9-12-2014

Accessing Gluon Polarization Through the J/\u03c8 Longitudinal Double Spin Asymmetry in Polarized pp Collisions at PHENIX

James Aaron Key

Follow this and additional works at: https://digitalrepository.unm.edu/phyc_etds

James Aaron Key
Candidate

Physics and Astronomy
Department

This dissertation is approved, and it is acceptable in quality and form
for publication:

Approved by the Dissertation Committee:

Professor Douglas Fields, Chairperson

Professor Igor Gorelov

Professor Michael Gold

Professor Adam Hecht

Accessing Gluon Polarization Through the J/ψ Longitudinal Double Spin Asymmetry in Polarized pp Collisions at PHENIX

by

James Aaron Key

Licenciado en Física, Universidad de Granada, 2010
M.S., Physics, University of New Mexico, 2013

DISSERTATION

Submitted in Partial Fulfillment of the

Requirements for the Degree of

Doctor of Philosophy

Physics

The University of New Mexico

Albuquerque, New Mexico

July, 2014

Accessing Gluon Polarization Through the J/ψ Longitudinal Double Spin Asymmetry in Polarized pp Collisions at PHENIX

by

James Aaron Key

Licenciado en Física, Universidad de Granada, 2010

M.S., Physics, University of New Mexico, 2013

Ph.D., Physics, University of New Mexico, 2014

Abstract

To date, the exact distribution of the fundamental property of intrinsic angular momentum, or spin, in the proton amongst its constituents is largely unknown. Through observation of the production of the J/ψ particle in polarized pp collisions at RHIC we are able to further constrain the contribution of the gluon polarization to the total spin polarization of the proton by expanding the global data available into a new kinematic regime.

Contents

Contents

Contents

Contents

Contents

List of Figures

List of Figures

List of Tables

Glossary

A_{LL} Double longitudinal spin asymmetry

R Relative luminosity ratio between helicity combinations

QCD   The theory of strong interactions: quantum chromodynamics

RHIC   **R**elativistic **H**eavy **I**on **C**ollider

PHENIX   **P**ioneering **H**igh **E**nergy **N**uclear **I**nteraction e**X**periment

IP   Interaction Point

IR   Interaction Region

BBC   Beam Beam Counter

ZDC   Zero Degree Calorimeter

FVTX   Forward Silicon Vertex Detector

MuID   Muon Identifier

MuTr   Muon Tracker

GPR   Gaussian Process Regression

Chapter 1

Introduction

The full understanding of the elemental structure of matter has been the impetus behind centuries of scientific research. From the pioneering efforts of Rutherford to the paradigm shifting triumphs of quantum electrodynamics and later quantum chromodynamics, the particle and nuclear physics communities as a whole have revolutionized time and again the way that we see the physical world at the most basic level. With each advance came a reassessment of our understanding of the fundamental properties of matter and the theories that we leverage to gain predictive power over the physical world. The proton has been studied extensively at numerous scales with a wide variety of probes and experimental techniques. Nonetheless, there remain fundamental properties of the proton that, to this day, cannot be sufficiently explained by any one theoretical model. The intrinsic angular momentum, or spin, of the proton and how it is formed from its constituent particles is one of those questions and the one with which this thesis is concerned.

The ultimate goal of spin physics is to complete our knowledge of the internal structure of the proton. Our knowledge of the proton has advanced from that of a simple point particle to the complex, composite particle as we understand it today.

Chapter 1. Introduction

QCD has proven wildly successful in describing a wide variety of observations in particle physics, yet numerous experiments have given, and continue to give, clear evidence of phenomena that are not fully described by a spin independent description of the strong interaction. Thus, our understanding of two of the most basic properties of matter is incomplete and must be extended to be inclusive of both. While the individual interpretations of the goal of physics as a whole may vary, clearly a robust and complete understanding of the composition of matter is of utmost importance. The ability to theoretically and experimentally disentangle the partonic contributions to the overall spin of the proton provides one of the most stringent challenges to the theoretical foundations of the strong interaction.

This thesis introduces the discoveries that have led us to our current understanding of the distributions describing the internal structure of the proton both in momentum and spin. In hopes of further constraining the experimental limits placed on the spin dependent gluon parton distribution function, an analysis of the double longitudinal spin asymmetry in J/ψ production is performed. In support of these efforts, and many others, a precision charged particle tracking and vertexing detector has been installed at the PHENIX experiment at the Relativistic Heavy Ion Collider (RHIC). The coverage of this precision detector extends into the forward region where it is possible to probe the gluon contribution to the proton spin in a momentum range where there exists no experimental data to date.

In chapter 2 we will introduce the theoretical foundations for the strong interaction and the Standard Model of particle physics and the experimental tools used to evaluate these theories. The implications of the details of QCD have on the internal structure of the proton and the framework for characterizing scattering in the case of composite particles as well as the relation to spin polarization are explored in chapter 3. The experimental apparatus used for providing polarized proton-proton collisions as well as the detector technologies utilized in the PHENIX experiment

are introduced in chapter 4. An important upgrade to the vertexing capabilities of the PHENIX experiment was installed in 2012, providing numerous improvements to existing measurements as well as enabling novel measurements involving the separation of heavy flavor meson decays. The details of the detector upgrade and upgrades designed and implemented as part of the work supporting this thesis are expounded in chapter 5. A detailed analysis of the production of the lowest energy $c\bar{c}$ bound state, the J/ψ , and the spin dependence of J/ψ production in polarized pp collisions is found in chapter 6. Finally, in chapter 7, a summary of the work completed and an outlook of future measurements that constrain the gluon contribution to the spin of the proton is explored. As stated above, the core goal of the field of spin physics is to resolve the details of the interplay of the theory of strongly interacting particles and the fundamental property of intrinsic angular momentum. QCD has proven wildly successful in describing a wide variety of observations in particle physics, yet numerous experiments have given, and continue to give, clear evidence of phenomena that are not fully described by a spin independent description of the strong interaction. Thus, our understanding of two of the most basic properties of matter is incomplete and must be extended to be inclusive of both. While the individual interpretations of the goal of physics as a whole may vary, clearly a robust and complete understanding of the composition of matter is of utmost importance.

Chapter 2

Quantum Chromodynamics

Quantum chromodynamics, the theory of strong nuclear interactions, is perhaps the most successful theory in physics in terms of the breadth, precision, and implications of the predictions that have been derived from decades of experimental and theoretical progress. In this chapter we will explore the history of QCD and arrive at how the theory of strong interactions and the spin of composite particles like the proton are related.

2.1 The Standard Model

The Standard Model of particle physics was developed during the second half of the 20th century and describes the electromagnetic, weak nuclear, and strong nuclear interactions of elementary particles. It was born out of an attempt to unify the electromagnetic and weak nuclear interactions by Glashow [1]. The Standard Model is a quantum field theory [2] with the underlying symmetries of relativistic invariance and the gauge symmetry of quantum chromodynamics and the electroweak interaction. In a gauge theory, the Lagrangian describing the kinematics is invariant under the

transformations of a Lie group [3], usually denoted the gauge group of the theory. That is, the Standard Model has a local gauge symmetry of $SU(3) \times SU(2) \times U(1)$. The group describing the symmetry of the electroweak interaction, the unified theory of the weak nuclear and the electromagnetic interactions is $SU(2) \times U(1)$ while the symmetry of the strong nuclear interaction, or quantum chromodynamics is described by $SU(3)$. Here, $SU(n)$ is the group of $n \times n$ matrices that are unitary, that is, that the matrix multiplied by the corresponding transposed matrix of complex conjugated elements is the identity matrix, or $UU^\dagger = U^\dagger U = I$ and special, $\det(U) = 1$. In group theory one may write down the so-called generators of the group, which is a subset of the group elements which can be repeatedly applied to generate all of the elements of the group. A quantum field theory predicts that there will be a number of force mediating particles, the gauge bosons, equal to the number of dimensions of the gauge group. These gauge bosons correspond precisely to the generators of the group, which implies that there are $n^2 - 1$ force carrying particles for a theory having a $SU(n)$ symmetry. The implications, therefore, are that the strong interaction is mediated by 8 vector bosons, the gluons, whose representation is that of the Gell-Mann matrices [4]. Accordingly, the weak nuclear interaction is mediated by the massive $W^\pm$ and Z bosons which are represented by the Pauli matrices and the electromagnetic interaction is mediated by a single vector boson, the photon. Additionally the Standard Model is a non-abelian gauge theory, which is simply that the generators of the group are non-commutative.

The remaining fundamental particles of the Standard Model are the three generations of quarks and leptons [5, 4], both of which are fermions. All other observed particles are composite particles that are formed from combinations of the fundamental particles, the most common of which are the mesons, bound states composed of a quark anti-quark pair, and the baryons, bound states of three quarks, which together form the family of particles known as hadrons which are predicted, once again, by group theoretical considerations guiding the possible combinations of fundamental

particles.A complete description of the phenomena predicted by the Standard Model and QCD falls outside of the scope of this document, but the reader is referred to [6] for an excellent treatment of the subject.

2.2 Partons

Quarks and gluons are referred to under the umbrella name of parton that is a generic descriptor for any particle that is a constituent of a hadron. The term parton was coined by Richard Feynman in 1969 when he proposed the parton model [5] as a framework for analyzing high energy collisions involving hadrons. The parton model did not achieve widespread acceptance but the partons that are the namesake of the theory were found to be the very same quarks and gluons that arise from QCD and hence the name has endured.

Quarks and gluons emerge from the $SU(3)$ sector of the Standard Model corresponding to QCD. In analogy to the electrical charge of quantum electrodynamics the name of the proportionality factor for QCD is known as "color charge". The relation to the quotidian usage of the word color is, however, quite tenuous in nature. Due to the underlying $SU(3)$ symmetry there exist 6 (anti-)color charges denoted (anti-)red, (anti-)blue, (anti-)green in contrast to the common QED charge. Using the generators of $SU(3)$, the Gell-Mann λ_i matrices, one can describe the 8 different possible gluon color charges as

$$g_i = \lambda_i \begin{pmatrix} r\bar{r} & r\bar{b} & r\bar{g} \\ b\bar{r} & b\bar{b} & b\bar{g} \\ g\bar{r} & g\bar{b} & g\bar{g} \end{pmatrix}$$

Just as with electrical charge a non-zero color charge is required to participate in a strong nuclear reaction. Additionally, all normal matter, such as nucleons, are known to be "colorless". The colorless state refers to any combination of colored

objects such that for every color present in the composite state the corresponding anti-color is also present in equal number (e.g., $N(r\bar{r}-g\bar{g})$ where N is a normalization constant) or a state where all three colors are present. Therefore, the particles with non-zero color charge are the quarks, antiquarks, and gluons. A $U(3)$ symmetry, that is the group whose elements are the 3×3 unitary matrices can be seen as the direct product of two subgroups: one with dimensionality 8 (an octet), $SU(3)$, and one with dimensionality 1 (a singlet). The gluons, of course, pertain to the $SU(3)$ subgroup and the colored collection of states is referred to as the "color-octet" [7]. The remaining state is the "color-singlet" which has no net color and, therefore, cannot be a representation of a gluon.

The net color of the vector bosons of the strong interaction is a result of the non-abelian nature of the gauge theory and leads to two important consequences with far-reaching effects: confinement [8] and asymptotic freedom [9, 10]. Confinement is the term given to the peculiar (in comparison with the other fundamental forces) behavior of the strong interaction that the force felt between particles with color charge grows stronger with increasing distance and, hence, smaller with decreasing distance. Thus, the strong interaction "confines" particles with color charge inside colorless composite particles [11]. Asymptotic freedom is simply the vanishing attraction in the limit of vanishing distance between colored objects. The practical implications of this inverted dependence with distance are that calculations must be done perturbatively at small distances (high energy) due to the necessity of calculating integrals that lack an analytical solution through a series expansion. At large distances (low energy) this series expansion in α_s, the strong coupling constant, diverges which renders perturbation theory incapable of producing predictive results.

2.3   The Strong Coupling Constant: α_s

To solidify the concept of the non-constant nature of the coupling constants in quantum gauge theories it can be shown that to second order the dependence of the fine structure constant (QED) for all $Q^2 \gg m^2$:

$$\alpha(Q^2) = \alpha(m^2) \left[1 + \frac{\alpha(m^2)}{12\pi} \log \frac{Q^2}{m^2} + \mathcal{O}(\alpha^2) \right] \tag{2.1}$$

and the dependence of the strong coupling constant is [12]

$$\alpha_s = \alpha_s(m^2) \left[1 + \frac{\alpha_s(m^2)}{12\pi} \log \frac{Q^2}{m^2} (2n_f - 11N) + \mathcal{O}(\alpha_s^2) \right] \tag{2.2}$$

where m^2 is the initial energy scale where the coupling constant is known, Q^2 is the mass of the gauge boson involved in the interaction (either the photon or the gluon in the cases of QED and QCD correspondingly), n_f is the number of "active" flavors (i.e., above the energy threshold for production), and N is the number of colors (3: red, blue, and green). Therefore these equations give the scaling of the coupling constants with interaction energy.

Given that $n_f \leq 6$ and $N = 3$ the factor of $2n_f - 11N$ that forms part of the constant for the term in α_s^2 will always be negative. It, therefore, follows that with decreasing distance we will have increasing Q^2 and hence $\alpha_s \to 0$ with $d \to 0$, which is the concept of asymptotic freedom.
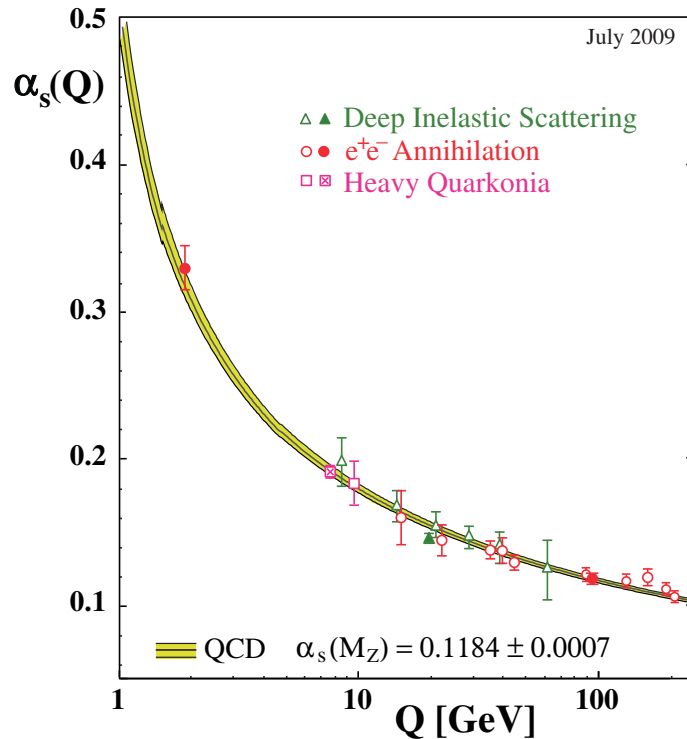
Figure 2.1: Scaling of the strong coupling constant as a function of energy scale [13].

2.4 Cross Sections and More

Before moving on to the details of how to apply QCD to the scattering of composite particles it is worthwhile to first introduce the tools and terminology used in describing interactions and particle production in medium and high energy collisions.

2.4.1 Terminology

One of the primary handles available in the comparison of theory and experiment is the cross section. The cross section gives us a manner of quantifying the production rates of a given particle in a scattering experiment. This is quite convenient as it is

often straightforward to identify produced particles from their observed properties (such as mass and charge) and directly count the number that have been produced. The cross section, σ, and in particular the differential cross section $d\sigma/d\Omega$, where Ω solid angle provide a manner of quantifying the particle production rates in a manner that is independent of the experimental apparatus.

As established in section 2.2, perturbation theory can only be applied to the short range strong interactions where the strong coupling constant is small. Fortunately, a technique known as collinear factorization allows one to express a cross section as a convolution of the part that can be calculated perturbatively, the hard scattering cross section of the partonic process, with two probability distributions that are not calculable, the parton distribution (f_a) and fragmentation functions D_c^h. The parton distribution function gives the probability to scatter off of a parton of flavor a and momentum fraction x, while the fragmentation function gives the probability for the outgoing parton, c, to produce a final state hadron, h, with a momentum fraction, z, of the outgoing parton as in Figure 2.2.
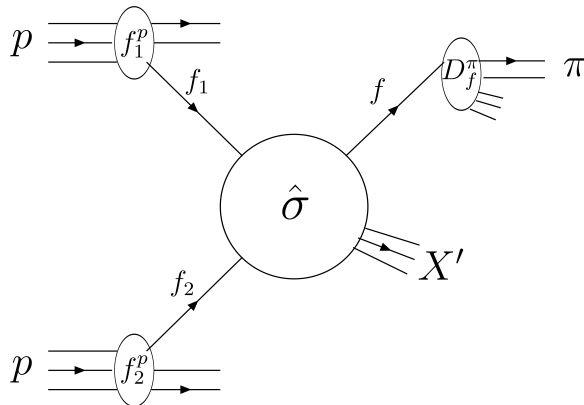
Figure 2.2: Collinear QCD factorization in pp collisions

The cross section under collinear factorization can, therefore, be written as

$$\sigma = \sum_{\{a,b\}} \int f_a(x_1) f_b(x_2) \otimes \hat{\sigma}_{ab \to cX} \otimes D_c^h(z) dx_1 dx_2 dz \tag{2.3}$$

The differential cross section need not be restricted simply to study as a function of solid angle and is frequently studied as a function of p_T, the momentum of the produced particle transverse to the beam direction, or y, the rapidity of the produced particle. The rapidity is defined as a function of the energy of the particle E and the projection of the momentum parallel to the beam axis.

$$y = \frac{1}{2} \frac{E + p_z}{E - p_z} \tag{2.4}$$

As is common in the world of collider experiments, and in particular for the case of PHENIX, the z axis is taken to be the beam axis. A more widely used quantity that is equivalent to rapidity in the limit of vanishing mass is the pseudorapidity which is more easily accessible experimentally as it is simply a function of the polar angle as measured from the z axis.

$$\eta = \frac{1}{2} \ln \left(\frac{|\vec{p}| + p_z}{|\vec{p}| - p_z} \right) \tag{2.5}$$

$$= -\ln \left(\tan \frac{\theta}{2} \right) \tag{2.6}$$

The rapidity and pseudorapidity in pp collisions are numerically very similar as the mass of the proton forms a very small fraction of the total energy of the particle when accelerated to 255 GeV.

To compare the particle production rate amongst experiments and separate data sets from the same experiment the number of produced particles must be measured relative to the total collisions rate during the same period. This is given by a quantity known as the luminosity (sometimes instantaneous luminosity) and has units of

cm^{-2}s^{-1}, therefore giving the particle yield per unit of target cross section, which in our particular case is the inelastic pp cross section. The integrated luminosity is used to refer to the time integrated luminosity and gives a measure of the number of supplied collisions. In the case of RHIC the typical unit of integrated luminosity is the inverse picobarn (pb^{-1}), which is equal to 10^{-36} cm^{-2} while in the higher luminosity LHC the basic unit is the femtobarn. The differential cross section can also be related to experimentally observable quantities through

$$\frac{d\sigma}{dp_T} = \frac{1}{\mathcal{L}\epsilon}\frac{dN}{dp_T} \tag{2.7}$$

where $\mathcal{L}$ is the integrated luminosity, dN is the count of produced particles in a range of transverse momentum dp_T, and ϵ is a correction factor that takes into account the geometrical acceptance of the detector and the efficiency with which the detector is capable of reconstructing a particle that passes through that geometrical acceptance. The efficiency is determined by a combination of the physical signal collection efficiency of the detector elements, the efficiency with which the software algorithms used are able to identify the signature of a particle passing through the detector, as well as the efficiency with which the particular event is able to be selected for output by triggering detectors (explained in detail in subsection 4.2.4).

In a circular collider with two counter-rotating beams the luminosity is written as a function of the physical characteristics of the beam and bunch structure of the beams. The accelerated proton beams are discrete in the sense that they are not a constant flux of protons, but rather a collection of spatially separate bunches of protons. The oscillation frequency of the acceleration cavities determines the frequency at which the bunches pass an interaction point along the beam line and therefore determines the maximum frequency at which interactions can occur (ignoring for now the possibility of more than one collision per bunch crossing). The luminosity can therefore be written as

$$\mathcal{L} = fn\frac{N_1 N_2}{A} \tag{2.8}$$

where f is the crossing frequency, n is the number of bunches that are filled with protons, N_i is the number of protons in the corresponding beam and A is the projection of the cross-sectional area of one beam upon the cross-sectional area of the other. f and n are fixed machine parameters of the collider while N_i is measured through instrumentation capable of measuring the beam current and A is measured through a process known as a Vernier, or Van der Meer [14] scan. This technique consists of gradually steering the beams out of collisions, one at a time, while studying the collision rate as a function of the transverse displacement of the steered beam to obtain the transverse profile of the beams.

Chapter 3

The Proton

The study of the nucleon has yielded great insight into the inner workings of our universe. Nonetheless, the theoretical description of scattering processes involving hadrons is still described in a phenomenological manner. This chapter will explore the current state of the theoretical and experimental results that have resulted in the modern understanding of the proton and its underlying structure in terms of position and momentum, of both the linear and intrinsic angular varieties.

3.1   Substructure

All of the known fundamental particles such as quarks, leptons, and the gauge bosons are hypothesized to be point-like in nature. That is: they have absolutely zero physical extension. At the beginning of the twentieth century there was debate as to the point-like nature of the proton. Precision measurements on the anomalous magnetic moment of the proton and neutron [15] found that the proton did not behave as would be expected for a point-like particle. This was further corroborated by the measurement of the $ep \rightarrow eX$ cross section where the angular distribution of

the outgoing lepton was found to deviate from the theoretical behavior for a point-like particle. The results of this experiment can be found in Figure 3.1.
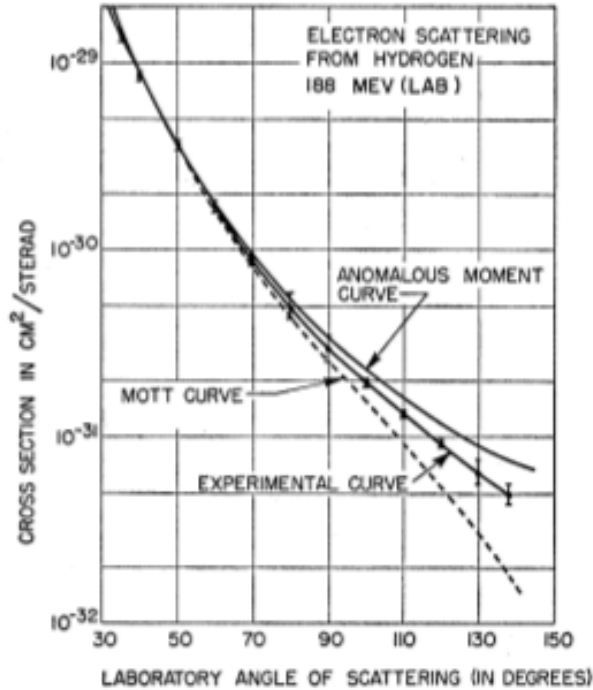
Figure 3.1: Experimental results for e^- scattering off of hydrogen targets at 188 MeV. The behavior observed deviates from both the behavior of a point like particle and that of a point like particle with the anomalous magnetic moment of the proton [15].

These experiments and discoveries launched the advances in our understanding of the strong nuclear interaction and the existence of fundamental particles that bind together to form the nucleon and eventually the development of QCD and the Standard Model. The above described experiment where a leptonic probe such as an electron is scattered on a quark or gluon is known as Deep Inelastic Scattering, or DIS. The incoming lepton exchanges a virtual photon with one of the constituents of the proton target which fragments while the lepton scatters and is present in the final state. Through these experiments it is now known that not only does the proton have

15

substructure such as being formed by two u quarks and one d quark as is determined by the well defined quantum numbers of the proton, but also contains a "sea" of quark-antiquark pairs in the form of the QCD vacuum, as well as the gluons that mediate the strong interactions between them. Therefore it makes sense to not only quantify the probability to scatter off of a valence quark in a nucleon, but as the energies probed are high enough for the collisions to become highly inelastic it also makes sense to quantify the probability to scatter off, for example, a strange quark or a gluon.
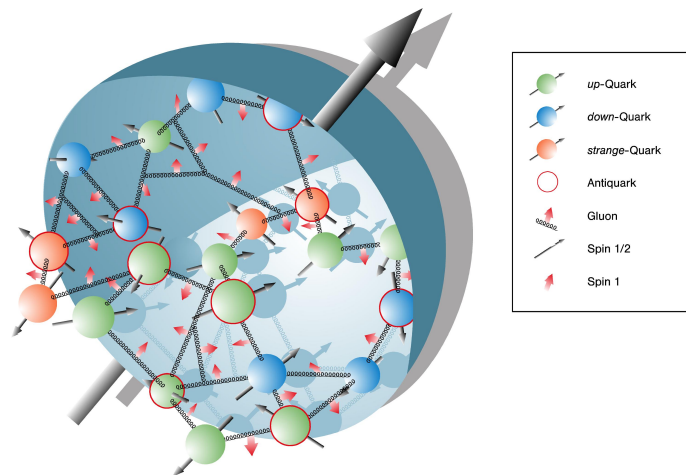
Figure 3.2: The proton as seen at probe energies high enough to resolve the internal QCD structure of quarks, antiquarks, and gluons.

As we will find, even though both the proton as well as the fundamental particles that form the proton bound state have well defined quantum numbers individually, the way in which those quantum numbers are composed to form those of the proton becomes non-trivial in the framework of QCD and the more complex picture that it provides of the true substructure of hadrons. This is particularly true of the spin quantum number of intrinsic angular momentum, or spin.

3.2   Hadronic Scattering

In quantum field theory the cross section of lepton-lepton scattering is described by a product of two leptonic tensors which are generally denoted $L_{\mu\nu}$ through

$$\frac{\mathrm{d}\sigma}{\mathrm{d}\Omega} \propto L^{\mu\nu}L'_{\mu\nu}. \tag{3.1}$$

In terms of the fermionic fields and the gamma matrices, the leptonic tensor [2] becomes

$$L_{\mu\nu} \propto \sum_{\lambda,\lambda'} \left(\bar{u}(k',\lambda')\gamma_\mu u(k,\lambda)\right) \left(\bar{u}(k',\lambda')\gamma_\nu(0)u(k,\lambda)\right)^*, \tag{3.2}$$

which is the commonly used tensor for calculating cross sections such as $q\bar{q} \to \mu^+\mu^-$ by calculating the tensor product of the leptonic tensors of each of the incoming quarks. In this equation there is a sum over helicities, $\vec{p}\cdot\vec{\sigma}$, for both the incoming (λ) and scattered leptons (λ'). In DIS we have the case of a lepton scattering off a parton within the proton. The tensor expression that is derived for leptons is analytically calculated from the QFT integrals. In the case of the hadron we also have a tensor, $W_{\mu\nu}$, that represents the fields involved through

$$W^{\mu\nu} \propto \sum_\sigma \int \frac{\mathrm{d}^4\xi}{2\pi} e^{iq\cdot\xi} \langle\vec{P},\sigma| \left[J_\mu^\dagger(\xi), J_\nu(0)\right] |\vec{P},\sigma\rangle \tag{3.3}$$

which describes the interaction of the electroweak currents with a target nucleon having spin 4-vector S such that $S^2 = -M^2$ and $S \cdot P = 0$.

However, given the composite nature of the proton the precise tensor representation is much more complex than the leptonic case. Instead, using symmetry arguments the hadronic tensor is parametrized as a function of various so-called structure functions [16]. J, therefore, is an operator that represents the effective vertex between the proton blob and the virtual photon exchanged with the lepton probe.
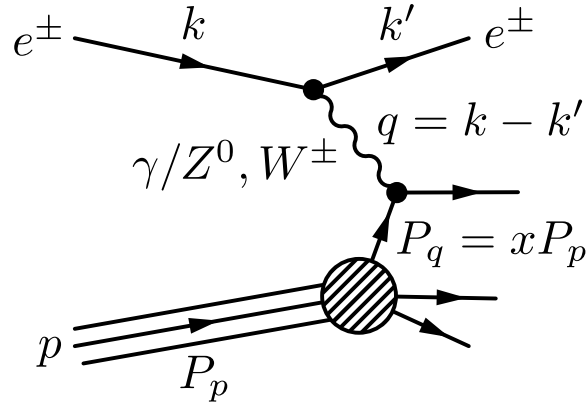
Figure 3.3: Feynman diagram corresponding to deep inelastic scattering (DIS) where an incoming lepton exchanges a virtual photon with a hadron and scatters.

The fully parametrized expression for the hadronic tensor is written as

$$
\begin{aligned}
W_{\mu\nu} =& \left(-g_{\mu\nu} + \frac{q_\mu q_\nu}{q^2}\right) F_1\left(x, Q^2\right) + \frac{\hat{P}_\mu \hat{P}_\nu}{P \cdot q} F_2\left(x, Q^2\right) \\
& - i\epsilon_{\mu\nu\alpha\beta} \frac{q^\alpha P^\beta}{2P \cdot q} F_3\left(x, Q^2\right) \\
& + i\epsilon_{\mu\nu\alpha\beta} \left[S^\beta g_1\left(x, Q^2\right) + \left(S^\beta - \frac{S \cdot q}{P \cdot q} P^\beta\right) g_2\left(x, Q^2\right)\right] \\
& + \frac{1}{P \cdot q} \left[\frac{1}{2}\left(\hat{P}_\mu \hat{S}_\nu + \hat{S}_\mu \hat{P}_\nu\right) - \frac{S \cdot q}{P \cdot q}\hat{P}_\mu \hat{P}_\nu\right] g_3\left(x, Q^2\right) \\
& + \frac{S \cdot q}{P \cdot q} \left[\frac{\hat{P}_\mu \hat{P}_\nu}{P \cdot q} g_4\left(x, Q^2\right) + \left(-g_{\mu\nu} + \frac{q_\mu q_\nu}{q^2}\right) g_5\left(x, Q^2\right)\right]
\end{aligned}
\tag{3.4}
$$

where

$$
\hat{P}_\mu = P_\mu - \frac{P \cdot q}{q^2}q_\mu, \qquad\qquad \hat{S}_\mu = S_\mu - \frac{S \cdot q}{q^2}q_\mu
\tag{3.5}
$$

and F_i are the unpolarized (spin independent) structure functions as the unpolarized cross sections in DIS can be written in terms of F_i [17]. The difference in the polarized cross sections that depend on the lepton and nucleon helicites, in turn, can be written in terms of the g_i and are therefore known as the spin dependent structure functions. In the above expressions x (sometimes seen as x_B) is defined as $x_B = \frac{Q^2}{2Mq^0}$. In the

limit of infinite proton momentum x_b corresponds physically to the fraction of the total hadron momentum that is carried by the interacting parton. In collisions at RHIC at a center of mass energy of 510 GeV in comparison with a nucleon mass of approximates 1 GeV the approximation is appropriate.

Additionally, in pp collisions it is common to use the approximation

$$x_1 = \frac{M}{\sqrt{s}}e^y, \qquad x_2 = \frac{M}{\sqrt{s}}e^{-y} \tag{3.6}$$

which again, in the limit of infinite proton momentum can be interpreted as the fraction of the total proton momentum carried by the struck parton. In the same approximation M can be replaced by the transverse momentum p_T and the rapidity with the pseudorapidity η, which are more readily available as experimental observables.

In QCD, the structure functions are a function of scale-dependent parton distribution functions $f_a(x, \mu^2)$ where a is the type of parton (i.e., gluon or quark), μ is the renormalization scale which is typically taken to be the scale of the probe. When $Q^2 \gg M^2$ the structure functions can be written as

$$F_i = \sum_a C_i^a \otimes f_a \tag{3.7}$$

where the coefficients are written as a power series in the strong coupling constant α_s. The parton distribution functions are a quantity that give the probability to scatter off a parton of a given flavor with momentum fraction x integrated over all values of partonic transverse momentum k_t. The parton distribution functions (PDFs) cannot be calculated perturbatively, but are universal. That is, as they are determined in one experiment they are applicable to other experiments even if they involve a different collision environment with respect to species and center of mass energy. The state of the art PDFs as determined in the CT10 analysis are shown in Figure 3.4 and described in detail in [18]. The PDFs are determined from a wide variety of fixed target DIS experiments at SLAC, FNAL, and CERN as well as ep collider data from

HERA. To access the flavor decomposition of the quark anti-quark sea and gluon distribution they also include measurements of jet production in hadronic collision, dilepton production through Drell-Yan processes, and W and Z boson production at Tevatron and LHC.
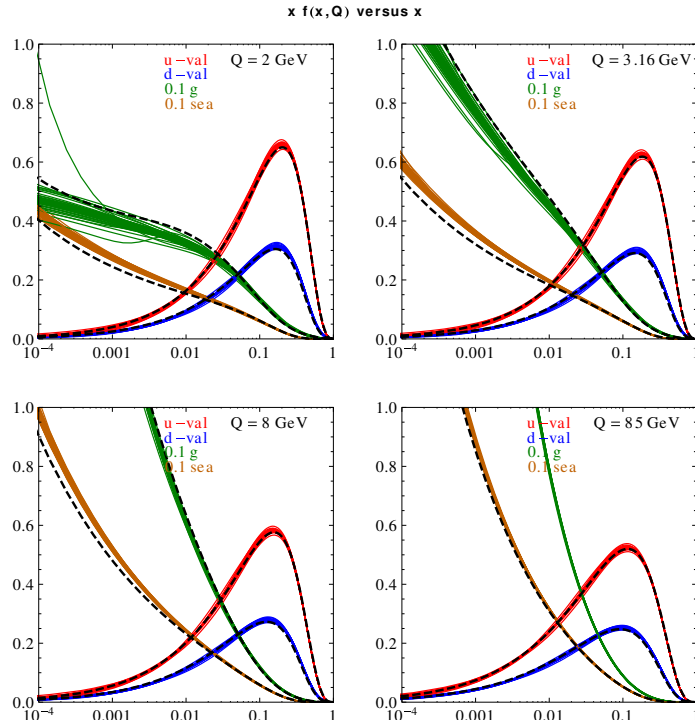
Figure 3.4: CT10NNLO parton distribution functions as a function of x for a fixed value of Q. The values of Q are 2, 3.16, 8, 85 GeV. The dashed curves are the central CT10 NLO fit [18].

3.3   Spin Structure

While there is a flourishing field involved in the study of the transverse momentum and position structure of the proton as well as the transverse spin dependent behavior we will not discuss the details of the work towards obtaining a full three dimensional picture of the internal structure of the proton beyond a cursory introduction. From

there we will move on to the case of longitudinal spin dependent effects which are the focus of the analysis effort of this thesis.

3.3.1 Generalized Parton Distributions

The previously described parton distribution functions are the diagonal elements of the type $\langle P, \lambda | \hat{O} | P, \lambda \rangle$, with P and λ the 4-momentum and helicity of the proton. The generalized parton distributions (GPDs) are defined in terms of the off-diagonal matrix elements, i.e., $\langle P', \lambda' | \hat{O} | P, \lambda \rangle$.
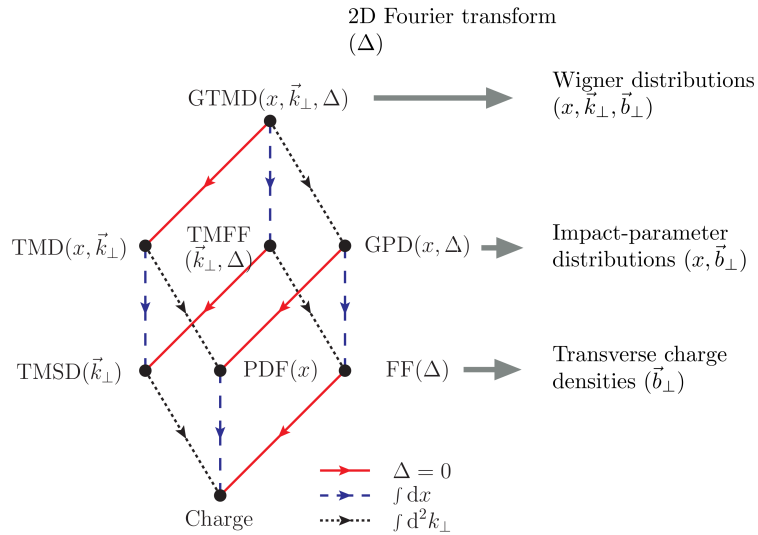
Figure 3.5: Graphical representation of the various generalized forms of parton distributions within the nucleon. The dotted connecting lines imply translations from one distribution function type two another and the variable over which each is integrated.

The various forms of GPDs contain information on additional properties such as the transverse spatial distribution of the partons in the impact parameter (Δ) plane within the nucleon and the distribution of the transverse momentum $(k_\perp)$ within the

nucleon. As with traditional parton distribution functions they are not calculable from first principles and must be determined from experiment, which is at the time of the writing of this thesis a highly active area of research. A full review of the state of the art of the field of GPDs can be found in [19, 20, 21].

3.3.2 Gluon Polarization

Alternatively, the parton distribution functions can be studied for their potential spin dependence where $\Delta f_q(x, Q^2)$, the *polarized* PDF, is the difference between PDFs with the interacting parton spin aligned and anti-aligned with the proton.

$$\Delta f_q(x, Q^2) = f_{q+}(x, Q^2) - f_{q-}(x, Q^2) \tag{3.8}$$

Therefore, the total polarization of a given parton, as a function of Q^2 is the integral of the polarized PDF over all values of x. For the case of the gluon we have:

$$\Delta G(Q^2) = \int_0^1 dx \Delta g(x, Q^2) = \int_0^1 dx \left[g_+(x, Q^2, \mu^2) - g_-(x, Q^2, \mu^2) \right] \tag{3.9}$$

The polarized PDFs cannot be measured directly, but rather studied through the use of a spin asymmetry which is an experimental observable. In the case of the gluon polarization what is studied is the double longitudinal spin asymmetry or A_{LL} which is defined as the relative difference in the cross section for a given process when the colliding, longitudinally polarized protons have like and unlike helicities as given by

$$A_{LL} = \frac{\sigma_{++} + \sigma_{--} - \sigma_{+-} - \sigma_{-+}}{\sigma_{++} + \sigma_{--} + \sigma_{+-} + \sigma_{-+}} \tag{3.10}$$

or in terms of particle yield

$$A_{LL} = \frac{1}{P_B P_Y} \frac{N_{++} - R N_{+-}}{N_{++} + N_{+-}} \tag{3.11}$$

where P_X is the polarization of beam X and R is the relative luminosity

$$R = \frac{L_{++}}{L_{+-}} \tag{3.12}$$

between like $(++)$ and unlike $(+-)$ helicity crossings. We will revisit the polarized PDFs and the manner in which they are calculated from the sum of global data available from polarized experiments in chapter 6.

It is of interest to study the distribution of the spin amongst the different types of partons within the nucleon not only to obtain a complete picture of how spin is distributed amongst the constituents of a composite particle, but also given 1988 result of the European Muon Collaboration (EMC) that discovered the spin composition of the three valence quarks within the nucleon is not sufficient to account for the whole of the spin polarization of the proton [22]. The results of the EMC experiment where polarized muons were scattered off of a proton target can be observed in Figure 3.6 where it is found that the $g_1(x)$ structure function of the proton is much smaller than necessary for the valence quark spin to account for the proton spin. Therefore, the remaining spin polarization must derive from one of the other possible sources within the nucleon as described by

$$\langle S_z \rangle = \frac{1}{2} = \frac{1}{2}\Delta\Sigma + \Delta G + L_q + L_g \tag{3.13}$$

where $\Delta\Sigma$ is the valence/sea quark polarization, ΔG is the gluon polarization, L_q is the quark/antiquark orbital angular momentum, and finally L_g is the gluon orbital angular momentum. The theoretical foundation of the angular momentum contributions and the possible link to experimental observables is currently an active area of research. While also not without theoretical debate, the gluon polarization is potentially the most experimentally accessible component with the apparatuses available to us today and is, therefore, the topic of this thesis.
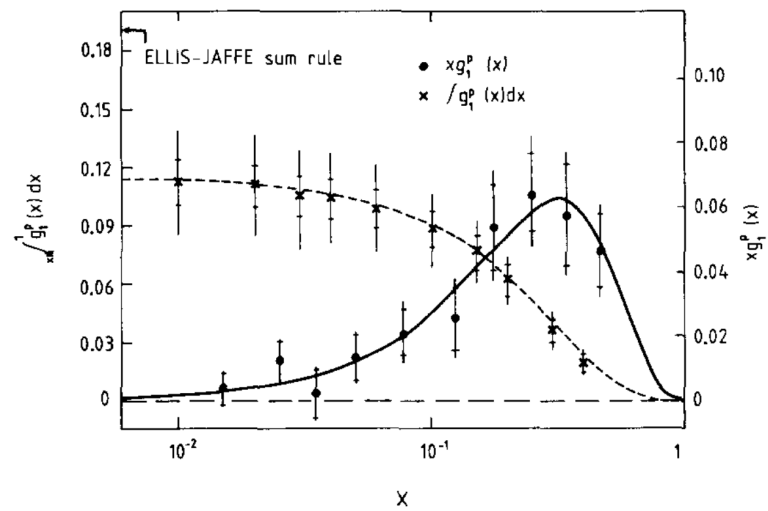
Figure 3.6: Results of the 1988 EMC experiment [22] that gave the first indication that spin composition in composite particles is affected by the small scale quark sea and gluon structure of QCD.

Chapter 4

The PHENIX Experiment

In the study of nucleon structure and nuclear processes at high temperatures, the days of an inexpensive, tabletop experiment have long since passed. In order to make the precise observations necessary to lend insight to the open questions on the fundamental properties of ordinary matter, it is necessary to turn to an extraordinarily complex and sophisticated experimental apparatus. In this chapter we will explore the accelerator infrastructure and detector systems that make these measurements possible.

4.1 RHIC

The Relativistic Heavy Ion Collider (RHIC) is a counter-rotating double ring hadron collider located at Brookhaven National Laboratory. The collider is able to accommodate a wide variety of species at a center of mass energy of up to 255 GeV per proton or up to 100 GeV per nucleon in heavy ion collisions. RHIC is the world's first, and only, collider capable of providing polarized proton-proton collisions. As such, it is one of the only facilities in the world capable of performing measurements

that can further the current knowledge of the spin structure of the proton.

Prior to the completion of RHIC, the only experimental probes of the nucleon spin structure were from polarized DIS measurements in fixed target experiments. These experiments, while highly successful in constraining the valence quark polarized parton distribution functions, are inherently limited in their ability to probe the gluon polarization due to the use of an electromagnetic probe. To properly probe the polarized gluon polarization it is necessary to employ a strongly interacting probe. Given the practical impossibility of producing of a gluon beam, polarized or otherwise, one must move to polarized hadron-hadron collisions. The idea for the construction of RHIC was first conceived in 1983 and nearly two decades later the first commissioning run of the collider and the associated detectors was completed in 2000. The construction leveraged an already extensive accelerator complex at BNL that, suitably for this thesis, served as one of the original locations for the simultaneous, Nobel prize winning discovery of the "J" portion of the J/ψ particle in 1976 [23].

In the polarized proton operating mode, an optically pumped polarized ion source (OPPIS) supplies polarized H$^-$ ions for acceleration and is capable of providing 80% polarization at sufficient current to guarantee a bunch intensity of at least 2×10^{11} protons per bunch at RHIC. From the polarized source the protons are accelerated to 200 MeV by a 200 MHz LINAC and transferred to the BOOSTER where they are brought up to the injection energy of 1.5 GeV for the Alternating Gradient Synchrotron (AGS). The AGS serves to further accelerate the bunched protons to 25 GeV at which point they can be successfully injected into either of the RHIC storage rings (arbitrarily denoted Blue and Yellow) through the AGS-to-RHIC transfer line which makes vertical and horizontal shifts to arrive in the RHIC plane. Prior to injection, the polarization of the protons is measured. More detail on the polarization measurement is presented in subsection 4.1.1.
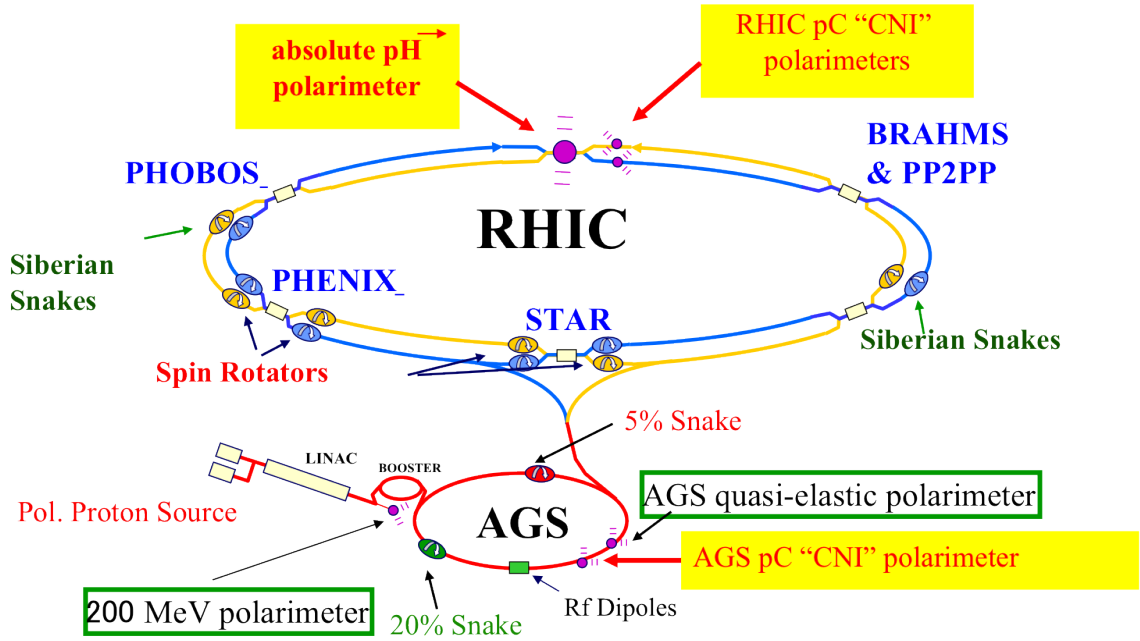
Figure 4.1: RHIC accelerator complex with detail for polarized pp collisions

Polarized collisions in a variety of orientations are provided at the various experimental halls along the RHIC ring. The primary experiments are PHENIX and STAR which have collected data for all RHIC runs. The main experiments are complemented by smaller, more specialized experiments which are run selectively for shorter periods. The stable direction for spin polarization is transverse to the momentum of the polarized particle and the plane of circulation. To be able to provide longitudinally polarized collisions, both STAR and PHENIX have upstream and downstream spin rotating magnets that bring transversely polarized protons into longitudinal collision and then rotate the remaining protons in the bunch back into transverse polarization [24].

Maintaining beam polarization during acceleration is a complex feat that requires a careful analysis of the dynamics of spin evolution. The precession of the spin vector in the presence of external magnetic fields in a circular accelerator is given by the

Thomas-BMT equation [25]:

$$\frac{\mathrm{d}\vec{P}}{\mathrm{d}t} = -\left(\frac{e}{\gamma m}\right)\left[G\gamma\vec{B}_\perp + (1+G)\vec{B}_\parallel\right] \times \vec{P} \tag{4.1}$$

where γ is the Lorentz factor of the accelerated particle and G is the anomalous magnetic moment. One can relate this to the orbital equation of motion in an external magnetic field as given by the Lorentz force equation,

$$\frac{\mathrm{d}\vec{v}}{\mathrm{d}t} = -\left(\frac{e}{\gamma m}\right)\vec{B}_\perp \times \vec{v} \tag{4.2}$$

and readily observe that the spin vector of a proton in circular orbital motion as experienced in a ring collider precesses at a rate that is $G\gamma$ times that of the orbital motion. For a proton with energy of 250 GeV, $G\gamma$ is approximately 478 [26]. In an ideal planar accelerator $G\gamma$ is known as the spin tune, or ν_{sp}.

The difficulty in maintaining beam polarization during acceleration is due to what are known as depolarizing resonances. Such a resonance occurs when the spin precession frequency, as given by (4.1), is equal to the frequency with which perturbing forces are encountered. When near a resonance the stable spin direction is no longer vertical and the ratio of final polarization to initial polarization when crossing a resonance is given by

$$P_f/P_i = 2e^{-\frac{\pi|\epsilon|^2}{2\alpha}} - 1 \tag{4.3}$$

where α is the spin tune change per radian of orbit angle, or in other words, the rate at which the proton is accelerated through the resonance. When this acceleration is sufficiently slow the evolution of the stable spin direction is adiabatic and will result in a rotation of the spin vector by 180° and the spin is effectively flipped by passing through the resonance while maintaining the same polarization magnitude. However, partial depolarization will occur for realistic acceleration rates. While this can be partially overcome with careful manipulations of the collider parameters, the large number of depolarizing resonances at high energies make this impractical.

In order to avoid the depolarizing resonances specialized sets of helical dipole magnets known as "Siberian snakes" [27, 28, 24], or spin flippers, invert the orientation of the spin vector within the transverse plane. In particular, at RHIC, there are two sets of Siberian snakes per beam so that the spin direction is inverted every half turn of the beam. The AGS also utilizes a similar magnet to avoid depolarizing resonances, but due to physical space constraints it is only a "partial snake" that rotates the spin vector by less than 180°. The partial snake is sufficient at the lower energies of the AGS to maintain the beam polarization as the stable spin direction will remain in the vertical direction as long as the rotation due to the Siberian Snake is much larger than the rotation due to the depolarizing resonance. These specialized magnets have made it possible to maintain an average polarization of both beams in excess of 50% during an eight hour store with future improvements targeting polarization values of greater than 60%.

4.1.1 Polarimetry

Due to losses in the injection and ramp to storage energy, the resulting bunch polarization will be significantly less than at extraction from the polarized source. For any spin dependent measurement it is crucial to precisely quantify the beam polarization as it will result in a global scale factor for any spin asymmetry measurement as in Equation 3.11. Fills at RHIC are typically held for 8 hours. When a fill is started it is useful to quickly affirm that the polarization is minimally acceptable before continuing to the length of a full store. Given the competing needs for both responsive and precise measurements of the polarization, two polarimetry methods are in use at RHIC: H-jet (hydrogen jet) and pC (proton-carbon).

Both methods depend on the measurement of a transverse single-spin asymmetry (SSA). That is, the asymmetry in the azimuthal distribution of the outgoing particles with respect to the spin orientation of the incoming particle. The polarization of the

beam can then be calculated given that

$$\mathcal{P}_{beam} = -\frac{\epsilon_N}{A_N} \qquad (4.4)$$

where A_N is the true, physics asymmetry in transversely polarized proton scattering and ϵ_N is the raw asymmetry given by the relative difference in the number of outgoing particles scattered to the left and right of the polarization axis of the incoming proton, or

$$\epsilon_N = \frac{N_L - N_R}{N_L + N_R}. \qquad (4.5)$$

pC or CNI (Coulomb-Nuclear Interference) polarimetry [26] is conducted by passing an extremely thin carbon strip through the beam and measuring the angular distribution of the recoil protons. This is accomplished by the use of silicon strip detectors surrounding the target as seen in Figure 4.2. This method has abundant statistics and is capable of producing a reasonable measurement within seconds. Specifically for the case of the pC collisions we have that

$$\mathcal{P}_{beam} = -\frac{\epsilon_N^{pC}}{A_N^{pC}}, \qquad (4.6)$$

where ϵ_N is the raw asymmetry in the detected recoil carbon nuclei. Notably, without knowledge of the physics asymmetry, the pC polarimeter would not be able to provide an absolute measurement of the polarization. However, thanks to a second, independent polarimeter this is not the case.

Hydrogen jet polarimetry [29] consists of a very low pressure hydrogen gas that is maintained within the beam line for the duration of the store. Due to the low pressure necessary to maintain a pure sample of H^+ gas, the interaction rate is accordingly quite low and an entire fill is necessary to accumulate sufficient statistics to precisely determine the beam polarization. Given that both the proton from the beam and the proton from the H-jet polarimeter are polarized one can write

$$\mathcal{P}_{beam} = -\frac{\epsilon_N^{beam}}{A_N^{beam}} \quad ; \quad \mathcal{P}_{target} = \frac{\epsilon_N^{target}}{A_N^{target}}. \qquad (4.7)$$
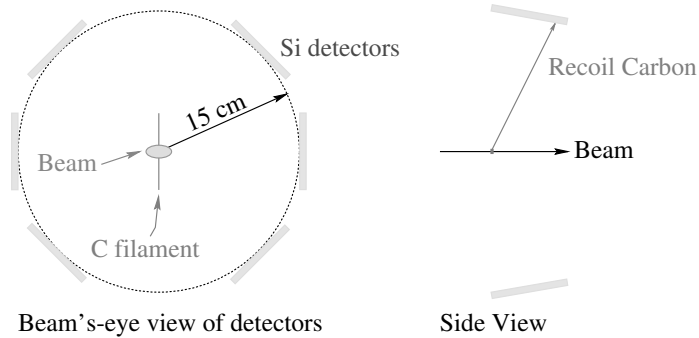
Figure 4.2: Cross-sectional view of the pC polarimeter. The silicon strip detector are distributed azimuthally around the target [26].

However, since it is the case that both the beam and the target are protons the physics asymmetry will be the same for both: $A_N^{pp} = A_N^{beam} = A_N^{target}$. Therefore, the H-jet polarimeter is capable of providing an absolute measurement of the polarization that does not depend on knowledge of the physics asymmetry as in

$$P_{beam} = P_{target} \frac{\epsilon_N^{beam}}{\epsilon_N^{target}} \tag{4.8}$$

where ϵ_N^{target} is the raw asymmetry measured by considering the hydrogen target as polarized and averaging over the two spin orientations for the beam.

It is possible to measure the physics asymmetry in pC, A_N^{pC}, by first determining the beam polarization with the H-jet polarimeter and using that, $\mathcal{P}_{beam}$, with Equation 4.6. Once A_N^{pC} has been determined and confirmed to not be a function of time, the pC polarimeter can also be used to supply an absolute measurement of the polarization.
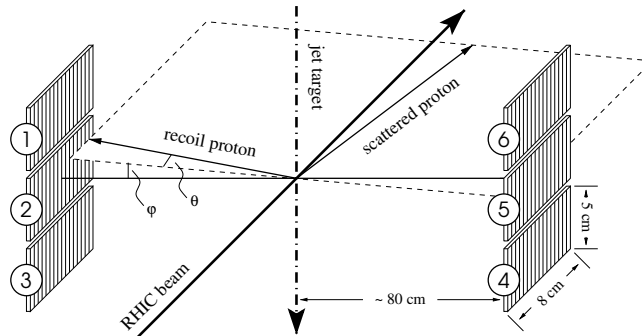
Figure 4.3: Schematic representation of the hydrogen jet polarimeter. Silicon strip detectors are located to the left and right of the beam line to detect the recoil proton from the hydrogen gas [29]

4.2 PHENIX

The **P**ioneering **H**igh **E**nergy **N**uclear **I**nteraction e**X**periment (PHENIX) [30] is a collection of specialized detector subsystems designed specifically for the efficient detection and study of nucleon-nucleon interactions through leptonic decay processes. Contrary to the design of many modern experiments, the PHENIX experiment sacrifices hermetic 4π coverage for precision and data acquisition speed in an attempt to study rare processes. The detector subsystems are separated into three main groups: global detectors used for event characterization and triggering, central arm detectors focused on the study of photons and electrons, and the muon arms which mainly study muons in the forward rapidities.

4.2.1 Central Arm Detectors

As their name belies, the central arm detectors are located at central rapidity covering $-1.2 < \eta < 1.2$. Tracking coverage is available from the Drift Chamber and Pad Chamber and covers approximately $\pi/2$ azimuthally in each of the two arms [31].

A recently installed barrel precision silicon pixel vertex tracker (VTX) [32] matches, and exceeds, the coverage of the original tracking detectors and provides a high resolution primary vertex measurement. Complementing the tracking detectors are two electromagnetic calorimeters consisting of lead glass (PbGl) and lead scintillator (PbSc) technologies for better control of systematic uncertainties. Particle identification is accomplished by way of a rich imaging Čerenkov detector [33] as well as precision time of flight detectors (ToF) with resolutions of approximately 100 ps [34].
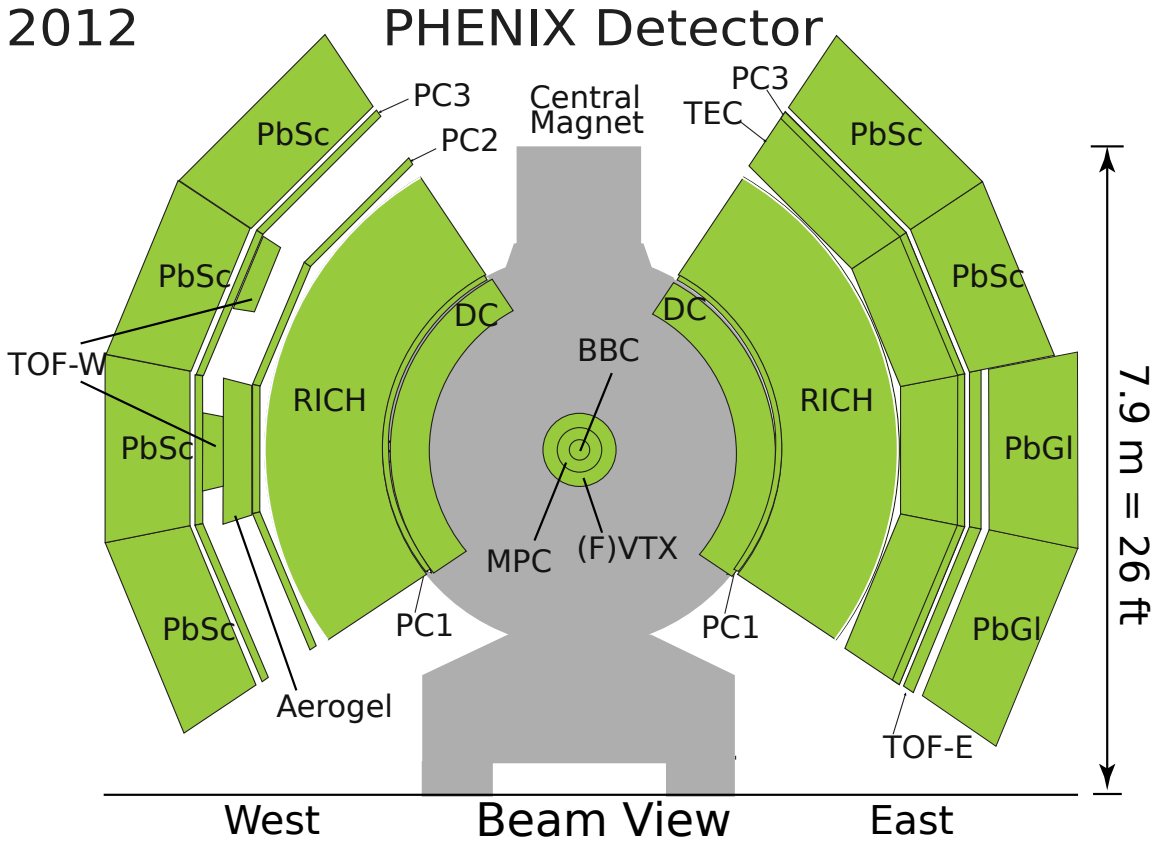
Figure 4.4: Diagram of the central arm PHENIX detector subsystems as installed in the experimental hall for the 2013 running period.

The primary focus of the central arm detectors is to provide high resolution tracking in conjunction with finely segmented electromagnetic calorimetry that is

suitable for the high occupancy found in heavy ion collisions. The primary channels studied by the central arm are two photon decays of π^0, direct photons, and e^+e^- pairs from J/ψ decays. With the addition of the VTX, the precise determination of the primary collision vertex enables the discrimination of prompt or short lived intermediate particles and longer lived intermediates such as B or D mesons. A schematic of the cross section of the central arm detectors can be found in Figure 4.4.

4.2.2 Muon Arm Detectors

Accordingly named, the muon arms [35] are a set of high resolution forward spectrometers operating in a radial magnetic field as well as a series of absorbers that serve to reduce the hadronic background and identify muons by their highly penetrating nature.

As seen in Figure 4.5, the muon arms have full 2π coverage in ϕ and cover a pseudorapidity range of $1.2 < |y| < 2.4$ with one arm on either side of the interaction point, denoted North ($+z$) and South ($-z$) in the PHENIX coordinate system. The arms are largely symmetric, but due to the physical constraint that the South arm remain mobile to allow for maintenance, the South arm is smaller. The spectrometer, known as the Muon Tracker (MuTr), is composed of three stations with three chambers in the first two stations and two in the final station. Inside the chambers are cathode wire strips that are held at approximately 1.85 kV below the anode wires. When the chambers are filled with a mixture of Ar, CO_2, and CF_4 charged particles passing through the gas will deposit charge onto the anode wires, creating an image charge on the cathode strips, which is digitized and translated into known positions, or coordinates, within the detector. The spatial information recorded at the various stations is processed through a pattern recognition algorithm into tracks. The azimuthal bending of the tracks is then used with knowledge of the magnetic field strength to extract momentum information.
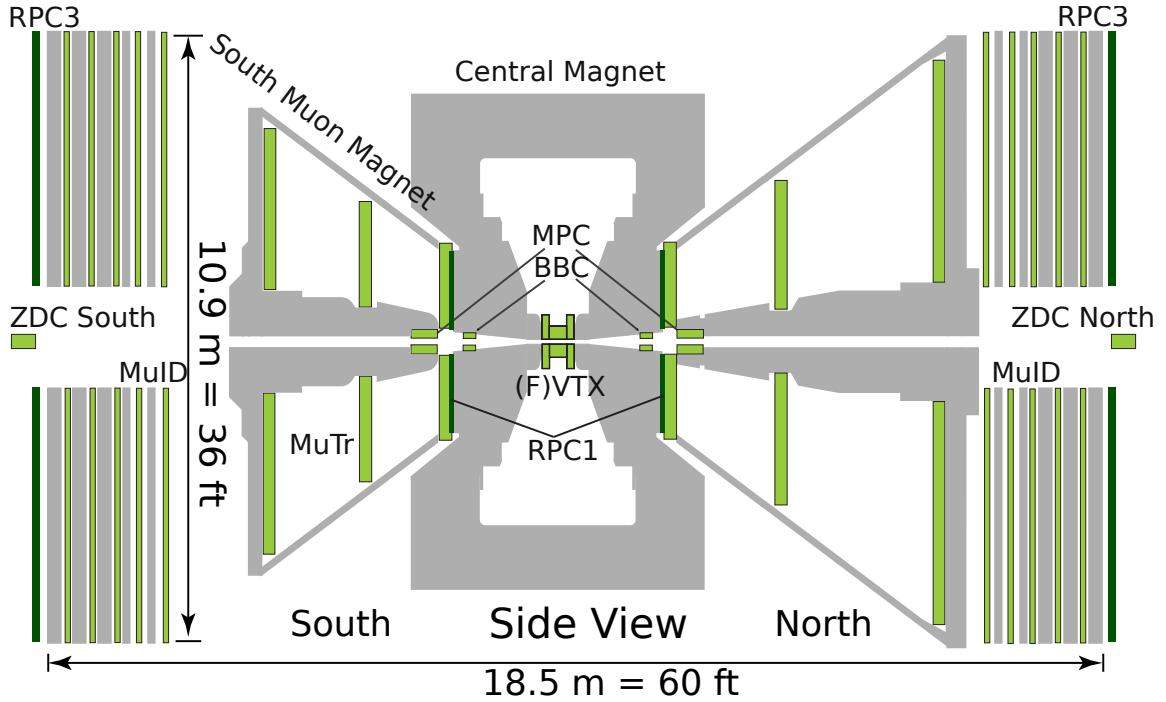
Figure 4.5: Side profile diagram of the forward PHENIX detector subsystems as installed in the experimental hall for the 2013 running period.

Behind the spectrometer lies the Muon Identifier (MuID). Constructed of interleaved plates of steel absorber and Iarocci tubes (proportional tubes), they measure both penetration depth and serve as a seed for tracking through the MuTr. The tubes themselves are 8.4 cm in width and oriented alternatively vertically and horizontally to provide two dimensional position information. There are a total of five planes of absorber material and four planes of active detector. To reach the final gap of the MuID, a muon must have an energy of at least 2.7 GeV, while the probability for a pion with 4 GeV to reach the same depth is 3% or less. This serves to greatly increase the purity of muons within the sample of all tracks in the MuTr.

Upgrades to the muon arms include two resistive plate chamber (RPC) stations located at the front and back of either arm of the spectrometers that provide precise

timing and additional rough tracking information for the rejection of beam related backgrounds, as particles that are comoving with the beams can be rejected. The RPC output is combined with that of the MuTr and MuID to create an efficient trigger (details in subsection 4.2.4) for the selection of events with a large fraction of true muons.

4.2.3 Event Characterization

In addition to the main spectrometers and calorimetric detectors in PHENIX, there are also two separate subsystems for event characterization and triggering: the Beam Beam Counter (BBC) [36] and the Zero-Degree Calorimeter (ZDC) [37]. Both detectors fill the essential role of determining whether or not, within a given crossing, a collision has occurred. Additionally, prior to the installation of the silicon vertex detector upgrades the most precise vertex information available came from the BBC as it measures both the time and position of each collision along the beam axis.
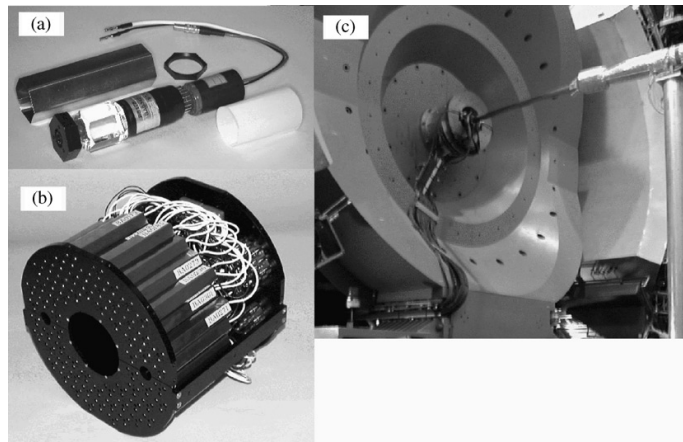
Figure 4.6: (a) A single photomultiplier tube mounted on a quartz radiation. (b) An arm of the BBC detector composed of 64 PMT units. (c) The BBC detector as installed in the PHENIX detector behind the central magnet [36].

The BBC is composed of two arms that are located at ± 144 cm along the beam axis and centered around the nominal interaction point. The coverage of the detector is very forward with pseudorapidity of approximately $3.0 < |\eta| < 3.9$. In each arm there are 64 photomultiplier tubes located radially around the beam pipe with a 3 cm quartz radiator mounted on each. The design of the BBC allows for an RMS timing resolution of 54 ps. The time of interaction (t_0) and the vertex position of the collision can be calculated from the time of arrival at the north (t_N) and south (t_S) arms according to the following relation.

$$z_{BBC} = c(t_N - t_S)/2, \tag{4.9}$$

$$t_0 = (t_N + t_S)/2 \tag{4.10}$$

Given that the maximum crossing frequency at RHIC is 9.6 MHz, the resolution is more than sufficient to determine the presence of a collision and capable of providing a longitudinal vertex resolution of 2-5 cm depending on the collision species (i.e., heavy ion or pp).

The ZDC also consists of two arms, but located much farther from the interaction point at approximately ± 18 m with a horizontal acceptance of ± 5 cm providing extremely forward rapidity coverage. Each layer of the calorimeter is comprised of an absorber composed of copper-tungsten and a PMT which collects light guided along optical fibers that are sandwiched behind the absorber. The ZDC primarily measures neutrons and therefore has an additional charged particle identifier and veto in the form of an additional layer of scintillator placed between the front of the ZDC and the interaction point. A secondary detector is located between the first two layers of the ZDC and is composed of horizontal and vertical scintillator strips of 15 mm or 20 mm widths. To maximize resolution, these Shower Maximum Detector (SMD) strips are inclined at 45° and are capable of providing position resolutions of approximately 1 cm in the transverse plane. The timing resolution of the ZDC detector is approximately 100 ps and provides a second vertex measurement, but the
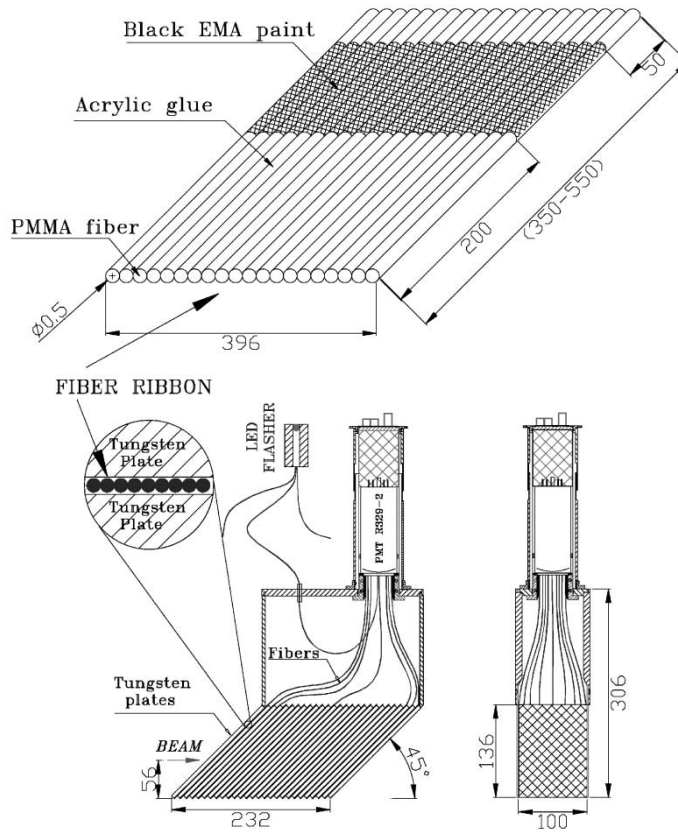
Figure 4.7: Mechanical design of a single layer of the ZDC [37].

reduced timing resolution in conjunction with the larger distance from the interaction point causes the ZDC to have a much poorer vertex resolution. As such, the ZDC is typically not used for vertex determination purposes, but is still viable as a triggering detector, luminosity monitoring, and for a local measurement of the polarization.

4.2.4 Triggering

As previously mentioned, the maximum collision rate of RHIC is 9.6 MHz. The maximum collision rate has been approached, and exceeded when taking into account multiple collisions per crossing, in the most recent pp running period. However, due

to bandwidth and storage constraints, it is impossible to commit data from the full 9.6 MHz of collisions to disk for later analysis. Even if the technology existed to commit the full amount of data to disk, the sheer amount of information would confound analysis efforts by the time required to analyze a large volume of mostly "uninteresting" events. The purpose of triggering subsystems is to reduce the flood of data down to rates that can be practically stored to disk without blindly rejecting events that have a high probability of being "interesting" by virtue of coming from a rare process with a certain event topology. The PHENIX data acquisition system is capable of sustaining approximately 6 kHz rates of committing event data to disk. Even when dropping the data from 99.9% of all collisions this translates to storing roughly 1.2 GB of data to disk every second and leads to multiple petabyte data sets. The sheer volume requires great effort and care for proper storage and manipulation of the data in a manner conducive to subsequent analysis into reliable physics results.

Triggering makes use of fast signals provided by any of the PHENIX subsystems capable of producing an event by event decision quickly enough for PHENIX as a whole to retrieve the data from a temporary buffer that is nominally 64 beam clocks in depth. In PHENIX, the triggering architecture consists of subsystem level trigger systems referred to as local level 1 (LL1) which serve as inputs into a higher level global level 1 (GL1) trigger system that processes and emits trigger decisions to all of the PHENIX detectors based on programmable combinations of the LL1 inputs. As mentioned previously, the minimum requirement to commit the data from a given beam crossing to disk is that a collision occurred, and both the BBC and ZDC are capable of such a detection. Such a trigger is referred to as a minimum bias trigger as it should apply minimal bias towards a specific type of event. The BBC minimum bias trigger consists of requiring that a hit was recorded in at least one PMT in both arms on either side of the interaction point. Additionally, the timing information is available to the LL1 system and further selection can be done on the rough vertex position of the collision. This can become important at PHENIX as the central and

muon arms only have a nominally stable acceptance when the collision occurs within 30 cm of the IP.

At current luminosities, the vast majority of the collisions cannot be stored, it is not enough to simply require the presence of a collision to store it. Care must be taken such that the remaining data contains a high concentration of events that are of interest in the physics analyses. To achieve this goal, triggering is expanded to include the topology of the event. In the case of the central arms, where the common probe is the electron, a trigger decision can be performed on the energy sum in square groups of 4 or 16 towers in the electromagnetic calorimeter. If the energy sum passes a programmable threshold and there is activity in the RICH then the event is considered to have a candidate electron. This does not guarantee that the event will indeed contain an electron as the efficiency of the trigger is not 100%, but will instead have a high probability of containing an electron. The trigger circuit is known as the ERT, or the EMCAL-RICH trigger. Alone, the ERT does not provide any vertex information and to increase the rejection, the number of events that are discarded, the ERT is combined with the BBC trigger with a logical AND of the two trigger signals.

For the muon arms, the MuID provides the ability to trigger on the presence of highly penetrating roads by combining signals from Iarocci tubes that form roads that originate from a reasonable vertex location into logical subsets. A trigger signal is then formed by imposing that hits be present in certain MuID gaps. Typically, a highly penetrating trigger primitive, "deep" in colloquial PHENIX terminology, is formed by requiring a hit in one of the first two gaps and another hit in one of the last two gaps, though less restrictive requirements can be placed upon demand. To trigger on the possible presence of a dimuon, a trigger is formed that requires two separate logical subsets of the MuID trigger subsystem to have deep-qualified primitives.

The MuID, unfortunately, has a timing window which is two beam crossings wide. Generally, this has been mitigated by using the MuID triggers in coincidence with a BBC trigger which will correctly identify the crossing with a collision. However, if two collisions occur in two adjacent crossings then there will be ambiguity as to which crossing contains the muon, or dimuon, candidate as the BBC will fire for both crossings even though only one will contain the true muon trigger. This is a particular concern for the Run13 running period of PHENIX as the average number of collisions per crossing is substantially greater than unity and thus there is a high probability to have collisions in adjacent crossings. The recently installed RPC detector upgrades [38, 39] add precision timing information to the possible trigger combinations and can remove all such ambiguities, albeit in a reduced acceptance where the RPC and MuID overlap. In addition to the MuID and RPC, the MuTr has been instrumented as a trigger to select muon candidates having a particular sagitta, or deviation from a straight track at an intermediate tracking station, and therefore add momentum selection to the trigger. As part of the work in support of this thesis the addition of the Forward Silicon Vertex Dectector (FVTX) to the trigger system has been explored to improve the rejection of backgrounds by adding information prior to the absorber and is explained in detail in section 5.3.

Chapter 5

The Forward Silicon Vertex Detector (FVTX)

The Forward Silicon Vertex detector (FVTX) is a precision silicon tracking detector installed as an upgrade to the PHENIX experiment. It covers a similar pseudorapidity range as the existing muon arm detectors and extends the capabilities of those subsystems to perform precision leptonic measurements in the forward region. Here we will discuss the physical characteristics of the detector and the physics capabilities of the detector as designed. The unique data acquisition system (DAQ) will be described as well as the extensions to the capabilities of the FVTX that the DAQ structure has enabled.

5.1 Design Overview
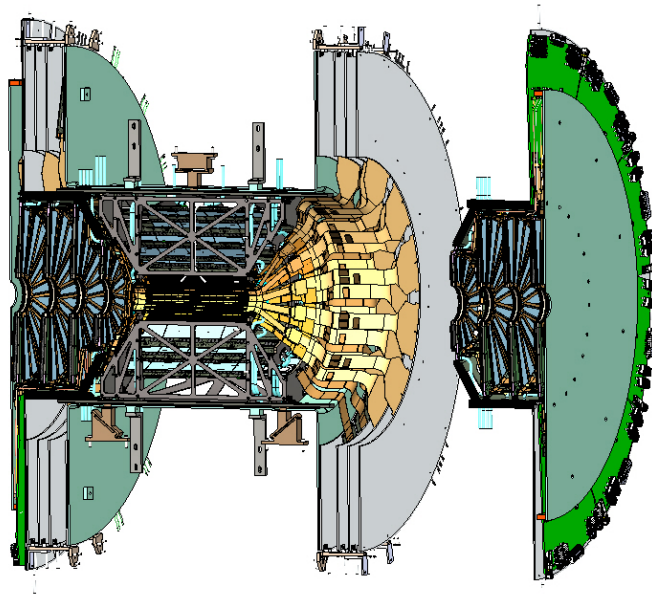
Figure 5.1: A drawing of the combined VTX/FVTX assembly.
One FVTX quadrant is displaced for clarity.

The FVTX detector system is composed of two identical endcap sections, located
on either end of a 4-layer barrel silicon vertex detector (VTX) [40], and in front of
the north and south muon spectrometer arms. Each endcap has 4 layers of active
silicon sensors arranged in a disk around the beryllium beam pipe. The basic unit
of construction is a *wedge*, (section 5.1.6.1) each of which carries a mini-strip silicon
sensor (section 5.1.2), read-out chips (section 5.1.3), and a high-density interconnect
(HDI, section 5.1.4). Wedges are mounted on *half-disks* (section 5.1.6.2), and fitted
with extension cables. For simplicity, the half-disks are referred to as *disks*. Disks
are mounted into *cages* (section 5.1.6.3), and the extension cables are connected to
ROC boards (section 5.1.5), the read-out cards that are the first stage in the data
path. Finally the cage+ROC assembly is installed in the carbon-composite frame
which also contains the VTX components.

Table 5.1: Summary of design parameters

Silicon sensor thickness (μm)	320
Strip pitch (μm)	75
Nominal operating sensor bias (V)	+70
Strips per column for small, large wedges	640, 1664
Inner radius of silicon (mm)	44.0
Strip columns per half-disk (2 per wedge)	48
Mean z-position of stations (mm)	$\pm$201.1, $\pm$261.4, $\pm$321.7, $\pm$382.0
Silicon mean z offsets from station center (mm)	$\pm$5.845, $\pm$9.845

Fig. 5.1 shows a model of two quadrants of the detector, with one FVTX quadrant displaced in z for clarity. The wedges, mounted on the disks, are shown installed into their cages. The VTX and its associated electronics are shown in the middle, mounted in the support frame. As can be seen in the figure, each cage has one small and three large disks. The smaller disks are simply truncated versions of the larger disks. A summary of the FVTX design parameters is given in Table 5.1.

5.1.1   Electronics

This section describes the electrical components and support systems used to read out and power the FVTX. The silicon mini-strip sensors and the FPHX read-out chips are described in sections 5.1.2 and 5.1.3, respectively. The HDI that provides power, bias voltage, and slow control signals to the sensor is discussed in section 5.1.4. The read-out cards and front end modules which process signals from the detector are discussed in section 5.1.5.

5.1.2   Sensors

The silicon mini-strip sensors were designed at Los Alamos and fabricated by Hamamatsu Photonics KK. The wedge-shaped geometry comprises two individual columns

of strips that are mirror images about the center line on the same sensor. The wire bond connections between the strips and read-out chips are located along the outer edges of the sensor (see Fig. 5.2). The centerline gap between columns is 100 μm and is completely active.
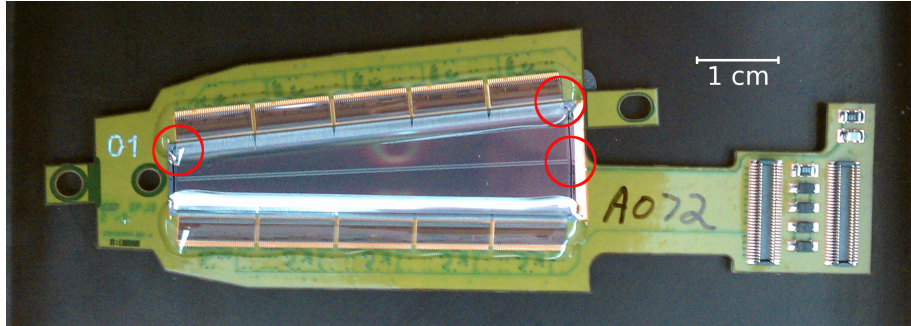
Figure 5.2: A completed FVTX small wedge, with sensor facing up. Note the center line dividing the two halves of the sensor and rows of FPHX chips along the sensor edges.

The strip length increases with radius on the sensor, and goes from 3.4 mm at the inner radius to 11.5 mm at the outer radius of a large wedge, with a pitch of 75 μm in the radial direction. Each sensor covers 7.5° in ϕ, and since the strips are perpendicular to the radius, they make an angle of 86.25° with respect to the centerline, as can be seen in Fig. 5.3.

The sensors were fabricated with p-implants on a 320 μm thick n-type substrate. The strips are AC-coupled and biased through individual 1.5 MΩ polysilicon resistors to a typical operating voltage of +70 V to completely deplete the silicon. The metallization on the strips is wider than the implant to provide field plate protection against micro-discharges, a concern that becomes greater with radiation-induced increases in the leakage current. The strips are also protected by two p-implant guard rings and an n$^+$ surround between the guard rings and sensor edge. There are two sets of bond pads for each strip, one of which is dedicated to probe tests. Fig. 5.3 shows details of the sensor layout, including guard rings, bond pad locations, and

mechanical fiducial marks used for alignment.
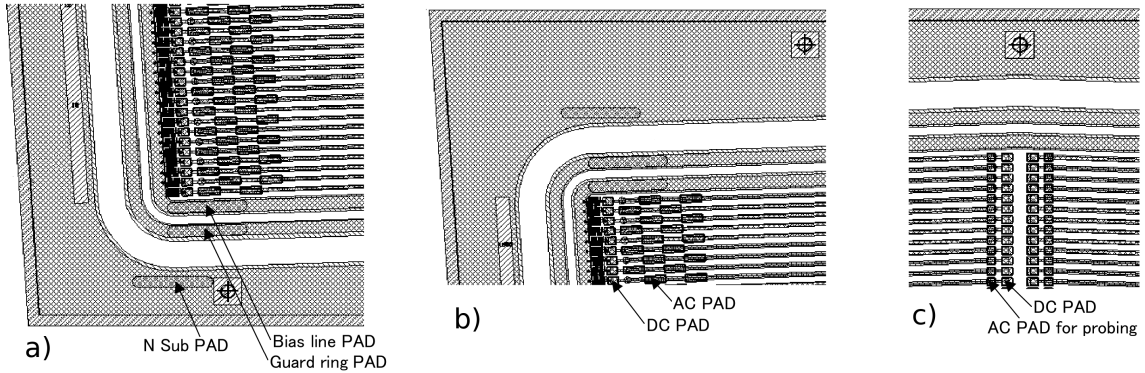
Figure 5.3: Details of the sensor layout. a) Narrow end corner, b) wide end corner and c) wide end center. These areas correspond to the circled regions in Figure 5.2.

5.1.3   FPHX Chip

A custom 128-channel front-end ASIC, the FPHX, was designed by Fermilab for the FVTX detector [41, 42]. The chip was optimized for fast trigger capability, a triggerless data push architecture, and low power consumption. The chip was fabricated by the Taiwan Semiconductor Manufacturing Company (TSMC) with 0.25 μm CMOS technology. The analog section consists of an integrator/shaper stage followed by a three-bit ADC. A single FPHX chip mounted onto the HDI is shown in Fig. 5.4. In this example, the wire bonding to the control lines on the HDI is complete, but no bonding between the sensor and the chip has been performed.
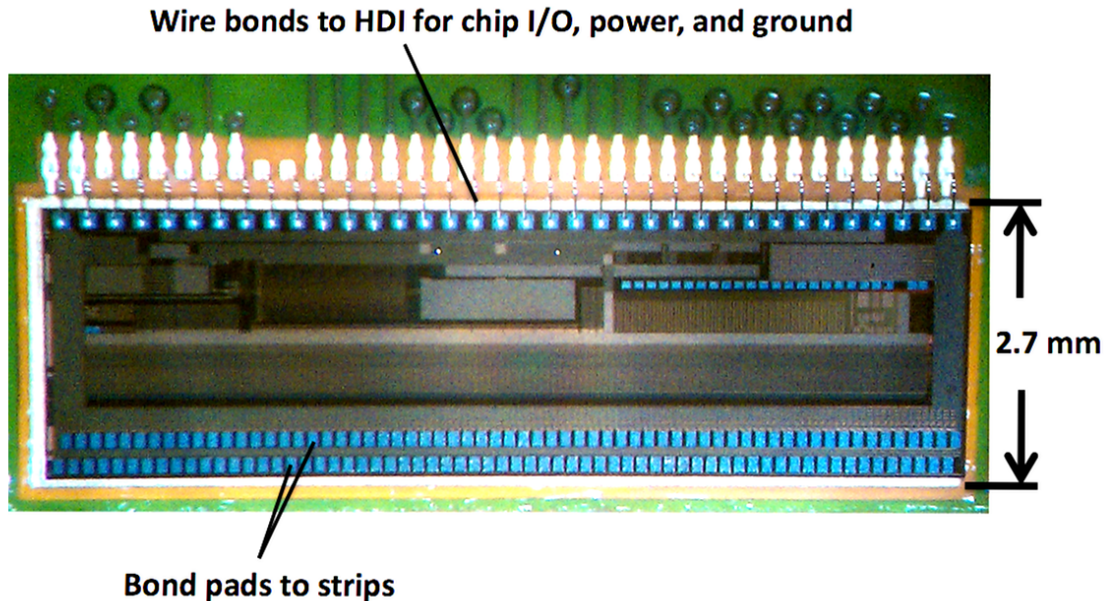
Figure 5.4: A single FPHX chip mounted onto the HDI. Along the top, wire bonds to the HDI have been completed. Along the bottom, in two rows, are 128 bond pads for wire bonds to the silicon strips.

The FPHX chip was designed to process up to four hits within four RHIC beam crossings (or ~4×106 ns = 424 ns). Each hit contains a 7-bit time stamp, 7-bit channel identifier, and a three-bit ADC value. By only accepting hits above a certain (programmable) ADC threshold, the signal-to-noise ratio can be dynamically optimized for different operating conditions. In addition, the ADC information from strips in an FVTX hit cluster is used to determine the center of the track via a weighted average of the charge in each strip. An ADC with higher resolution would not significantly improve the detector's tracking resolution, since multiple scattering in detector material is the dominant contribution to track smearing at the ~20 μm level.

The data words are output over two LVDS serial lines at up to 200 MHz clock rate. The total power consumption of the FPHX is ~390 μW per channel. The

noise, when the chip was wire bonded to a sensor with strips ∼2–11 mm in length (∼1-2.5 pF) was simulated and measured to be below the design specification of 500 electrons.

5.1.4   High-Density Interconnects

The silicon sensor and FPHX read-out chips are assembled on an HDI which provides the slow control, power, and bias input lines as well as slow control and data output lines. The HDI stack-up is shown in Fig. 5.5 and consists of seven layers of single-sided (20 μm) and double-sided (50 μm) copper coated polyamide bonded together with a 25 μm sheet adhesive for a total thickness of approximately 350 μm. Indicated on the HDI stack-up are two signal layers, one ground layer, and one power layer. All control lines (which are not active during data taking) are routed under the sensor, and all output lines are routed towards the edge of the wedge, thus minimizing the coupling between the output lines and the sensor. The number of lines (8 pairs for the control lines and 2 signal pairs per chip for the output lines) requires that they have a 40 μm width with a 100 μm spacing. Both simulated and physical tests were carried out to ensure that the input clock (200 MHz) had sufficient integrity at the furthest point from the driver.

Since the layout of the wedge, chip, and HDI can impact the system noise, the electrical layout of the wedge assembly was designed to minimize any additional noise. Incorporated onto the HDI were two noise-canceling loops, one for the input side and one for the output side of the chip, employing bypass capacitors connected to the bias ground and digital ground, respectively. Termination resistors for the calibration lines and bias resistors and capacitors are also located on the board.
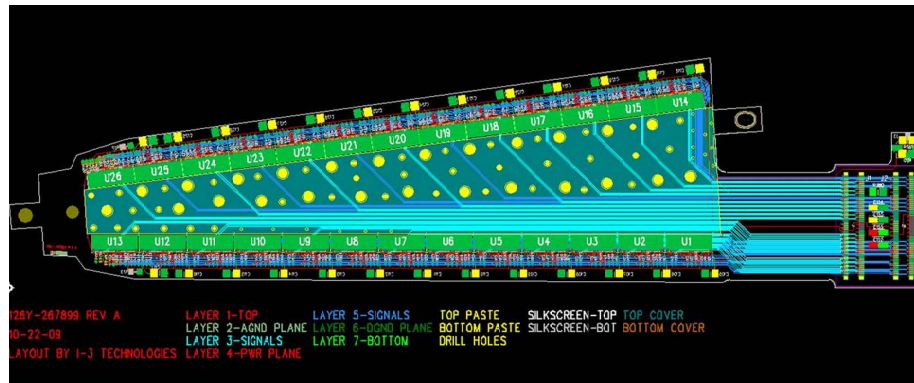
Figure 5.5: Schematic of the HDI stack-up.

5.1.5   ROCs/FEMs

The design of the read-out electronics for the FVTX detectors is based on three major constraints, imposed by the detector:

- Large instantaneous bandwidth (3.38 Tb/s)

- Radiation hardness of read-out components near the interaction point

- Large number of I/O lines (21,000 LVDS pairs)

As a result, the read-out electronics are logically divided into two independent blocks, illustrated in Fig. 5.6. The components are:

- Read Out Card (ROC) - module which is located close to the detector.

- Front End Module (FEM) - module which is located in the Counting House ($\sim$50 m from the Interaction Region) in a standard VME crate.

- FEM Interface Board - module located in each of the FEM VME crates.

The output of the FEM connects to the standard PHENIX DAQ board, a Data Collection Module (DCM), and from this point on the data stream becomes a part of the standard PHENIX DAQ.
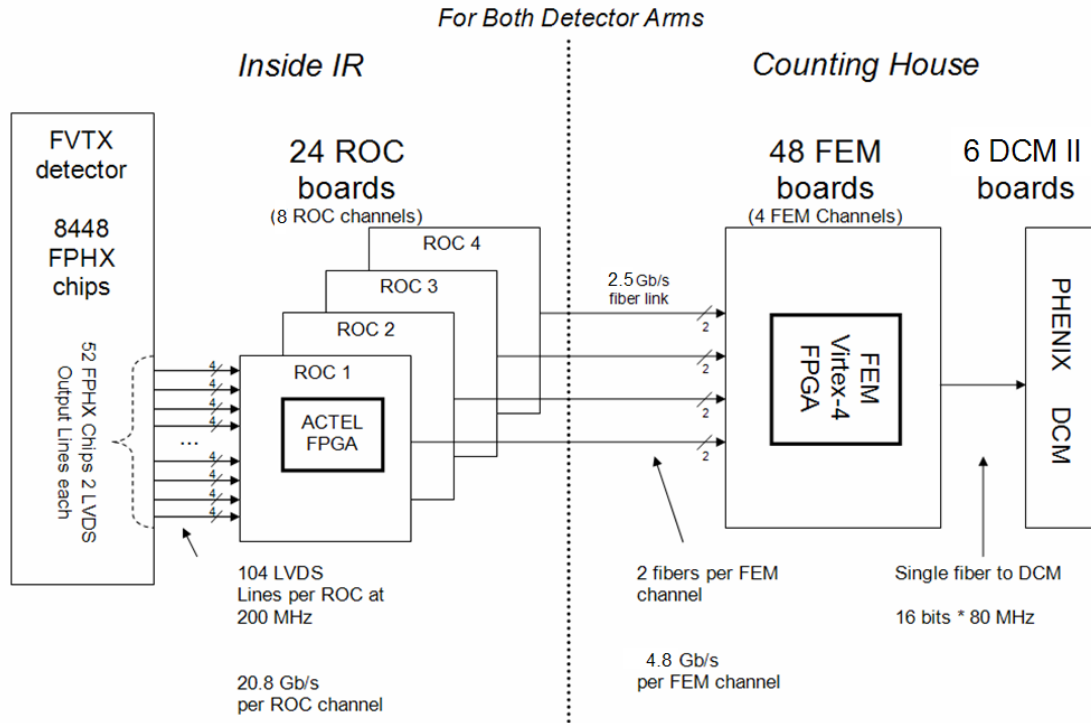
Figure 5.6: Read-out electronics block diagram.

5.1.5.1 Read Out Card (ROC)

The ROC boards are mounted on an aluminum cooling plate and connected to the HDIs through the extension cables.

The ROC boards are designed to:

- Receive data via LVDS pairs from the silicon read-out chips

- Combine and synchronize the data streams from multiple FPHX chips

- Send the data to the front end module (FEM) in the counting house via optical fibers

- Receive and distribute slow control data to/from the FPHX chips and other ROC components

- Hold an on-board calibration system for the FPHX chips.

- Hold an on-board JTAG FPGA which allows for remote programming of the slow control and data FPGAs from the counting house
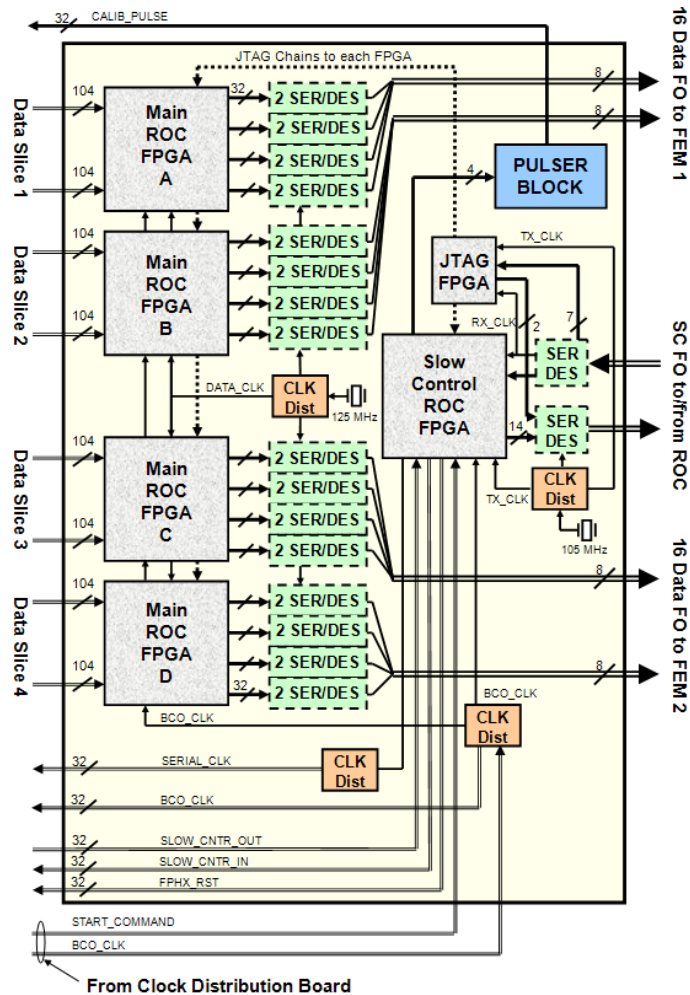
Figure 5.7: Block diagram of the ROC board.

The ROC board design utilizes radiation-hard FLASH-based ACTEL ProASIC3E FPGAs in order to limit susceptibility to single event upsets (SEUs). A functional ROC board diagram is shown in Fig. 5.7. Each board contains 4 large-scale ACTEL A3PE3000-FG896 FPGAs to process the data from the read-out chips, 33 16-bit Serializer/Deserializer chips (TLK2711) and four 12-channel optical fiber transmitters (HFBR-772BEZ) to send the data to 2 FEM boards. Each ROC FPGA holds two completely independent ROC channels, for a total of 8 ROC channels per board, which send out 32-bit data at the output clock frequency of 125 MHz.

The Beam Clock (9.4 MHz) arrives at the ROC board as an LVDS signal and is distributed to all the FPGAs on the board as well as to all the FPHX chips. A Serial Clock of 20× the Beam Clock frequency is generated by a PLL on the slow control FPGA. The output data from the FPHX chips are phase latched to a similarly generated 20× clock inside the Main FPGAs, which avoids distribution of the fast clock between FPGAs and simplifies the design.

A schematic of a single ROC Channel is shown in Fig. 5.8. The main task is to combine data from up to 10 FPHX chips into a single data stream without any delay: 20-bit data deserialization gives time for this. Three of those streams are combined by a 3-to-1 Round-Robin Arbiter and buffered into an output FIFO. We utilize triple redundancy on every component that allows for it, and actively use design blocks for predictable layout and timing. The design is latch free by construction, with constant synchronization of the input serial data streams.

The ROC board includes a calibration system that can deliver a precisely controlled voltage pulse to each FPHX chip on an HDI. The signal injection timing is synchronized with the Beam Clock. A 10 bit dual DAC is used together with a precision reference and analog switches to provide a large dynamic range and low noise. The amplitude is adjustable via the slow controls, while a fast rise and slow fall time are fixed by RC circuits. The calibration system is used routinely to check

for dead FPHX channels and determine the electronics noise levels. When disabled, the system contributes negligible noise to the FPHX chips.
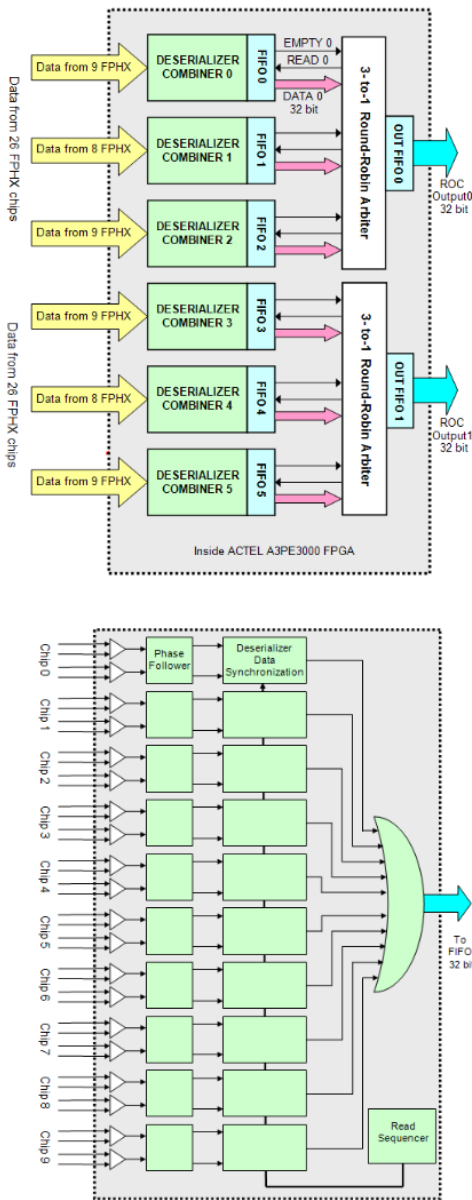
Figure 5.8: Block diagram of a single ROC channel and a single 10-chip channel deserializer/combiner.

5.1.5.2 Front End Module (FEM)

The FEM boards are located in 6U VME crates in the counting house (in a shielded location ~50 meters from the detector) where radiation levels are negligibly small and SRAM-based FPGAs can be used. The FEM boards are functionally designed to:

- Receive data from the ROC boards over fiber links.

- Sort the incoming data according to the Beam Clock Counter.

- Buffer the data from the last 64 beam clocks.

- Upon Level-1 trigger decision, ship the data from the Beam Clock of interest to the output buffer, which ships data to the PHENIX Data Collection Modules (DCM).

- Distribute and receive slow control data to/from the ROC cards. The online slow control interface is made through the FEM Interface Board and the interface to the ROC cards is made through an optical fiber.
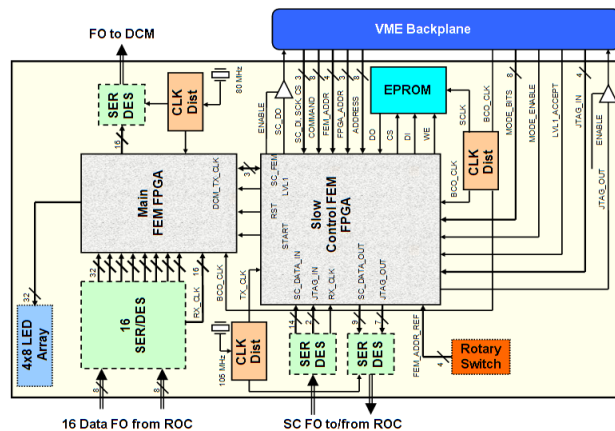
Figure 5.9: Block diagram of a FEM board.

The FEM board architecture can be seen in Fig. 5.9. Xilinx Virtex-4 FPGAs are used as the main FEM FPGA. The largest device of the memory-intense SX series (XC4VSX55) provides enough fabric and memory to implement 4 FEM channel cores and a channel combiner on a single FPGA. This significantly reduced the cost of the FEM board design.
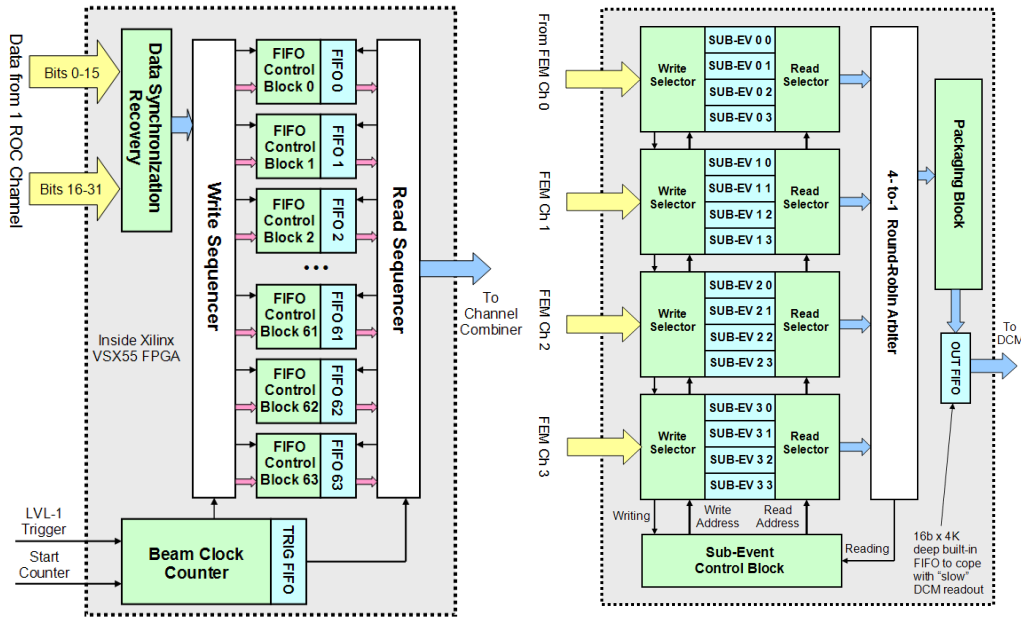
Figure 5.10: Block diagram of a single FEM channel and a channel combiner.

A block diagram of a single FEM channel and FEM channel combiner is shown in Fig. 5.10. One FEM board receives 16 optical fibers (from half of a ROC board). Data are buffered for 64 beam clocks in each of the 4 FEM channels in an array of 64 512 word deep FIFOs. Each FIFO stores the data for a particular beam bucket (0 through 63). Since data from the FPHX chips carry the 7-bit beam clock counter information, the sorting is trivial.

5.1.5.3 FEM Interface Board

Each VME Crate with 12 FEM boards is controlled by a single 6U FEM Interface Board which acts as a simple crate controller and is designed to:

- Receive GTM (beam clock and trigger) signals.

- Distribute the information from the GTM to the FEMs via the VME backplane.

- Distribute the Beam Clock to a set of ROCs via a front-panel fiber optic interface.

- Distribute a START signal to a set of ROCs via a front-panel, to allow the FEM and ROC read-outs to be synchronized.

- Interface to the PHENIX Online slow controls system via Ethernet or USB, and to the FEM boards via the VME backplane.

The full block diagram of a FEM Interface Board is shown in Fig. 5.11.
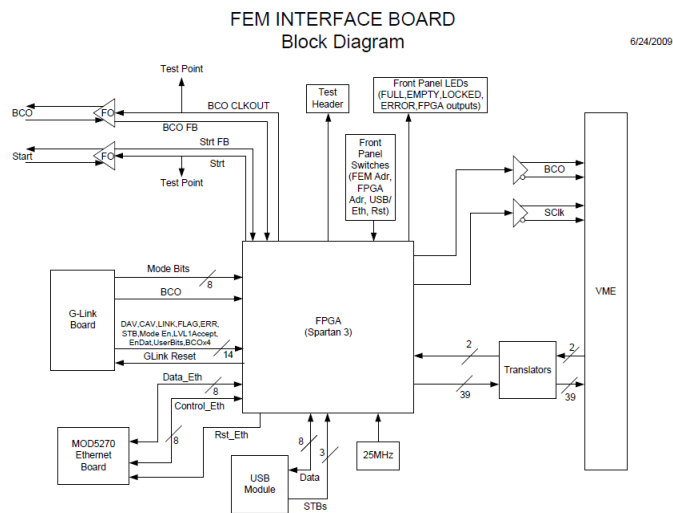
Figure 5.11: Block diagram of the FEM Interface Board.

5.1.6 Mechanical Design

Here we describe the mechanical design of the FVTX and the procedures used to assemble the various components into a complete detector.

5.1.6.1 Wedges

Silicon sensor, 320 μm

FPHX read-out chips

HDI, 350 μm

Carbon back-plane, 1.56 mm, K13D2U with EX1515 resin

Spacers – POCO graphite, AXM-5Q

Separate ground connection point for carbon

Hirose DF18 series connector

Hirose HFL series mini-coax for bias
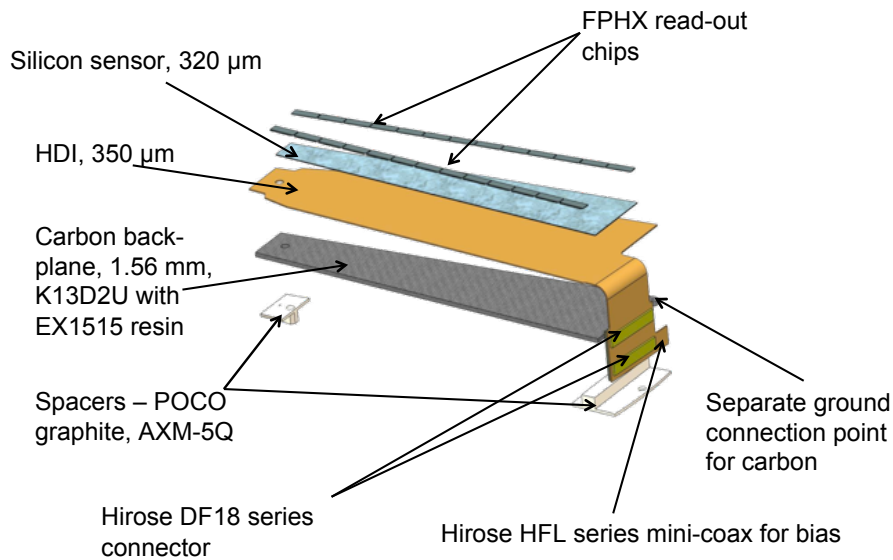
Figure 5.12: Exploded view of an FVTX sensor assembly.

A *wedge* is the basic construction unit of the FVTX detector. Fig. 5.12 shows an exploded view of a single wedge assembly, which consists of a silicon mini-strip sensor (Section 5.1.2), FPHX read-out chips (Section 5.1.3), a high-density interconnect bus (HDI, Section 5.1.4), and a carbon support backplane.

Assembly of wedges took place at the SiDet Facility at Fermilab. A series of precision assembly fixtures were used to affix the HDI onto the backplane, to place the FPHX read-out chips on the HDI+backplane assembly, and finally to attach the silicon sensor to the chip+HDI+backplane stack. At each assembly step, two fixtures used vacuum to hold the relevant components in place. Pins and holes on

the fixtures aligned the components as they were brought together, and pressure was applied between the two fixtures to ensure complete bonding between the components and adhesive. Fig. 5.13 shows a wedge assembly in progress.
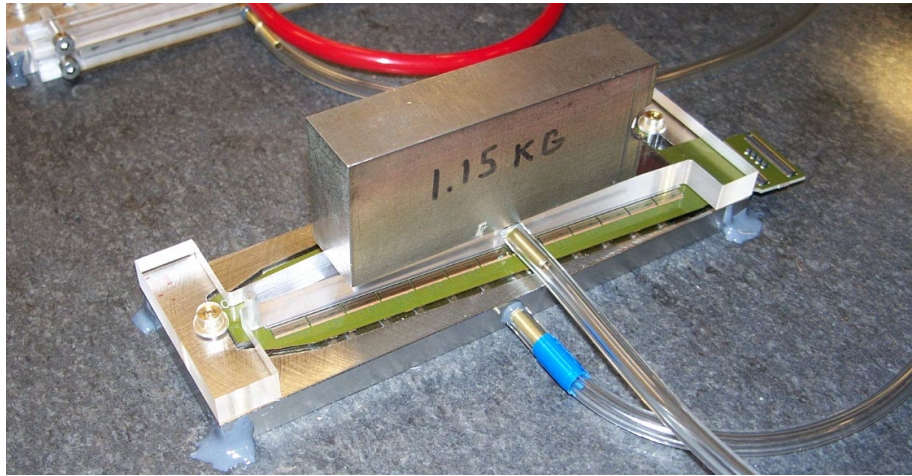
Figure 5.13: Assembly fixtures in use. At this step, the silicon sensor is being placed onto the FPHX chip+HDI+backplane assembly.

After the HDI and backplane were assembled, a different set of assembly fixtures was used to place the FPHX chips in position on the HDI. Large wedges have 13 chips on each side, while small wedges have 5. After placement the chips were wire bonded to the HDI and tests were performed to ensure proper function. A similar procedure was then used to attach the silicon sensor to the chip+HDI+backplane assembly with Arclad adhesive. Completed wedge assemblies were then shipped to Brookhaven National Laboratory for final preparation and installation.

Further operations were needed before a wedge was ready to be mounted onto the disk support plane. A small ground wire was attached with conductive silver epoxy to a small hole in the carbon plane, and connected to ground on the HDI. This serves to drain off charge that may build up on the carbon backplane. Next, graphite feet (Poco Graphite) were glued to the underside of the carbon plane. Finally, the HDI

was bent through 90° near the connector end using a thermal bending apparatus that heated the kapton-copper HDI to 100°C, in order to permanently form it to match the cage shape.

5.1.6.2 Disks

The wedge support disks are flat sheets of 0.4 mm thick thermally conductive carbon fiber on both sides of a carbon-loaded PEEK plastic frame. The PEEK at the outer radius contains a cooling channel, with nylon hose barb fittings at the ends, which removes heat generated by the FPHX chips. PEEK buttons maintain the spacing between the face sheets. Fig. 5.14 shows an exploded view of a disk assembly.
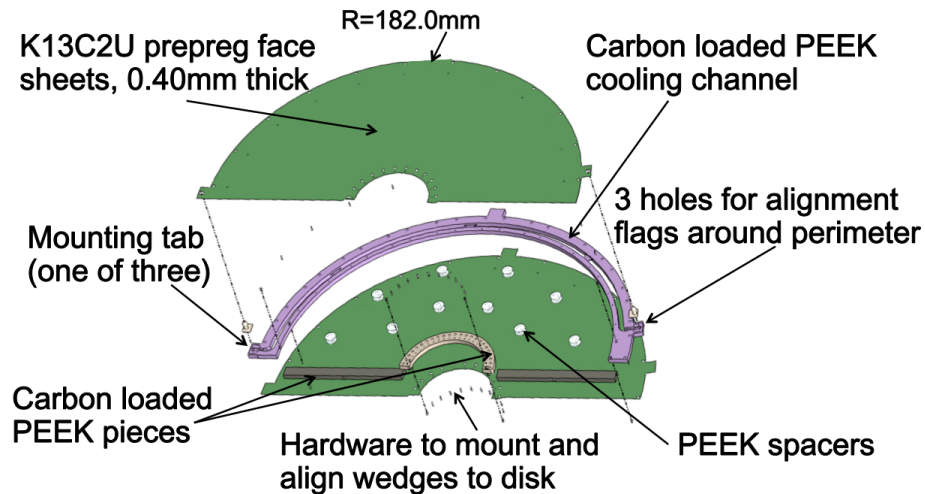
Figure 5.14: Exploded view of a support disk.

On both faces of the disks, precision alignment pins are located along the inner and outer radii, one pair for each wedge which will be mounted on the disk. These pins match a precision hole and slot in the graphite feet of the wedges, assuring placement of the wedges onto the support disk with an accuracy of 25 μm. Wedges are secured onto the disk with small PEEK screws near each of the alignment pins.

The silicon sensor on each wedge subtends an angle of 7.5°. Adjacent wedges on a disk overlap in the azimuthal direction by 0.5 mm to give hermetic coverage in the azimuthal direction. Since the HDI is significantly wider than the silicon sensor, the wedges must be staggered in z to allow this continuous azimuthal coverage by the sensors. This is achieved by mounting wedges on both sides of the disks, at alternating z positions on each side. The graphite feet on the back of the wedges come in two varieties so that wedges can be alternately mounted at 0.9 mm or 4.9 mm above the surface of the disk.
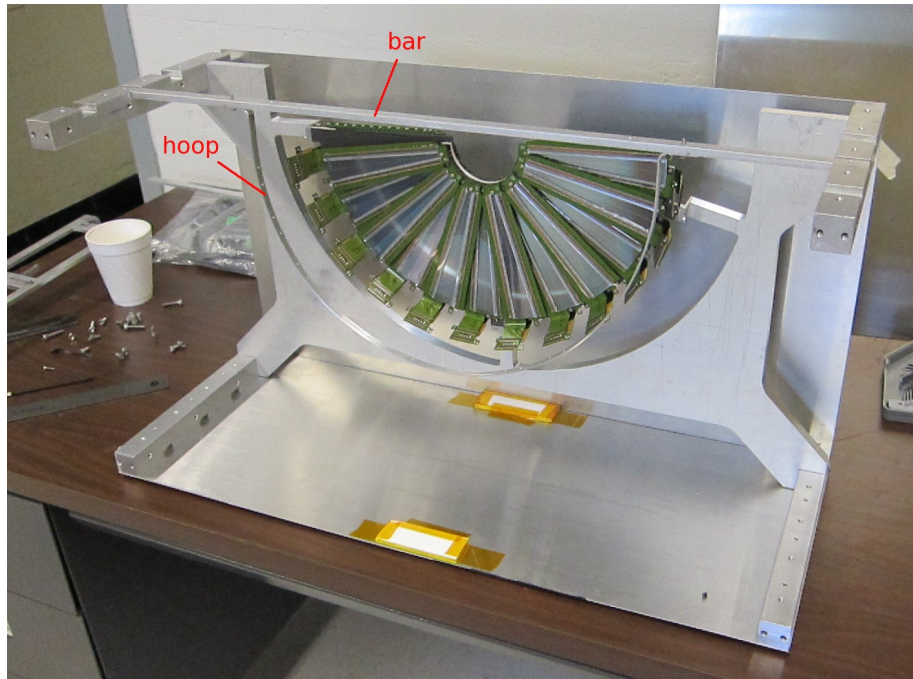
Figure 5.15: A populated disk in its support frame. Some of the cover sheets are in place. The hoop will support the extension cables that will be connected to the wedges prior to installation in the cage.

After each disk was fully populated with wedges, the positions of the wedges were precisely measured by Hexagon Metrology using an optical coordinate measuring machine. Fiducial marks, four on each silicon detector, were measured with an

accuracy of 5 μm in the plane of the silicon, relative to the three precision mounting points on the perimeter of the disk.

The disks were mounted into a cage on the three precision mount points located on the outer radius of the disk. To maximize the detector's ϕ resolution, each of the four disks are mounted into the cage offset in ϕ by an angle $3.75°/4$ with respect to the neighboring disk.

5.1.6.3   Cages

The cages, into which disk assemblies are mounted, are carbon-composite structures fabricated from CN60 carbon fabric. One of these cages is shown in Fig. 5.16 with four mounted disks (without wedges). During construction, the cage was mounted in an assembly structure that also supported the aluminum cooling plate onto which the ROC boards (6 per quadrant) are mounted, as shown in Fig. 5.17. A soft, thermally conductive pad, approximately 1/8 in thick, is placed between the ROC and the cooling plate to improve heat transfer. Each disk is mounted into a cage on three mount points, each of which has an alignment pin. First the small disk was mounted, and extension cables connected to the ROC boards, followed by the three large disks in turn. At the inner radius of the ROC boards, pairs of connectors can be seen, one pair for each wedge/extension cable. A completed half-detector is shown in Figure 5.18.
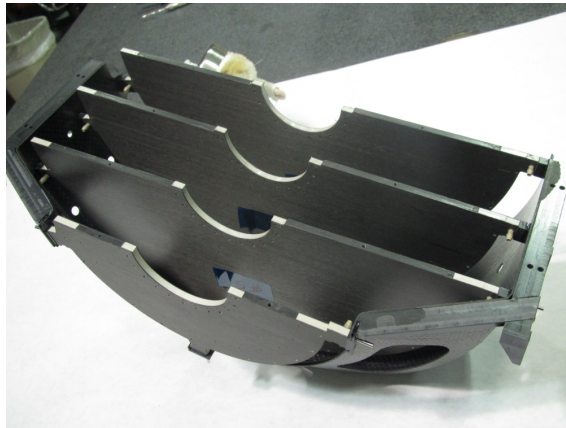
Figure 5.16: A cage with all four disks installed. No wedges have been placed on the disks.
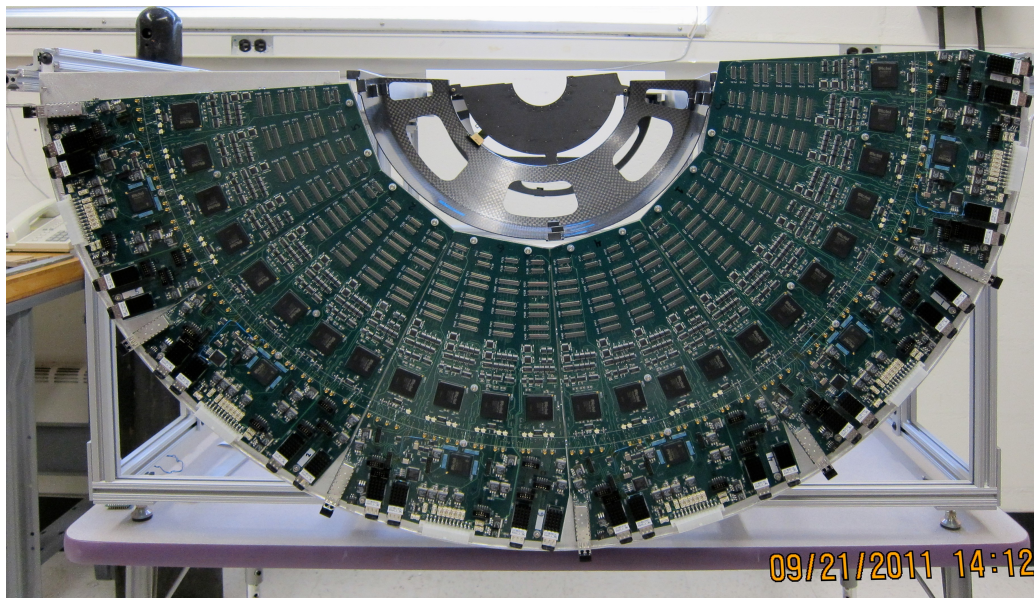
Figure 5.17: A cage and ROC boards on an assembly frame. An unpopulated small disk is mounted at the rear of the cage.

During the selection for the support materials several factors were considered: low radiation length is desirable to minimize interactions in detector materials; high rigidity is necessary for maintaining alignment and stability of detector components;

ease of machining and availability are important for construction. Candidate materials for the FVTX support structures were beryllium, glass fiber reinforced polymer, and carbon-carbon composite.

The vibrational mode frequencies, gravitational load distortions, and shape changes with temperature were studied for all mechanical structures, and used to verify that the dimensional stability requirements were met.
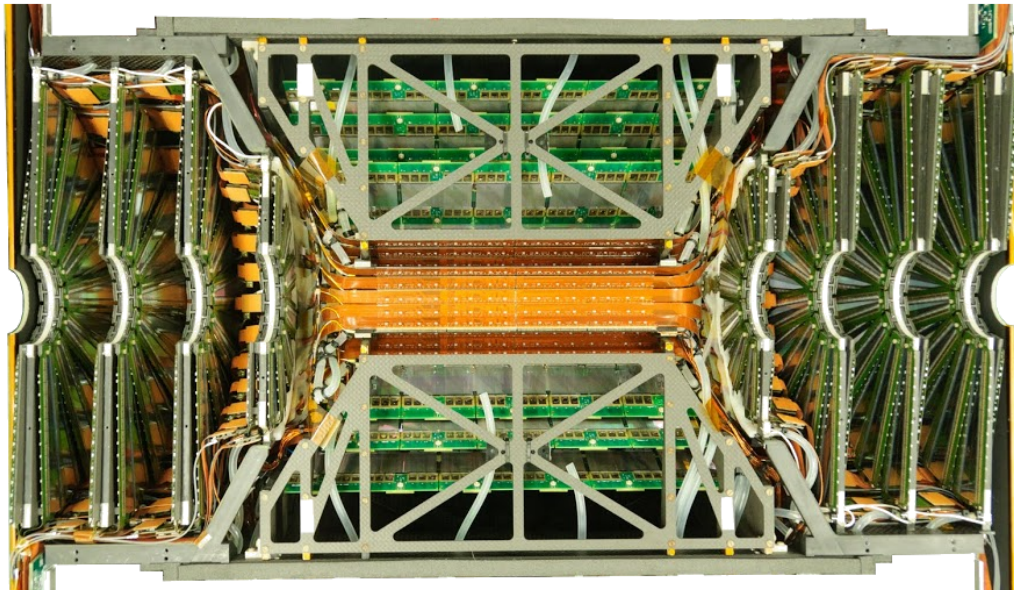
Figure 5.18: A completed half-detector, with the VTX barrels in the center, and the two FVTX endcaps on either end. The overall length is 80 cm.

5.2 Physics Capabilities

This section presents performance benchmarks from the FVTX, using data collected during operation at RHIC.

5.2.1 Timing
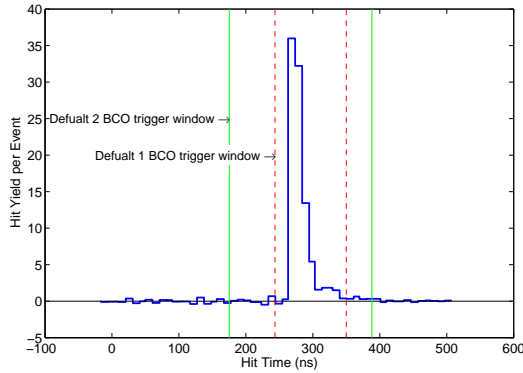
Figure 5.19: Timing distribution of the FVTX hits relative to the RHIC beam clock.

The distribution in time of FVTX hits is studied relative to the RHIC collision time by comparing the hit rate at different FVTX delay values relative to the RHIC beam clock. The timing distribution for two sectors of wedges in the south arm is shown in Fig. 5.19. Most hits fall in a window ∼30 ns wide.

Two standard trigger timing configurations were used during FVTX operation, as shown by the vertical lines in Fig. 5.19: during relatively low trigger rate running (in heavy ion systems) hits arriving in a time window two RHIC beam clocks (BCO) wide (1 BCO∼ 106 ns) are accepted. In high trigger rate $p+p$ running, a 1 BCO-wide window is used to avoid recording accidental hits from neighboring beam crossings (1 BCO apart).

5.2.2 Hit Efficiency

Multi-layer tracking detectors require a large intrinsic hit efficiency in each sensor, that is, a high probability that a particle of interest will produce a measured signal when traversing an active sensor layer. To evaluate this efficiency in the FVTX,

charged particle tracks which are identified by hits in three of the FVTX stations are projected to the fourth station. A hit cluster in the fourth station at the projected position is assumed to be due to the charged track, which is a good assumption for the low occupancy $p + p$ events used in this study.
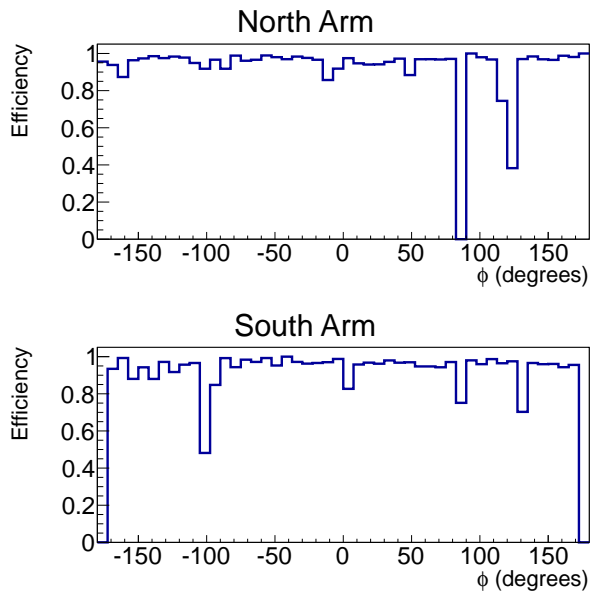
Figure 5.20: Hit efficiency for FVTX station 2 as a function of ϕ.

The probability of finding a hit at the projected spot in station 2 using tracks identified by hits in stations 0, 1, and 3 is shown in Fig. 5.20, as a function of the angle ϕ around the disk, using data recorded during the 2013 RHIC pp run. The extracted efficiencies shown in this plot include the intrinsic efficiency of the detectors as well as any efficiency loss due to dead channels, chips, or DAQ channels. The peak efficiencies are above 95% indicating that the intrinsic efficiency of the detector is quite high. The area near $\phi = 90°$ in the North arm has a low hit efficiency due to a broken component on a ROC board, which prevented several wedges from being read out. However, the overall live area during the 2013 run was greater than 95%.

5.2.3 Alignment and Residuals

Misalignment of the silicon wedges relative to each other and multiple scattering of particles as they pass through the FVTX sensor material have a detrimental effect on the ultimate tracking resolution of the detector. The internal detector alignment was performed using data taken with the PHENIX magnets turned off, so all charged particles travel in straight lines. The MILLEPEDE-II [43] package was used to internally align all detector elements.
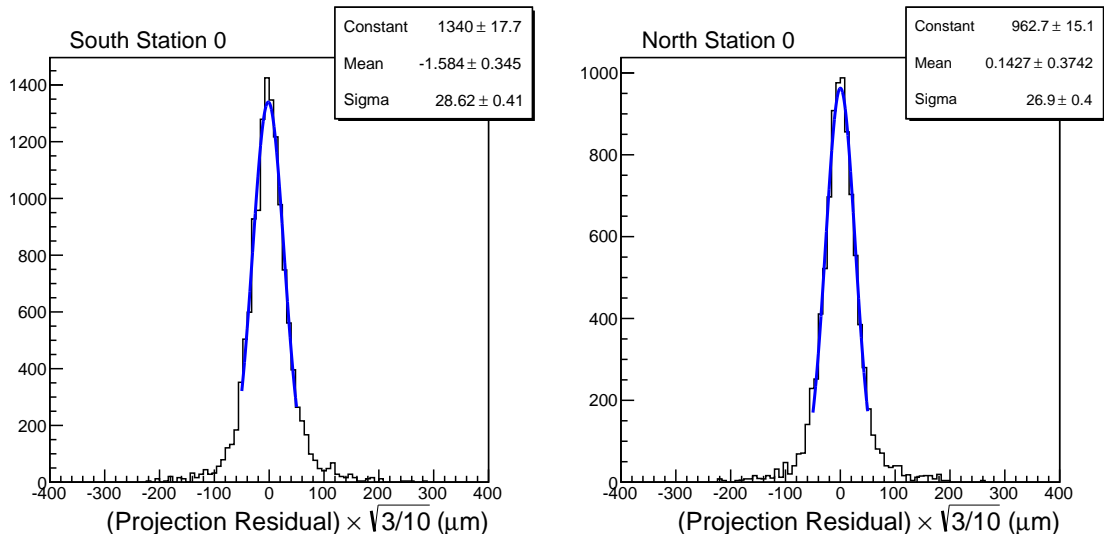
Figure 5.21: Track residuals for the innermost FVTX tracking stations, scaled to give the single hit resolution.

After detector alignment was performed, the FVTX single hit resolution was determined with straight-line tracks found in the FVTX, matched with tracks found in the muon spectrometer, from pp collisions recorded with the PHENIX magnets turned off. These tracks typically have a total momentum $p > 3\,\text{GeV}/c$. After finding tracks with hits in three FVTX stations, the track residual for the fourth station is found by calculating the distance between the track projection and the center of the nearest FVTX hit cluster in that station. The width of this track residual distribution

is determined by the hit position resolution in each station and the distance between tracking layers. To find the single-particle hit position resolution for a single station, a correction is applied to the track residuals, which was determined from linear regression assuming a common single-particle hit position resolution in the three stations used to find the track and a common distance between the stations. The scaled track residuals, which represent the single-particle hit position resolution, are shown in Fig. 5.21 for the innermost tracking station in the north and south arms. The position resolution for each of the eight stations varies between 24 and 28 μm, which is within the design parameters.

5.2.4 Electronic Noise

The FPHX chip was designed to have a relatively low noise of ~500 electrons when wire bonded to the actual FVTX sensor (see section 5.1.3). The electronic noise in the detector is monitored periodically using the calibration system. During calibration, groups of ten signal pulses of a given height are sent to an injection capacitor at the front-end of the read-out chip, while the the signal height is scanned across the discriminator threshold. The noise level is characterized by the broadening of the hit efficiency threshold as shown in Fig. 5.22. A normal cumulative distribution function is used to fit the data. The noise level is parametrized by the width, σ, of the fit function.

A histogram of the noise level for all operating channels is shown in Fig. 5.23. The average electronic noise level is between 350-380 electrons, which is significantly lower than the nominal discriminator threshold of ~ 2500 electrons. This level of electronic noise is well within design parameters of the FPHX chip and read-out system.
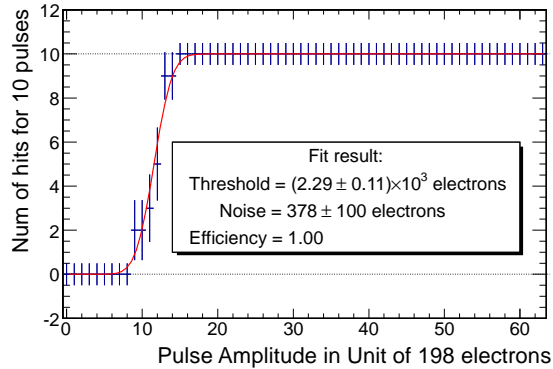
Figure 5.22: Typical calibration data for a single channel (blue points), fit with a normal cumulative distribution function.
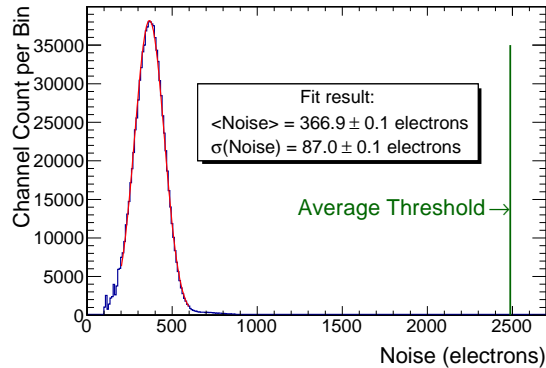
Figure 5.23: Histogram of the noise parameter, σ, for all channels under operating conditions, in a typical calibration run. A Gaussian distribution fit to the data gives a mean noise level of 367 electrons. The nominal discriminator threshold at ~ 2500 electrons is shown by the vertical green line.

5.3 Extensions

In this section we will explore the various extensions that have been made to the FVTX to augment the capabilities of the detector beyond the scope of the original design in both software and hardware. Due to the unique structure of the data acquisition pathway of the FVTX and the flexibility of the FPGA elements used

in the read-out it has been possible to add capabilities to monitor the real-time luminosity of collisions in the PHENIX interaction region. Furthermore, additional designs have been implemented to allow the FVTX to participate in the PHENIX triggering system for the selection of high multiplicity events while working within constraints of the original electronics design.

5.3.1 Tracking

The pattern recognition algorithm that filters and refines the recorded hit information into tracks passing through the detector is an integral part of a tracking detector. The ideal algorithm will be efficient by associating all of the hits deposited by a single charged particle into a track as well as have a high purity by not associating unrelated hits to the track. As can be expected, the ideal algorithm, if it existed, would not be practically feasible due to the finite computing resources that are available. A realistic algorithm must, therefore, strike a balance between maximizing the number of true tracks found while minimizing both the contamination of spuriously associated hits as well as the fake tracks formed from random combinations of hits that have no true relationship. In addition, the algorithm must be computationally efficient in order to enable the analysis of the multi-petabyte data sets that are now common in modern collider experiments such as PHENIX.

The FVTX sits within the poles of the central magnet close to the nominal IP where the magnetic field lines are approximately axial along the beam axis. Therefore, charged particles that pass through the FVTX travel along paths that are roughly parallel to the magnetic field and experience minimal bending. The restriction to straight line tracks greatly simplifies the algorithm selection. This condition also assumes that the multiple scattering of the particle as it passes through the detector is small and does not cause the path of the particle to deviate substantially from a straight line, which is a good approximation for particles capable of pene-

trating the absorber material preceding the muon arms. The Hough transform is a highly efficient pattern recognition algorithm specifically designed to extract straight line features from images or point clouds. The algorithm describes a method to replace the problem of finding collinear points with the mathematically equivalent problem of finding a confluence of lines. The method involves transforming each of the points into a straight line in Hough space. In the most common parametrization [44], a straight line is described by the angle θ of the normal as measured from the origin and the minimum distance ρ from the origin to the line (along the normal). In this parametrization each point in Cartesian space transforms to a sinusoid in Hough space as given by $x \cos \theta + y \sin \theta = \rho$. Therefore, a confluence of sinusoids in Hough space corresponds to a line passing through collinear points as illustrated in Figure 5.24.
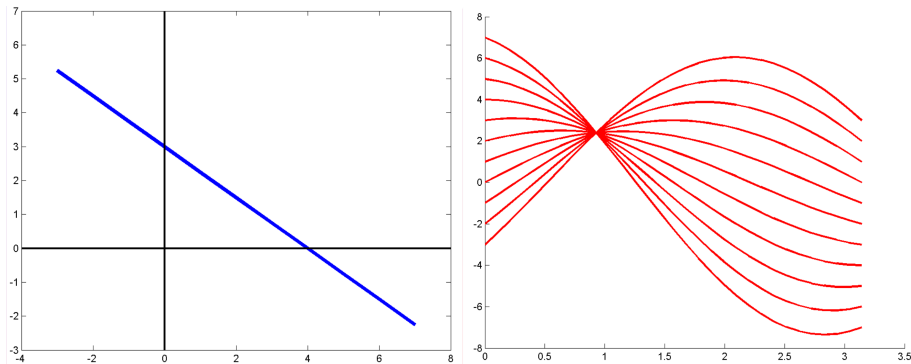
Figure 5.24: A set of collinear points in the Cartesian plane (left) and the Hough transform of a subset of the collinear points (right). The line on which the points are collinear is described by (ρ, θ) at which the sinusoids converge.

In practice, the sinusoids are collected in a discrete accumulator array and bins with counts that are above a certain threshold are considered to be sets of collinear points. The Hough transform, originally designed for image analysis, works best when there are many collinear points, as is the case for pixels in an image. In the case of particle tracking, in particular through the FVTX with only four tracking lay-

ers, the situation is far different where tracks must be identified even when there are three or fewer points available. In this case, the accumulator array is very sparsely filled and the bins containing tracks are very close to the threshold imposed by random crossings of sinusoids. To enhance the signal to background ratio the Hough transform method is applied to hit pairs, rather than individual hits as described in [45], thereby increasing the number of counts in the signal bin. While greatly increasing the efficiency of the algorithm for sparse point clouds, this has the unfortunate side effect of cause the algorithm to increase in computational complexity from $\mathcal{O}(N)$ to $\mathcal{O}(N^2)$ for the two dimensional case.

In heavy ion collisions it is possible to have single events that deposit more than 20000 hits in the detector that correspond to roughly 7000 clusters of hits, and approximately 2000 tracks, given that the average number of hits per track is above three. This is a test of the ability of the algorithm to maintain high efficiency and purity in the presence of a large number of hits. It has been shown that the Hough transform, as implemented, is capable of providing greater than 95% track finding efficiency with more than 90% purity in the highest occupancy environment expected for AuAu collisions at $\sqrt{s} = 510$ GeV with an average processing time per event on the order of 10 ms. This has enabled the FVTX to process an unprecedentedly large heavy ion data set, for PHENIX, collected in 2012 and 2014.

In pp collisions, the problem is quite different. Occupancy is very low, with at most a few hundred hits collected per event. However, the high rate brings with it a large number of crossings that contain multiple collisions. In a crossing with multiple collisions all of the event vertexes must be identified for proper event characterization and momentum reconstruction. The high computational efficiency of the Hough transform algorithm has allowed for more complete tracking strategies to be implemented and extend tracking through the FVTX detector to a vertex range that includes particles originating from outside of the detector volume ($|z| > 30$ cm).

Hit information from the adjacent barrel vertex detector is now able to be included to expand the tracking acceptance by up to 30%. In addition, the precision vertex determination allows for a secondary tracking pass to be performed that includes particles depositing only two hits in the active detector volume that also point closely to a reconstructed vertex, further increasing acceptance. With these tracking enhancements the FVTX has demonstrated the ability to reconstruct up to 5 event vertexes from a single crossing and correctly associate reconstructed tracks with each vertex up to $|z| < 150$ cm. These enhancements have proven vital for precision measurements in the muon arms in both pp and heavy ion environments.

5.3.2   Luminosity Monitor

For certain precision measurements made relative to the number of collisions, namely spin asymmetries, it is imperative to know very well the number of collisions that have occurred. In particular, as we will later see in detail, it is necessary to quantify this very precisely when we are looking for small differences in production rates of a given probe for differering helicities of the colliding protons. In order to distinguish the spin dependent behavior from a simple imbalance in the bunch luminosities for each helicity combination we must quantify the luminosity imbalance through a metric known as relative luminosity (discussed in more detail in section 6.5).

An ideal luminosity monitor is one that only counts a collision when one has actually occurred, one that always counts a collision whenever one occurs, and one that is capable of tracking the luminosity with the same vertex sampling as is used in the final physics analysis. To expand, the ideal luminosity monitor is, therefore, free of noise in both the sense of detector noise and also backgrounds that are not collision related. It is also capable of counting multiple collisions within the same bunch crossing. The BBC and ZDC (subsection 4.2.3) coincidences (meaning both the detector elements that are to the north as well as those to the south of the inter-
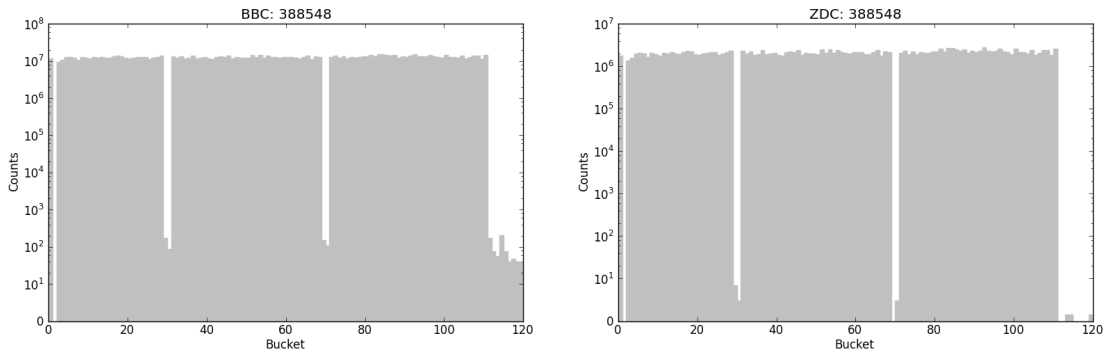
Figure 5.25: Usage of the BBC and ZDC detectors for luminosity monitoring.

action region must be activated) provide two independent measures of the collision rate that mostly satisfy the requirements of an ideal luminosity monitor. They both do suffer from backgrounds that are not collision related, but as seen in Figure 5.25 the background fractions are quite small. More importantly, as they are coincidence detectors with timing information, it is possible to restrict the luminosity according to a certain vertex region to match the cuts used in an analysis. However, since they are coincidence detectors they are not capable of counting the number of collisions per crossing, but rather the number of crossings where there were one *or more* collisions. Additionally, the crossing counts are scaled by the a factor that represents the efficiency of the detectors for detecting a collision.

As previously discussed in subsection 5.1.3 and subsection 5.1.5 the FVTX diverges from the traditional, analog buffering read-out architecture. The FVTX offers continuous digitization of charge depositions that pass a programmable threshold. Therefore, all of the (above threshold) hits are guaranteed, within limits of the on-board buffering elements in the FPHX chips and the ROC, to arrive at the FEM in the rack room. This architectural choice allows for additional processing, beyond simple data acquisition purposes, to be effected at the FEM. Ideally, given the previously mentioned constraints of an ideal luminosity monitor and the geometry of the

FVTX it would be desirable to count the number of tracks in a collision as this will be directly proportional to the number of collisions. Even better would be to count the number of tracks that point back to a given vertex region. However, that is not possible to implement within the limits of the current FEM FPGA (Figure 5.26) as most of the general purpose elements of the FPGA are currently utilized for data acquisition tasks, though it could be accomplished trivially with a new board dedicated to the task.
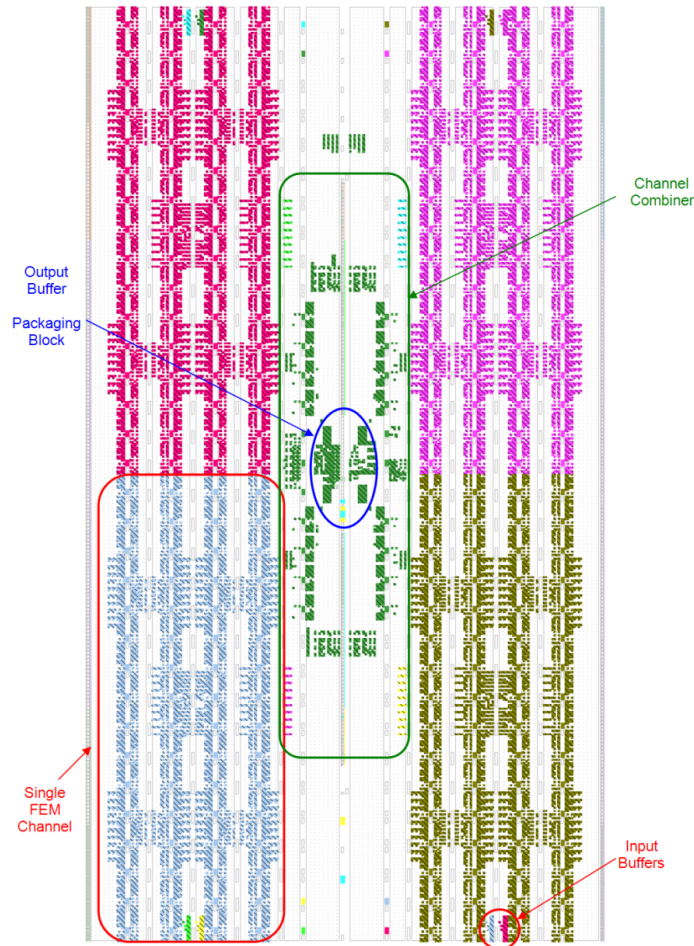
Figure 5.26: Implementation of the FEM FPGA design.

To avoid having to perform the pattern recognition step on the FPGA, a com-

promise is taken by counting the number of hits per crossing. The number of hits is directly proportional to the number of clusters (charge deposited across multiple strips due to a single ionizing particle), which is also directly proportional to the number of tracks and, therefore, the delivered luminosity.

Even the näively simple task of counting the number of hits that arrive at the FEM is complicated by the space restrictions on the FPGA. At the luminosities seen in Run13 the collision rate is approximately 10 MHz and the average number of hits created in a collision is roughly 250 as seen in Figure 6.13. Therefore, during an entire 90 minute run approximately $10^{11} - 10^{12}$ hits above threshold are produced in the FVTX and a binary counter that is at least 32-bits wide is needed to accumulate the counts reliably. Due to the segmentation of the read-out chain there must be a set of 120 counters, one per RHIC crossing, for every FEM channel (two wedges) of which there are four per FEM. Therefore, the design calls for a total of 480 counters that are a minimum of 32-bits wide. The most common implementation of a fast binary counter requires five gates per bit. Using this approach the counter array would occupy over 80% of the Xilinx Virtex-4 FPGA that is used in the FEM.

Fortunately, the FPGA that was chosen for the FEM was selected for the large number of built-in memory elements, block FIFOs, that it contains. However, it also possesses a large array of 512 DSP slices. A DSP48 slice is an 18 bit twos complement multiplier followed by a 48-bit sign-extended adder that is well suited for digital signal processing applications (DSP). Appropriately configured, the DSP48 slice can be operated as a 48-bit wide binary counter and the cascade between the DSP48 slices can effectively convert a column of slices into a wide shift register.

Finally, a data path was established to retrieve the stored counts from the FEM. The FEM Interface Board has an ethernet interface, but was originally configured to only receive single byte status responses from the electronics chain. Therefore, the entire read-out was redesigned to allow for arbitrary length payloads to be sent in
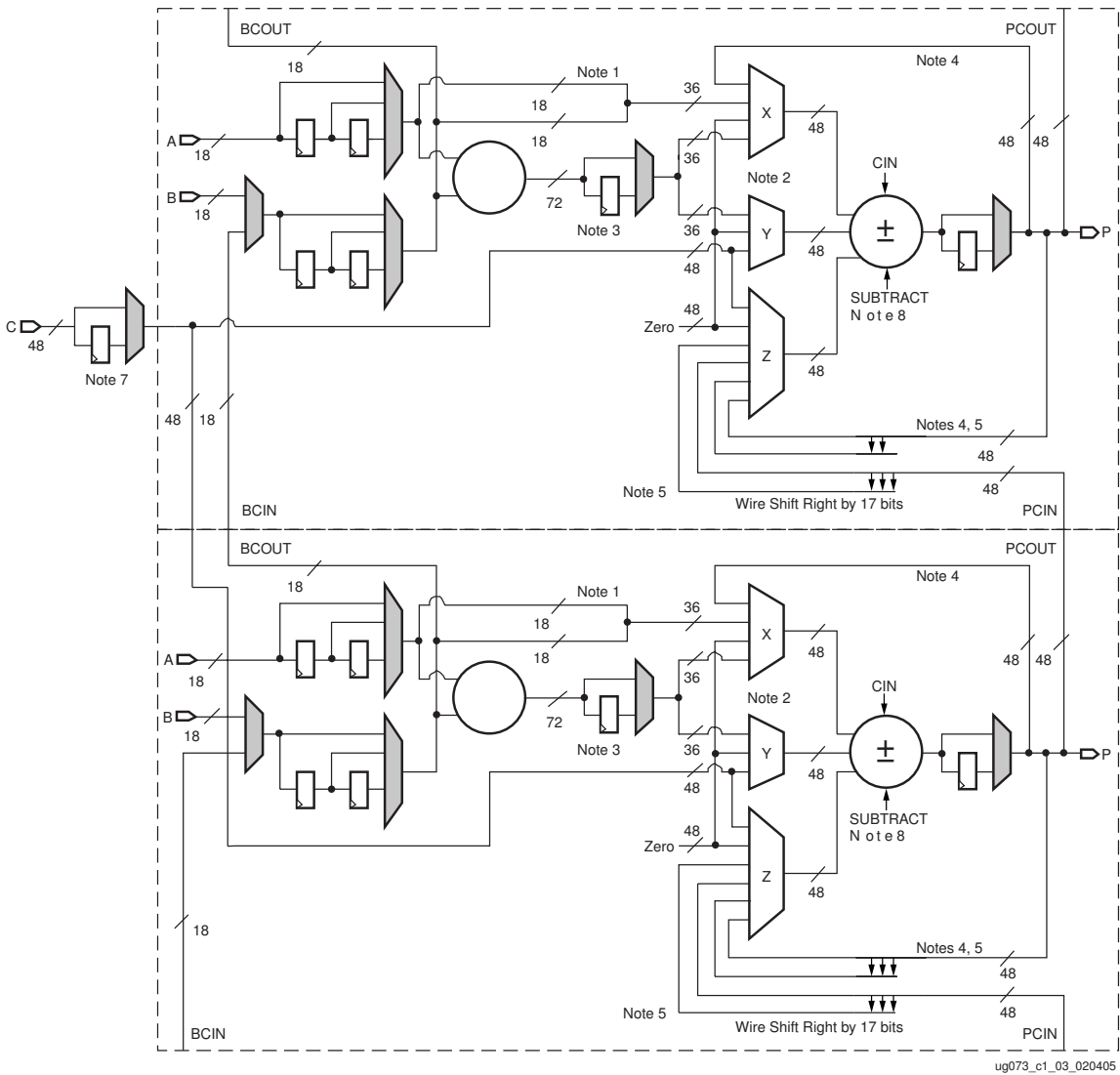
Figure 5.27: The DSP48 slice in the Xilinx Virtex-4 FPGA is able to function as a highly space and power efficient 48-bit wide binary counter. The cascading interconnect also allows for a read-out scheme using minimal general interconnect resources.

response to a slow control command. The completed design is shown in Figure 5.26 where the nearly complete usage of the FPGA can be observed.

The FVTX luminosity monitor scales appropriately in the case of multiple col-

lisions. However, as we are only counting the total number of hits received at the FEM it is not possible to restrict the hits counted to a given vertex range. Therefore, the luminosity, as recorded by the FVTX will only be appropriate for those analyses where the full vertex range can be used. Unfortunately, this is not frequently the case due to the varying acceptances of the PHENIX detector over the full vertex range. A hit counting luminosity monitor is also vulnerable to backgrounds that are not related to the primary collision products such as single beam backgrounds moving with the beam or particles produced by activation of the detector and its support structures. To mitigate this, a second design was completed that, within each crossing, counts the number of wedge pairs in the same azimuthal segment and adjacent stations that both have a hit above a given threshold. The "station-coincidence" design partially sacrifices the nearly linear scaling with multiple collisions as any given wedge pair, of which there are 96, can only increment a single count per crossing whereas the hit counting variety can increment once per crossing for every strip in the detector. However, it also serves to suppress the backgrounds that are not capable of producing hits in adjacent (in z) wedges.

5.3.2.1 Performance

The completed design was integrated into the FVTX front-end electronics for the 2013 RHIC running period as well as a read-out strategy through the slow control ethernet interface that allowed for extraction of the crossing dependent counts. As the best FVTX strategy was not known prior to the beginning of Run13, both the normal hit-counting flavor as well as the "station-coincidence" variety were implemented. To provide symmetric azimuthal coverage for both types, the flavor was alternated from one FEM to the next. Therefore, for every set of 16 wedges pertaining to a single ROC, each half is treated with a different scaling strategy and the results are subsequently analyzed and compared to determine which of the methods

is optimal.
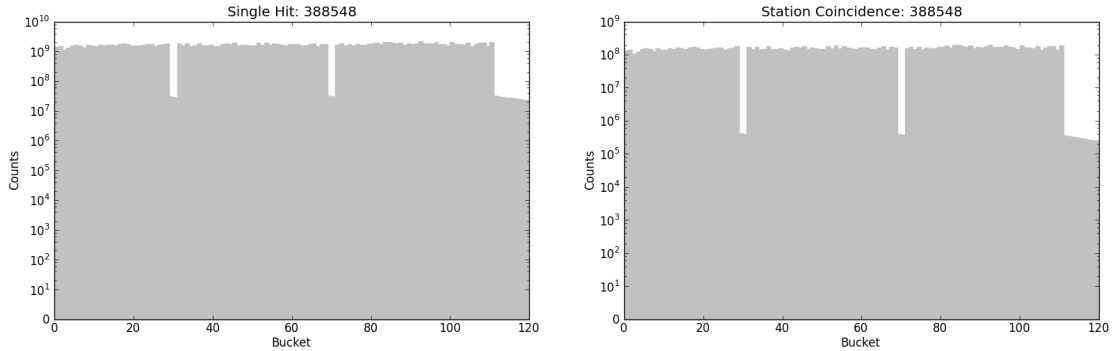
Figure 5.28: Comparison of counts for crossing number from the "singles" and "station-coincidence" flavors.

As can be observed in Figure 5.28, the typical signal-to-background ratio for the "singles" flavor luminosity is approximately 100 : 1 whereas the "station-coincidence" flavor has ratios approaching 1000 : 1. Raw counts are also lowered by approximately one order of magnitude. Statistical uncertainties are beyond what is needed from an analysis standpoint as even the highest statistics A_{LL} measurement will have a statistical uncertainty of 10^{-4} at best. The signal to background ratio belies the hit counting nature of the FVTX luminosity monitoring capabilities as the BBC and ZDC, which rely on a coincidence between detector arms on opposing sides of the interaction point. A full study of the performance of the FVTX as a relative luminosity detector as well as a comparison with the BBC and ZDC can be found in section 6.5.

Aside from the different signal to background ratios the FVTX count dependence on crossing is found to be nominally consistent with that of the BBC and ZDC, confirming that the hit and coincidence counting strategies are, to first order, valid for monitoring the delivered luminosity. The counts are stored on a channel-by-channel basis every 15 minutes during a run to a database where they can be conveniently retrieved for later analysis. The counts were also recorded whenever the run is

terminated. The strategy was adopted to allow for studies of the time dependence of the luminosity. A small number of channels were excluded from certain runs due to apparent anomalies in the read-out that create a non-physical structure within the counts that repeats every 8 crossings. Possible causes are FPHX chips and fibers that lose synchronization with the rest of the read-out chain and return noise that is misinterpreted as data. As this problem affects a very small portion of the total data collected it is simply ignored at the analysis stage with no attempt made, or perhaps possible, to recover the suspicious data.

5.3.3 Trigger

As introduced in subsection 4.2.4, triggering is used to optimize the use of the band-width available to store event data to disk, which is orders of magnitude smaller than the total data throughput capability of the experiment during collisions. In order to provide a trigger the event data from the detector must be quickly processed and a decision made within the maximum buffering capabilities of the PHENIX detector subsystems. The same push architecture of the FPHX chip that enables the ability to perform online luminosity monitoring also enables the use of the FVTX detector as a trigger.

The original FVTX proposal includes a design for a sophisticated trigger (Figure 5.29) that involves splitting the incoming data stream at the input to the FEM to a separate trigger board with a large FPGA dedicated to forming a trigger decision. The design calls for an FPGA logic that quickly processes the incoming hits into tracks with an on-board tracking algorithm based on the Hough transform as is used in the offline tracking software. The fast tracking output would then be used to also perform vertex finding on the FPGA. With both a vertex and the set of on-line tracks, the distance of closes approach (DCA) to the vertex is calculated for all tracks and a trigger decision is made based on the presence of tracks with displaced

vertices. Thus, the proposed FVTX trigger would be able to enhance the fraction of events with tracks having a DCA that is characteristic of a heavy meson decay, such as that from B and D mesons. A preliminary study of the trigger design found that the implementation was feasible and tracking could be completed with a trigger decision emitted within the time available, even in a heavy ion environment where hit occupancy can reach nearly 3%.

While a displaced vertex trigger would certainly be of utmost interest for the primary physics program of the silicon vertex detector upgrades at PHENIX, it would also require substantial design work and dedication of funds to create and fabricate separate trigger boards and implement the design in a large, expensive FPGA. However, as all the hit information arrives at the FEM, just as it would arrive at a potential trigger board, it is available for triggering purposes if the FEM FPGA can be modified to emit a trigger signal. The remainder of this chapter is dedicated to the description of a proof-of-concept FVTX trigger that was designed to be completely contained within the current electronics layout of the detector, with the only necessary modification being the addition of triggering logic to the existing FPGA designs in the FEM and FEM Interface Board. As seen in Figure 5.26, the FEM FPGA is nearly 100% utilized and as such the difficulty to find valid placements and routing of the FPGA components becomes more and more challenging.

Despite these challenges it was found to be possible to create a trigger design that functions at the full native speed of the FEM without interfering with the normal data acquisition and luminosity monitoring functions of the FEM. Since the design is constrained to fit completely within the available area of the FEM FPGA, we must restrict ourselves to the most basic hit information processing. The final design as used in proof-of-concept testing is closely related to the luminosity monitor strategy. To wit, an FVTX multiplicity trigger was created where a programmable multiplicity is used as a trigger primitive for each FEM. Then, a global trigger

Figure 5.29: Proposed design for an FVTX trigger capable of selecting events containing tracks from a displaced vertex

decision is created from the FEM primitives by the FEM Interface Board which interfaces with the PHENIX trigger subsystem: Global Level 1. With all of the pieces in place a PHENIX wide trigger could be configured from the combination of the FVTX trigger with a BBC coincidence trigger to provide a clean set of events with a high multiplicity in the FVTX. A further trigger design was pursued and completed, but not tested in a collision environment, that would allow for trigger decisions to be made from chip combinations within the FVTX. Channel combinations, or what is effectively tracking, is not possible for the aforementioned reasons. However, a rough tracking using programmable chip combinations has been shown to be completely feasible within the constraints of the current electronics.

The multiplicity trigger was tested across multiple FVTX cages (NW, NE, SW, SE) for stable timing and coincidences during the 2013 running period. As the full trigger implementation would require the installation of additional TTL based signal wires between the FEMs and the FEM Interface Board, the testing was restricted to small-scale tests of a single FEM in two cages. It was found that the rate at which the FVTX trigger prototype fired was roughly equal to the expected event rate. It was also found that the triggers from separate FEMs in separate cages fire in coincidence, supporting the timing stability and giving preliminary confirmation to the feasibility of creating a functional trigger using existing hardware that has already been designed, purchased, and installed at PHENIX. Future simulations must be done to fully explore the possible uses of the trigger to extract useful and interesting physics events, however, one such use is the study of high multiplicity events in pp and pA collisions to compare the multiplicity dependence of particle production with standard heavy ion data from AuAu.

Chapter 6

J/ψ Longitudinal Double Spin Asymmetry

6.1 Motivation

6.1.1 J/ψ Meson

To cleanly access the gluon polarization one needs a probe that is produced through a channel that is sensitive to gluons. At the energies accessed by RHIC the J/ψ is produced through both $q\bar{q}$ annihilation and gg fusion. At $\sqrt{s} = 510\,\mathrm{GeV}$, gg fusion is dominant at more than 99% of J/ψ production for unpolarized pp collisions and more than 99.9% for the polarized case as can be seen in Figure 6.1 at central rapidities.

Therefore, the factorized J/ψ cross section can be expressed as a convolution of various quantities as in Equation 6.1.

$$\sigma(pp \to J/\psi X) = g(x_1)g(x_2) \otimes \hat{\sigma}^{gg \to c\bar{c}}(\hat{s}) \otimes \mathcal{D}_{c\bar{c}}^{J/\psi} + \ldots \tag{6.1}$$
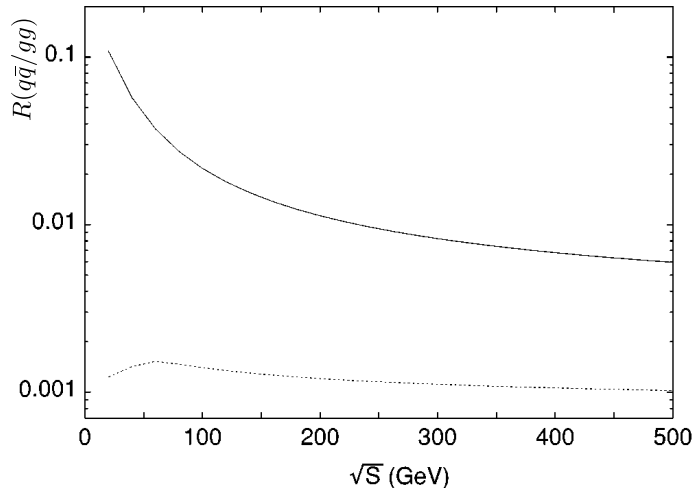
Figure 6.1: Ratios of unpolarized (solid) and polarized (dashed) $q\bar{q}$ and gg process luminosities as a function of c.m. energy, $\sqrt{s}$, at $y = 0$ [46].

where $g(x_i)$ is the unpolarized gluon PDF for gluons carrying a fraction x_i of the proton momentum, $\hat{\sigma}^{gg \to c\bar{c}}(\hat{s})$ is the partonic process cross section for the production of a $c\bar{c}$ pair from gluon fusion, and $\mathcal{D}_{c\bar{c}}^{J/\psi}$ is the probability to form a J/ψ bound state from the $c\bar{c}$ pair which depends on the production mechanism.

The double longitudinal asymmetry in $J\psi$ production, then, is sensitive to the gluon polarization at first order

$$A_{LL} = \frac{\Delta\sigma}{\sigma} \sim \frac{\Delta g(x_1)}{g(x_1)} \frac{\Delta g(x_2)}{g(x_2)} \otimes \hat{a}_{LL}^{gg \to c\bar{c}}(\hat{s}) \tag{6.2}$$

where $\Delta g(x_i)$ is the polarized gluon PDF and $\hat{a}_{LL}^{gg \to c\bar{c}}(\hat{s})$ is the asymmetry in the partonic level cross section, which is calculable in pQCD.

The ranges of x probed in pp collisions is determined by the process, the center of mass energy and the event kinematics involved. When moving to forward rapidity, such as the PHENIX muon arms, we move to a lower x range than has been previously probed, however, it must be noted that asymmetries are also expected to become smaller as we move to smaller x. A potential disadvantage of the gg channel is

that instead of probing $\Delta g(x)$ itself, as would be desired, the A_{LL} is sensitive to the product of $\Delta g(x_1)\Delta g(x_2)/g(x_1)g(x_2)$. If x_1 and x_2 have significant overlap then the A_{LL} is essentially reduced to $\Delta g^2(x)/g^2(x)$ which would not give sensitivity to a possible node in the Björken x dependence of the gluon polarization.
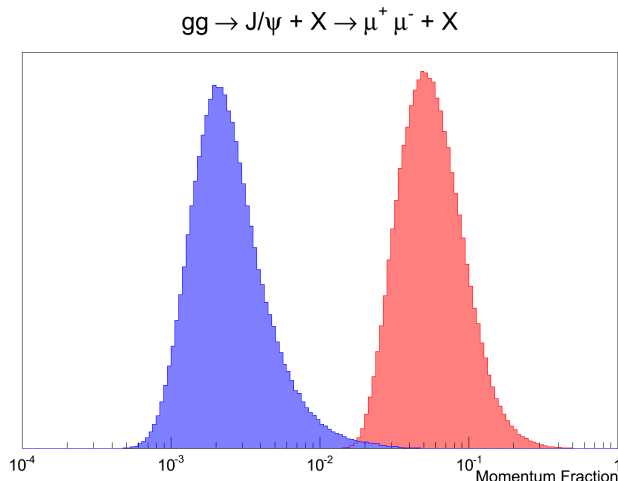
Figure 6.2: Björken x values for the high and low-x gluons participating in the production of J/ψ bound states through gluon fusion and decaying to $\mu^+\mu^-$ pairs in the forward PHENIX muon arm acceptance at $\sqrt{s} = 510$ GeV as simulated in PYTHIA with CTEQ6 PDFs.

Figure 6.2 shows the results of simulated J/ψ production in the conditions as found in Run13 where it can be seen that the low-x gluon has reach down to $\sim 2\times10^{-3}$ and the high-x gluon is clearly separated with minimal overlap. Also fortuitous is the fact that the high-x gluon distribution is centered in the region that has already been constrained by the previous RHIC π^0 and jet A_{LL} measurements. This information can be leveraged to give clean access to the low-x range where no current experimental data is available.

6.1.2 Current Results

The most recent theoretical prediction for the J/ψ A_{LL} is found in [46] and the $\sqrt{s}$ dependence is shown in Figure 6.3, which indicates that the asymmetry is expected to be smaller than 1% for all center of mass energies above 200 GeV. The calculation is, however, done for a different rapidity range than this analysis and using polarized PDFs from the now outdated GRSV global fits.
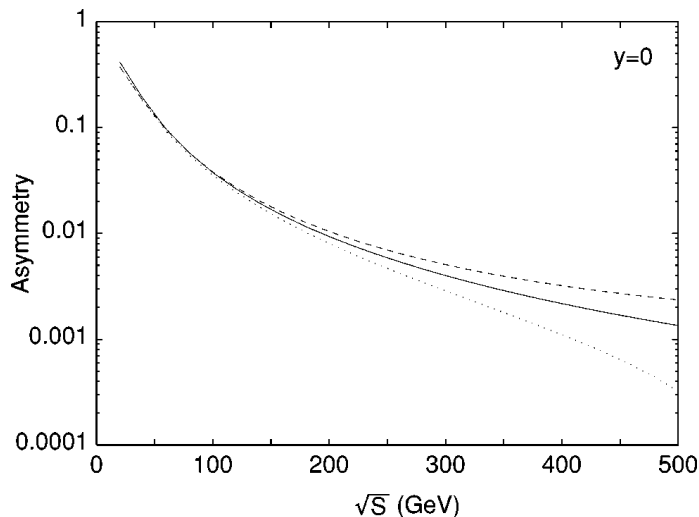
Figure 6.3: Theoretical double polarized asymmetries for gg processes only (solid) and with $q\bar{q}$ processes maximally aligned (dashed) and anti-aligned (dotted) with the gluon contribution at $y = 0$ as a function of $\sqrt{s}$ using GRSV PDFs at LO in NRQCD [46].

The data used in this result comes from the π^0 A_{LL} measurement at central rapidity at PHENIX [47] and the jet A_{LL} measurement at STAR [48] where the asymmetry has been shown to favor a non-zero value and an increasing dependence with transverse momentum. The results of the two measurements are combined in Figure 6.4 where the χ^2 profile for the integral of $\Delta g(x)$ over the probed x range is found to favor a positive, non-zero gluon polarization. Nevertheless, the uncertainty on this result is too large, and the kinematic range probed too limited to make

conclusive statements about the total gluon polarization in the proton.
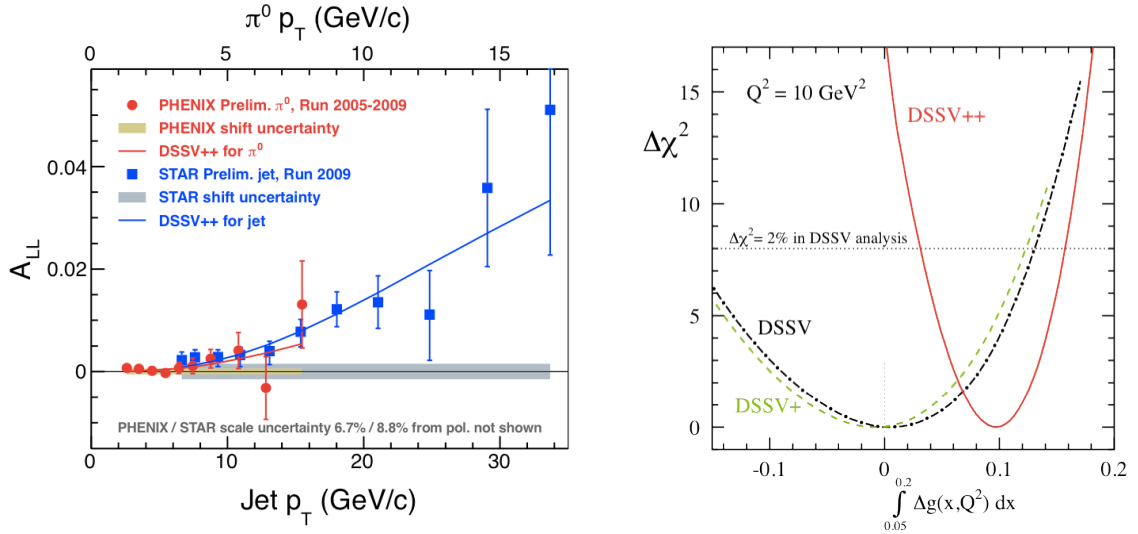
Figure 6.4: Combined results for the π^0 and jet A_{LL} measurement from longitudinally polarized pp collisions at RHIC in 2009.
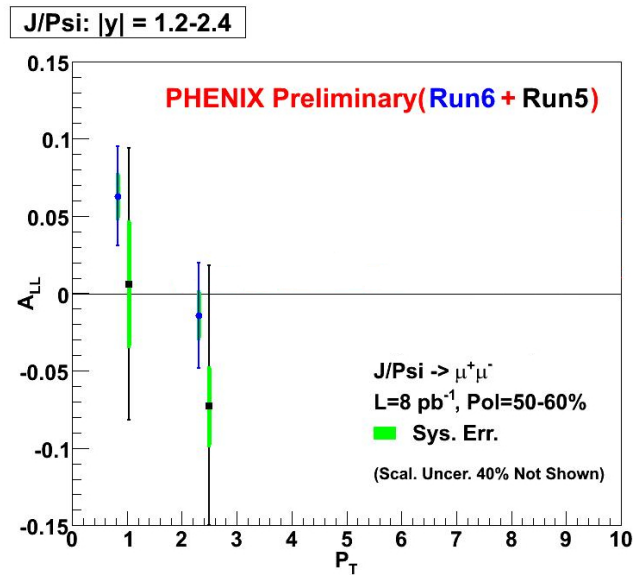
Figure 6.5: Preliminary Run5 and Run6 PHENIX results for the J/ψ A_{LL} in the muon arms at $\sqrt{s} = 200$ GeV.

Currently, the only available results for $J/\psi\ A_{LL}$ are at $\sqrt{s} = 200$ GeV in the PHENIX muon arms from Run5 and Run6 (Figure 6.5). The measurement is clearly statistically limited with respect to the size of the expected asymmetry. In Run13, the sampled luminosity is more than ~ 20 times greater than that of Run5 and Run6 combined and will allow for statistical errors on the order of 1% or better. In addition, the average polarization of both beams was greatly superior. As the figure of merit for a double spin asymmetry goes as P^4 it is of the utmost importance to maintain a high polarization. As can be seen in Figure 6.6 and Figure 6.7, both goals have been achieved and the 2013 data set at RHIC is the ideal data set for gluon polarization studies. Unfortunately, the target integrated figure of merit was not reached due to difficulties in simultaneously maintaining high polarization and luminosity during the run. Nonetheless, a large percentage of the goal was achieved.
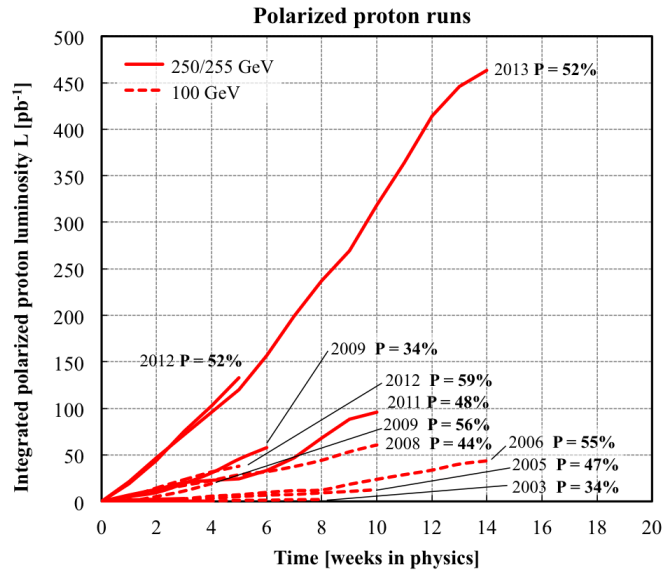
Figure 6.6: Comparison of the polarization and total integrated luminosity achieved for the polarized pp runs at RHIC.
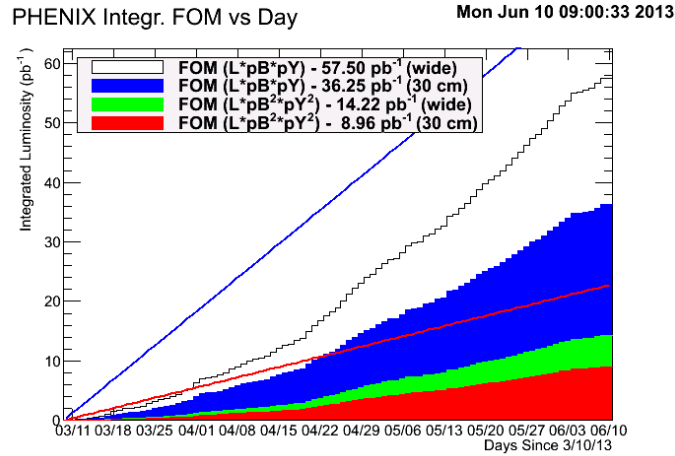
Figure 6.7: Integrated figure of merit metric vs. day for the Run13 running period at RHIC.

6.1.3   Global Fits

The latest fits from the DSSV group [49] that include the RHIC 2009 data from PHENIX and STAR are shown in Figure 6.8. The current fits are nearly uncon-strained below $x = 5 \times 10^{-2}$ where no experimental data currently exists. The J/ψ asymmetry will not have sufficient statistics to meaningfully impact the mean value of the fits, but could potentially impact the uncertainties at low x.

Though this document is not concerned with it, there are also substantial efforts underway to constrain the sea quark contributions and separate the sea quark con-tributions from the valence quark contributions. A complete summary of the all of the polarized PDFs as determined in the latest global analysis, but lacking the 2009 data from the above DSSV++ fit can be seen in Figure 6.9.
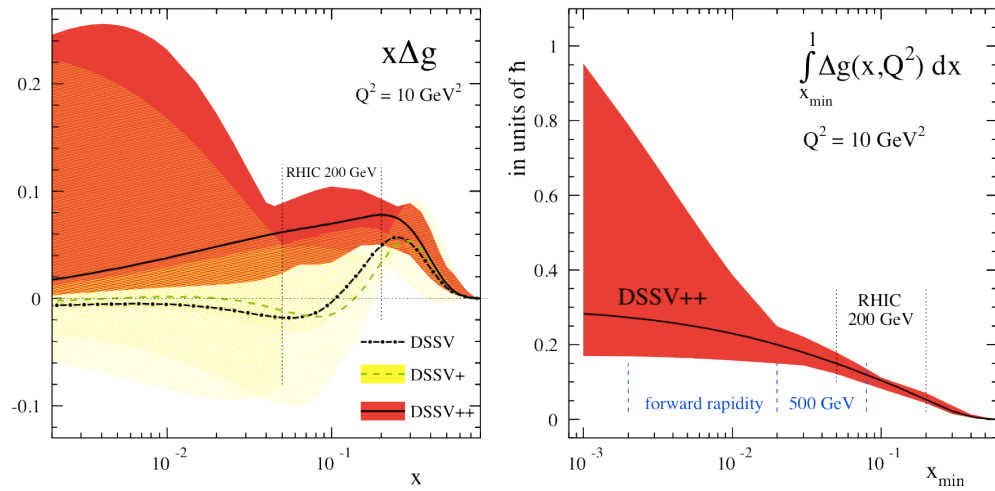
Figure 6.8: Most recent polarized gluon PDF from the DSSV group as extracted in a global fit to all polarized SIDIS, PHENIX π^0 and STAR jet A_{LL} data from Run9.
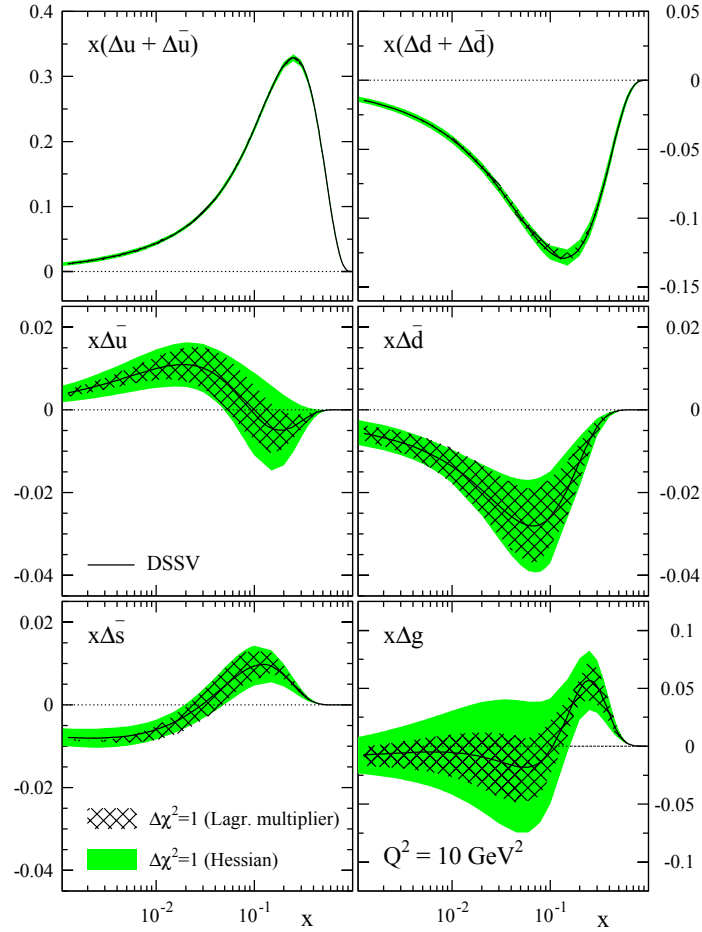
Figure 6.9: Complete set of polarized PDFs as determined in the DSSV global analysis for quark, antiquark, and gluon contributions [49].

6.2 Overview

Specializing Equation 3.11 for the J/ψ we have

$$A_{LL}^{J/\psi} = \frac{\sigma^{++} - \sigma^{+-}}{\sigma^{++} + \sigma^{+-}} = \frac{1}{P_B P_Y} \frac{N_{J/\psi}^{++} - R N_{J/\psi}^{+-}}{N_{J/\psi}^{++} + R N_{J/\psi}^{+-}} \tag{6.3}$$

As is clear from the above formula the main work in the analysis consists of identifying and counting the number of J/ψ particles that were produced and sorting those counts by the helicity of the corresponding collision. Additionally, study of the background fraction that is present in the raw J/ψ sample must be quantified along with the asymmetries of the components of that background. The relative luminosity must be extracted and the systematic uncertainty derived from a residual asymmetry between the BBC and ZDC must be quantified. Putting all of those pieces together we will arrive at the final asymmetry.

As we are studying the dimuon decay channel of the J/ψ we will be using the forward muon arms of PHENIX. The Forward Silicon Vertex Detector (FVTX) upgrade was also present and fully functional for the Run13 period. However, due to geometrical acceptance effects the fraction of dimuons that are reconstructed in the muon arms that also pass through the FVTX detector is approximately 25%. When FVTX information is available for a dimuon pair the mass resolution is greatly improved and the rejection of uncorrelated backgrounds is enhanced, which leads to smaller background fractions. However, as previously discussed, the expectation given the current state of the polarized gluon global fit is an asymmetry of less than 1% and given the rate of J/ψ production we cannot afford to restrict the analysis to FVTX matched dimuons.

The strategy, therefore, is an opportunistic one that uses the entire Run13 dataset and utilizes the additional FVTX information only when it is available. As such, we will be maximizing the use of the data available to us and improving the analysis for the portion of the data where it is possible. To do so, the dimuon sample is separated

into two disjoint subsets that consist of dimuons where both of the muons have good FVTX information (good being quantified by the matching variables between the FVTX and MuTr) and those that do not. The entire analysis is completed for each subset independently and the subset asymmetries are combined to form the final asymmetry.

6.2.1 Outline

Starting from Equation 6.3 the basic structure of the analysis is developed as follows:

- Separate data into subsets with good FVTX dimuon matches and without

- $2(3)\sigma$ mass windows around the J/ψ peak are defined for each subset from fits to all data

- Background fractions are extracted from the subset fits

- The inclusive count of dimuons in the J/ψ mass window is extracted according to:

$$N_{J/\psi}^{raw} = N_{\mu\mu}^{q=0} - N_{\mu\mu}^{q\neq0} \quad | \quad M_{\mu\mu} \in [M_{J/\psi} - 2(3)\sigma, M_{J/\psi} + 2(3)\sigma]$$

  where q is the total charge of the dimuon pair.

- Estimate the like-sign background A_{LL} from like-sign dimuons underneath the J/ψ mass peak

- Estimate the unlike-sign background A_{LL} from unlike-sign dimuons from a $M_{\mu\mu} \in [2.0\ \text{GeV}, 2.5\ \text{GeV}]$ sideband

These individual component asymmetries will then be used to extract the signal asymmetry and background asymmetries as

$$A_{LL}^{J/\psi} = \frac{A_{LL}^{inc} - r A_{LL}^{BG}}{1 - r} \qquad A_{LL}^{BG} = \frac{r_{like} A_{LL}^{like} + (r - r_{like}) A_{LL}^{side}}{r} \tag{6.4}$$

With corresponding error given by standard quadratic error propagation

$$\delta A_{LL} = \frac{1}{1-r}\sqrt{\left(\delta A_{LL}^{inc}\right)^2 + r^2 \left(\delta A_{LL}^{BG}\right)^2 + \left(A_{LL}^{BG}/(1-r)\right)^2 (\delta r)^2} \tag{6.5}$$

The MuTr+FVTX and MuTr subset asymmetries will be combined to form the final asymmetry.

The asymmetry is studied as a function of p_T, and to that effect the datasets are further separated into three p_T bins corresponding to 0-2 GeV, 2-4 GeV and 4-10 GeV. The bins have been chosen to have roughly equal statistics with a slight bias towards the lower two bins.

6.3   Quality Assurance

When performing precision measurements on very large sets of data that have been recorded over an extended period of time it is vital to ensure that the conditions under which the data has been recorded remain stable, or at the very least are well quantified. Many environmental variables that are external to the physics at hand may vary such as the efficiency and acceptance of the detectors as they age, the collisions conditions and the beam quality, as well as simple environmental factors such as atmospheric pressure, humidity, and temperature affecting the physical operating parameters of the detectors. During the data taking period care is taken to monitor the detectors and their output in real-time to guarantee high quality data. However, it is still necessary to quantify the reliability of the data through quality assurance checks prior to realizing the analysis. An overview of the procedures in this analysis for the principal detector subsystems used follows.

6.3.1 Muon Arms

To quantify the stability of the muon arms the individual detector performances are evaluated on a low level. The MuID efficiency is calculated on a tube by tube basis for all runs. Runs with abnormal efficiencies in a substantial portion of the detector are discarded from the analysis. An example of the extracted efficiencies is found in Figure 6.10. The remaining efficiency plots are omitted due to the sheer number of figures involved.
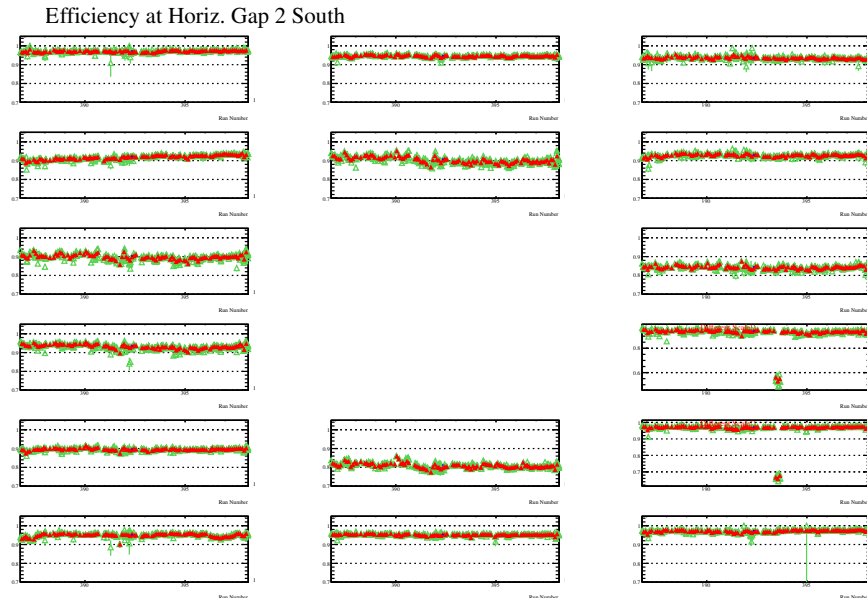
Figure 6.10: Tube efficiencies vs. run for a single gap of the MuID detector.

The MuTr, like many detectors, depends on the delivery of a stable high voltage to collect the charge deposited by the ionizing particle as it passes through the tracking chambers. As a first order QA procedure the status of the high voltage for the MuTr is tracked and runs with an abnormally high number of disabled channels are discarded. The status of the high voltage for the entire Run13 period is found in Figure 6.11. For detector issues that extend beyond the application of high voltage, the number
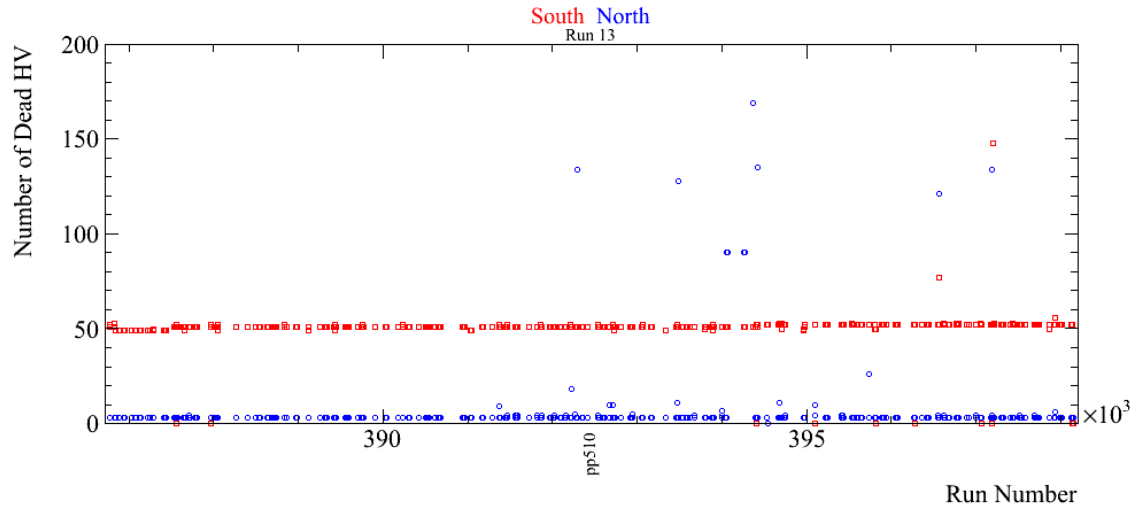
Figure 6.11: High voltage status by number of dead channels in the MuTr arms for the Run13 period.

of reconstructed clusters is observed for run to run stability for individual detector segments as in Figure 6.12. This level of QA eliminates runs where the detector is operating in a reduced capacity either due to physical or electronic anomalies. Regardless of the cause, runs that deviate from the typical behavior are removed from the analysis.
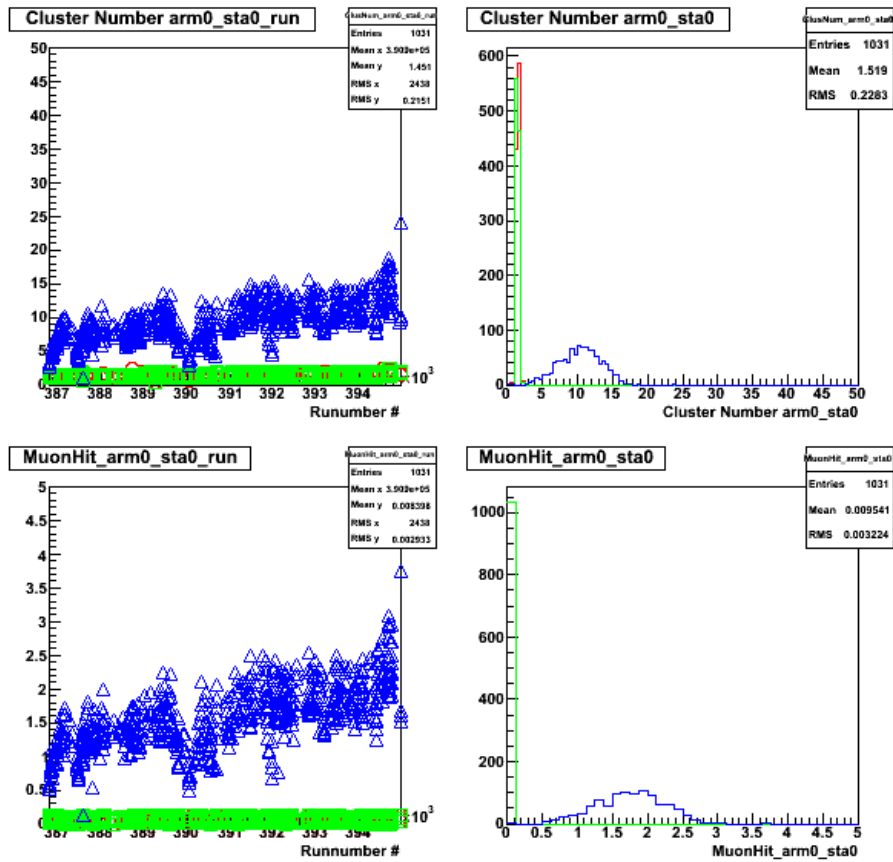
Figure 6.12: Reconstructed MuTr clusters for the Run13 period for a single detector segment in the South muon arm. Red is station 0, green is station 1, and blue is station 2. The left panel shows the run dependence, the right panel shows the frequency distributions.

6.3.2   FVTX

FVTX production output was considered on a variety of different quantities to analyze both the detector performance and stability on a hardware level as well as to verify the reconstruction software chain at various stages.

6.3.2.1 Hits

Beginning with the most basic we have the number of FVTX hits produced normalized by the number of events in each run. As a reminder an FVTX hit is the raw hit information as produced by the FPHX front end chips with timing, ADC value, and spatial location encoded. After normalizing by event count the remaining dependence with run is the event rate/multiple collision rate and detector live area and efficiency.

Hot channels, on the order of 100, were masked in hardware for Run 13 and are assumed to not form a large contribution to the total number of hits produced when there are collisions present. Detector dead area did not change substantially over the run period. The FVTX is a biased silicon detector and depends upon reaching full depletion to suppress detector noise. As such, for runs where the bias was inadvertently left disabled there is a large excess of hits.
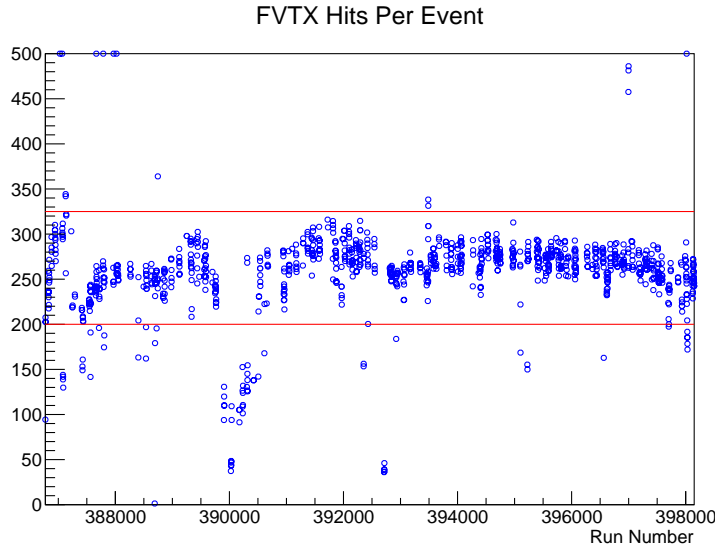
Figure 6.13: Hits produced in the FVTX detector normalized by number of events per run vs. run for Run 13. Accepted range is set to [200, 325].

Figure 6.13 shows the run by run dependence of the event normalized hit counts throughout the entire FVTX detector for Run 13. Immediately obvious is the brief period at the beginning of the running period when the detector was configured with a two beam clock wide readout upon Level 1 trigger request. Upon switching from the two clock wide trigger to the nominal one clock wide trigger used for the remaining of Run 13 the number of hits per event dropped by roughly 40%. Also noticeable is the period starting around run 390000 where the FVTX had a period of hardware instability of undetermined origin. The runs in this period are deemed unusable for most all physics analyses.

A range of [200, 325] hits per event is found to be a nominally acceptable range for determining detector stability as is indicated by the horizontal lines in Figure 6.13.

6.3.2.2   Coordinates

FVTX coordinates are formed during reconstruction by clustering hits from adjacent strips. Maps are used to correctly cluster across dead channels. Online calibrations are used to identify hot channels automatically and store the results to a calibrations database. During reconstruction the hot maps are used to suppress coordinate creation from strips that have been marked as hot. This also serves to stop the reconstruction of events that have been recorded with the bias disabled and are clearly bad as such events are very time consuming to reconstruct and, in any event, will be discarded at the analysis stage.

As can be observed in Figure 6.14 there are a number of runs where the hot channel suppression does not appear to have worked as intended and a number of coordinates has been constructed that is clearly not physical. Largely, the coordinates per event track the behavior of the hits while being substantially cleaner due to the exclusion of known hot channels. The same excess due to the two clock wide trigger
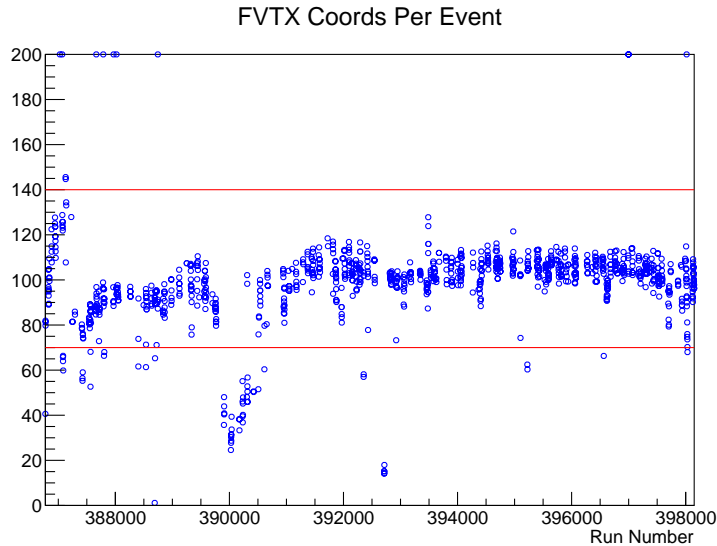
Figure 6.14: Coordinates reconstructed from hits produced in the FVTX detector normalized by number of events per run vs. run for Run 13. Accepted range is set to [70, 140].

can be observed at the beginning of the run as well as the hardware difficulties experienced around run 390000.

The expected number of hits that are clustered to form a coordinate is expected to be roughly three given the 75 μm pitch of the silicon strips. In Figure 6.15 the run dependence of the average coordinate size (in units of strips) is shown. During the two clock wide trigger run at the beginning of Run 13 the average coordinate size is substantially lower than when the one clock wide trigger was used. This is most likely due to the fact that the trigger window for the FVTX is two beam clocks wide, but centered around a single crossing such that some, but not all, hits from the neighboring crossings are read out leaving incomplete coordinates. Interestingly, the average coordinate size is seen to decrease noticeably as the run continued. As there is no dramatic dependence on run within each fill, this is not due to increases in instantaneous luminosity. The most clear dependence is with the total integrated luminosity and may be an indication of a changing detector efficiency for hits that
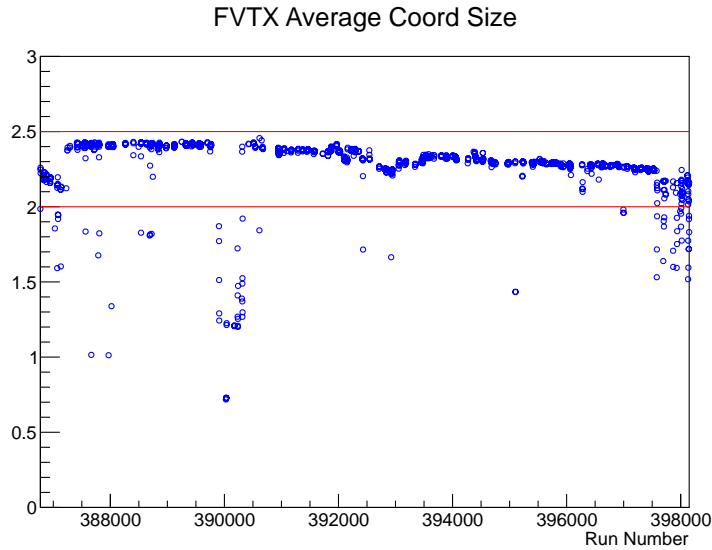
Figure 6.15: Average number of hits that form an FVTX coordinate vs. run for Run 13. Accepted range is set to [2.0, 2.5]. Runs above 397500 are affected by segments with missing QA output.

are close to threshold.

An unusual instability in the average coordinate size is seen around run 398000. Upon investigation the QA histograms were found to be empty for exactly 12 segments each run from run 397580 to run 398149. It is not known why the QA histograms themselves were not filled, but no anomalies were reported during the production of the data set.

A range of [70, 140] coordinates per event and [2.0, 2.5] hits per coordinate is found to be a nominally acceptable range for determining detector stability as is indicated by the horizontal lines in figure 6.13.

6.3.2.3   Tracks

During reconstruction a pattern recognition algorithm is used to group coordinates into tracks. For Run 13 a new algorithm based on the Hough transform was used to augment the geometrical acceptance and multiple vertexing capabilities of the detector.
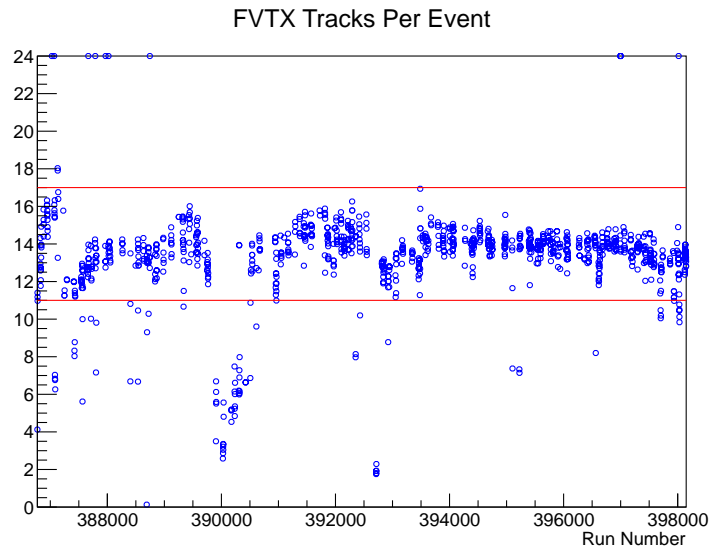
Figure 6.16: Tracks reconstructed from coordinates in FVTX detector normalized by number of events per run vs. run for Run 13. Accepted range is set to [11, 17].

Figure 6.16 shows the run dependence of the number of reconstructed FVTX tracks per event recorded. The behavior tracks that of the coordinates themselves, as expected.

To confirm that track quality was constant, Figure 6.17 shows the average number of FVTX coordinates that were grouped together by the pattern recognition algorithm to form a track. The majority of tracks found are three hit tracks and as such the average number of coordinates trends very close to three. The metric is found to be very stable save for the time period towards the end of the run which,
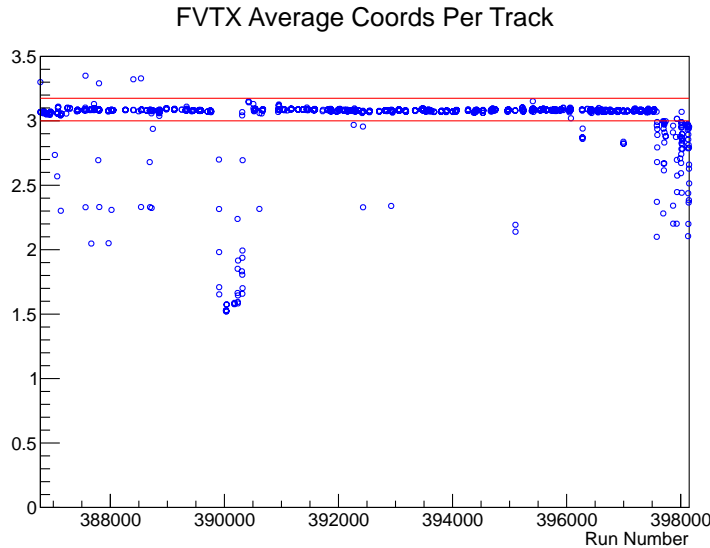
Figure 6.17: Average number of coordinates in reconstructed tracks vs. run for Run 13. Accepted range is set to $[3.0, 3.175]$. Runs above 397500 are affected by segments with missing QA output.

as explained before, is due to the improper filling of the QA histograms.

Figure 6.18 shows the average reduced χ^2 of the coordinate residuals as extracted from the track fitting module during reconstruction. Apart from the shared behavior with all of the observables that were extracted as averages, it is interesting to note that the average value is greater when using the two clock wide trigger. This implies that there are some tracks reconstructed with coordinates that originate in adjacent crossings that have poor residuals. The effect of these spurious tracks should be very small. If matching to the muon tracker is required, the contamination should be practically eliminated.

Nominally accepted values for tracks per event, coordinates per track, and reduced χ^2 are determined to be $[11, 17]$,$[3.0, 3.175]$, and $[3.175, 3.625]$ respectively.
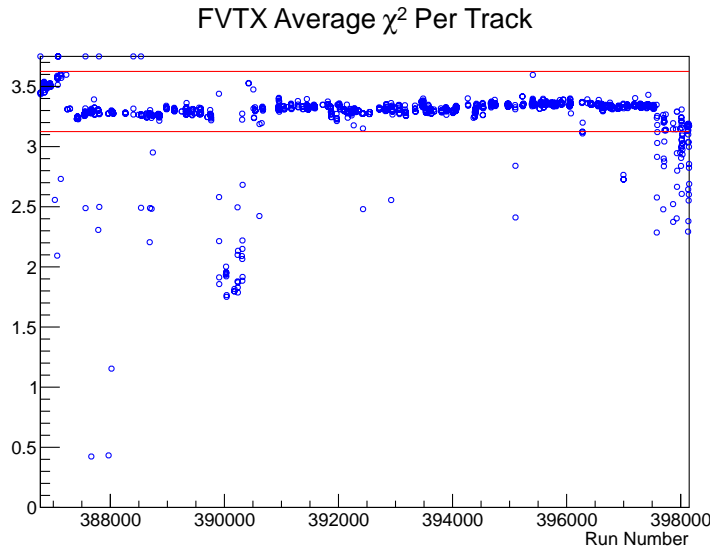
Figure 6.18: Average number of coordinates in reconstructed tracks vs. run for Run 13. Accepted range is set to $[3.0, 3.175]$. Runs above 397500 are affected by segments with missing QA output.

6.3.2.4 Wedges

The largest issue with stability that the FVTX experienced during Run 13 was the loss of individual data fiber synchronization during the run. This has the effect of completely blocking the data stream for an entire wedge. The cause of the synchronization loss was determined to be an excessively fragile check on synchronization status in the FEM FPGA. A single event upset (SEU) could occur on a single bit for a single transmission and cause the FEM to believe, incorrectly, that synchronization was lost. Changes to the FPGA code were effected for Run 14 that has eliminated the problem.

To study this particular issue an analysis of the number of wedges that produced identically zero hits was done on a run by run basis. As the cause of the issue was an SEU, the loss of synchronization could occur at any point during the run. Due
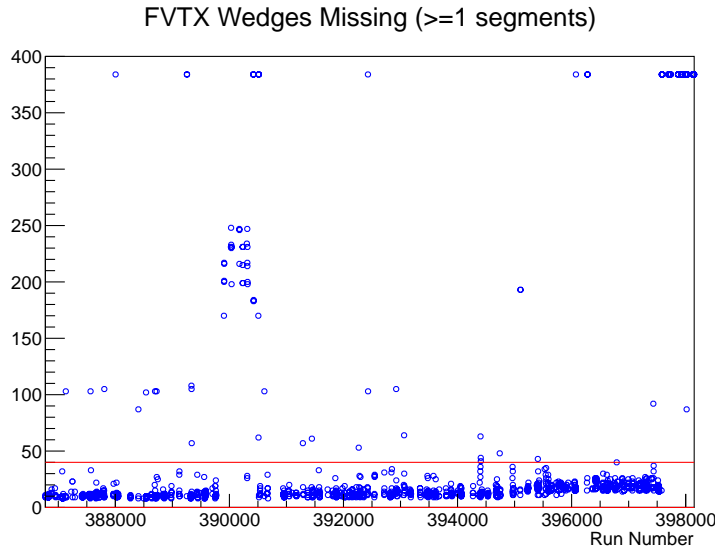
Figure 6.19: Whole wedges that were missing from the readout for at least one segment in a run vs. run for Run 13. Accepted range is set to $[0, 40]$, accepting only runs where 90%+ of the wedges are present for the entire run. Runs above 397500 are affected by segments with missing QA output.

to this, a wedge is counted as "missing" if it produced zero hits for at least one segment during the run. Unfortunately, this is useless for the runs that are affected by improper filling of the QA histograms, and in particular those above 397500.

Figure 6.19 shows that the number of affected wedges is reasonably small in comparison with the total number of wedges. Counts near 100 represent runs when an entire cage (i.e., NE/NW/SE/SW) was missing from the read out. This was occasionally caused during Run 13 when the FVTX start run procedure would fail due to interference from other run control processes. A resource locking strategy was implemented to prevent further occurrences.

A loose cut of approximately 10% of the detector, or 40 wedges, was applied for purposes of determining the good run list.

6.3.2.5   Bad Run Summary

Various run lists have been prepared for different acceptance criteria.

- Strict

    - A run is considered "bad" only if all of the above metrics are out of range.

- Coordinates

    - A run in considered "bad" if the number of FVTX coordinates per event is out of range.

- Majority

    - A run is considered "bad" if the number of FVTX coordinates per event is out of range **or** a majority of the other metrics are out of range.

    - *Note*: For this list the average and missing wedge metrics are ignored above run 397500 due to the improper filling of the QA histograms.

The number of bad runs and the percentage of total runs is shown here for the three criteria.

Type	N_{bad}	$\%_{\mathrm{bad}}$
Strict	45	4.32
Coordinates	86	8.26
Majority	98	9.41

Table 6.1: Summary of the number of bad runs and percentage of total runs during Run 13 for each of the three different good run criteria explained above.

6.4   Background Fraction

The J/ψ measurement has the advantage of being a resonance and therefore a mass peak is available that ensures that the signal to background ratio will be well understood. Nonetheless, it is important to extract the background fraction with the highest possible precision. To that end an extensive study of signal shapes and functional forms, simulated background shapes, fitting techniques and their potential biases has been explored.

6.4.1   Signal Shapes

From a physical standpoint, a Crystal Ball function is a well justified functional form for fitting the mass peaks of the J/ψ and ψ'. The Crystal Ball function is a gaussian which has been joined smoothly, at $x = -\alpha$, with a power law such that it, and the first and second derivative, are continuous functions as defined in Equation 6.6.

$$f(x; \alpha, n, \bar{x}, \sigma) = N \cdot \begin{cases} \exp(-\frac{(x-\bar{x})^2}{2\sigma^2}), & \text{for } \frac{x-\bar{x}}{\sigma} > -\alpha \\ A \cdot (B - \frac{x-\bar{x}}{\sigma})^{-n}, & \text{for } \frac{x-\bar{x}}{\sigma} \leqslant -\alpha \end{cases}$$

$$A = \left(\frac{n}{|\alpha|}\right)^n \cdot \exp\left(-\frac{|\alpha|^2}{2}\right), \quad B = \frac{n}{|\alpha|} - |\alpha| \tag{6.6}$$

The long tail to the left is typically used to describe radiative losses, or in the case of the PHENIX muon arm, the improper correction for the energy loss in the absorber. To study the suitability of this functional form for fitting the reconstructed mass peaks, simulated J/ψ particles produced in PYTHIA6 with NRQCD processes (color octet-model) [50] decaying to $\mu^+\mu^-$ pairs in the muon arm were fully reconstructed in GEANT3 as shown in Figure 6.20
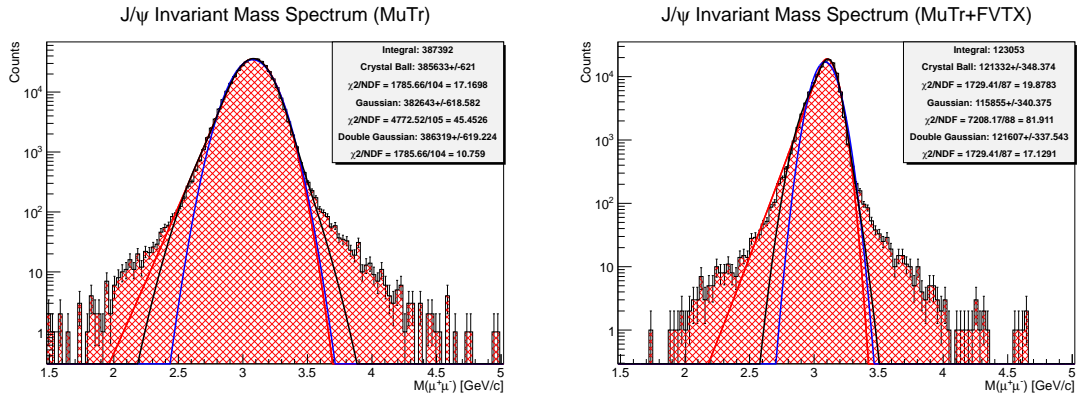
Figure 6.20: Reconstructed mass spectrum for simulated J/ψ particles in the PHENIX muon arms with FVTX matched tracks (right) and without (left). Single Gaussian (blue), Crystal Ball (Red), and Double Gaussian (Black) fits are shown.

The reconstruction was done with the same software as the Run13 production and the same cuts applied as were applied in the main analysis. The most immediate observation to be made from comparing simulation to data is that the mass resolution of the simulated J/ψ particles is approximately 130 GeV for the MuTr alone and 90 GeV for the FVTX whereas the resolutions in real data are approximately 190-200 GeV and 130 GeV. Clearly, there is a deficiency in the real detector that is not well represented in the current simulations and an attempt is made to smear the reconstructed muon tracks to match the real mass resolution of the detector.

The single gaussian fit (blue) is clearly not suitable for use as the signal functional form as it is incapable of describing the long tails that exist in the reconstructed shape on both the low and high-mass sides. The Crystal Ball function (red) does a much better job of describing the low-mass tail of the mass peak, but is still not able to fit the long high-mass tail that is clearly a feature of the reconstruction. It should be noted that the low-mass tail is much heavier than the high-mass tail, but the high-mass tail is of the same order of magnitude as the ψ' in the mass range of the ψ' and must be take into account for any precision measurement. Accordingly, the

Double Gaussian (black) fit gives the best results for the simulated shape as it is able to account for both tails as the mean of the two gaussian is allowed to differ according to Equation 6.7. When using the Double Gaussian functional form the mean value of the J/ψ peak is given as the weighted average of the means of the two gaussian components.
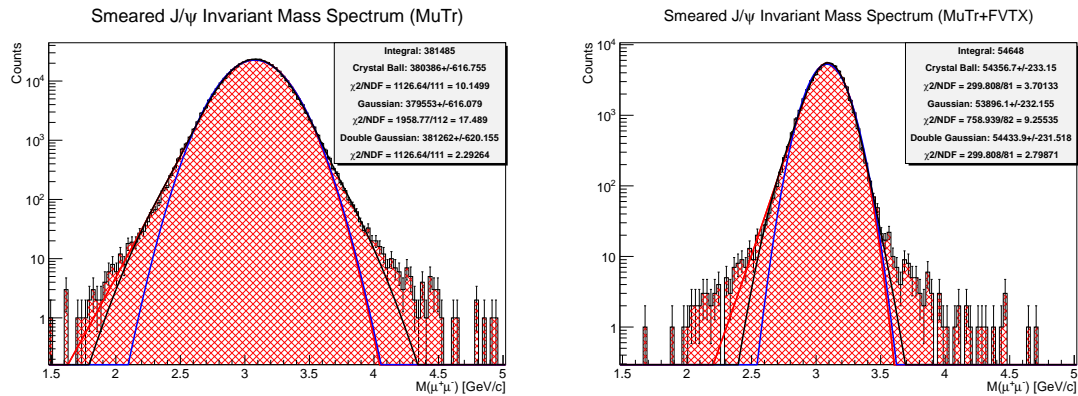
Figure 6.21: Reconstructed mass spectrum for simulated J/ψ particles in the PHENIX muon arms with FVTX matched tracks (right) and without (left) where the components of the single muon momenta have been randomly smeared by $5-7\%$ as a function of the total momentum. Single Gaussian (blue), Crystal Ball (Red), and Double Gaussian (Black) fits are shown.

$$f(x; A_1, \mu_1, \sigma_1, A_2, \mu_2, \sigma_2) = A_1 \exp\left(-\frac{(x-\mu_1)^2}{2\sigma_1^2}\right) + A_2 \exp\left(-\frac{(x-\mu_2)^2}{2\sigma_2^2}\right) \quad (6.7)$$

The same observations and conclusion are equally applicable when FVTX information is available, implying that the long tails present are in fact due to deficiencies in the reconstructed muon momenta as adding more precise vertex information and opening angle does not reduce the relative fraction in the tails. Following this line of thought, and in an attempt to evaluate the signal fits in similar conditions to real data, another simulation was completed on the same PYTHIA/PISA processed events and in the reconstruction step the components of the single muon momenta

were smeared by a momentum dependent amount (linear in total momentum) of $5-7\%$ that was empirically derived to match the p_T dependence of the mass resolution that is seen in real data. The results of this study are shown in Figure 6.21. In summary, the conclusions remain the same as before: the single gaussian is clearly ruled out, the Crystal Ball function is only able to well represent the left hand tail and the Double Gaussian gives the best fit. Again, the conclusion for the FVTX matched data is identical.

It is known that the acceptance-efficiency correction for the dimuon spectrum varies strongly over the mass range spanned by the reconstructed J/ψ peak. The hypothesis that the Crystal Ball function is only a valid functional form for the *true* mass spectrum and the modulation due to acceptance-efficiency effects causes the Crystal Ball function to fail to well represent the peak was explored in Figure 6.22
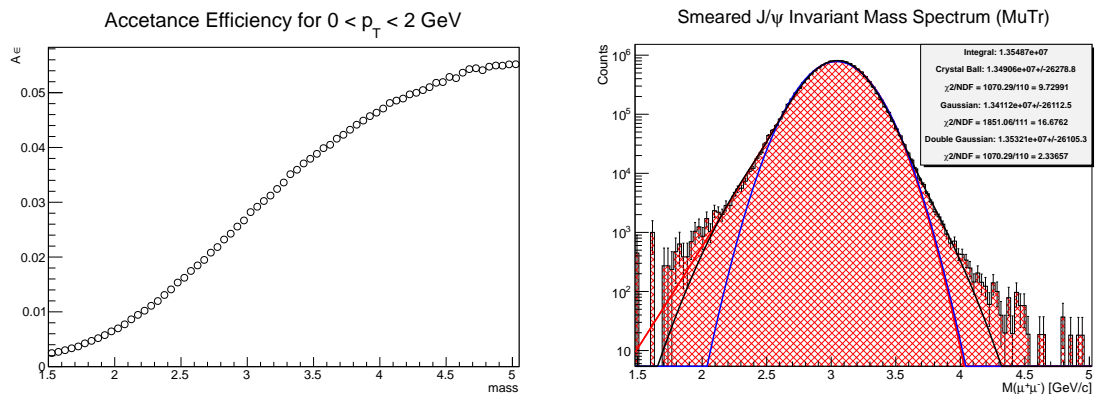
Figure 6.22: Left: The acceptance efficiency $(A\varepsilon)$ as extracted for dimuons in the J/ψ mass range and $p_T \in [0, 2[$ GeV. Right: Reconstructed J/ψ mass spectrum with single muon momentum smearing applied and with acceptance efficiency correction applied and corresponding fits.

The acceptance-efficiency correction was extracted from a dimuon simulation with physical p_T and mass input spectra. The acceptance modulation over the 2-4 GeV mass range can be seen to vary by nearly a factor of 9. However, once the correction

is applied to the above spectra (both with and without smearing) the suitability of the Crystal Ball function is not improved with respect to the Double Gaussian fit. This is true for the FVTX matched simulation as well as the simulation without smearing. As such, the only figure shown here is for the case of MuTr with smearing and the remaining cases are omitted for brevity.

For all further fits with functional forms, the Double Gaussian has been selected and the remaining functional forms have been discarded as unable to properly account for the features observed in the full reconstruction of simulated J/ψ decays.

6.4.2   Background Fits

Two independent methods are used to fit the backgrounds present in the mass spectrum. The first uses a technique known as Gaussian Process Regression (GPR) as detailed in [51] to fit the background shapes without supposing, a priori, a functional form. This has been chosen to supersede the prior methods of extracting the background by using third (and higher) order polynomials that have no strong physical justification. The second is a simulation driven fit that uses simulated shapes for the correlated backgrounds from $b\bar{b}$, $c\bar{c}$, and Drell-Yan processes as well as a shape for the uncorrelated backgrounds as extracted from the like-sign dimuon distribution in real data. Given the results from the previous section a double gaussian functional form is used for the J/ψ peak. A single gaussian is used for the ψ' peak as the statistics are too poor for the double gaussian shape to become apparent. The mean and width of the ψ' is extracted in the fit, however, in some cases where the statistics become too poor the ψ' has a tendency to collapse onto the J/ψ. That is, the mass difference of the J/ψ and ψ' from the Particle Data Group (PDG) is enforced only in the cases where the ψ' fit becomes unstable.

6.4.2.1   Gaussian Process Regression

The GPR method is trained on the data points in the 1.5-2.2 GeV and 4.3-6.0 GeV mass ranges in order to exclude the J/ψ and ψ' contributions to the mass spectrum and include only the data points that should correspond to background for the analysis. The method is then used to extract predictions for each of the mass bins used in the real data spectrum. The GPR method supplies the uncertainty on the predictions as well as exposing the full covariance matrix for all of the predictions. The resulting predictions and uncertainties are highly correlated from point to point and as such it is important to account for the correlations when applying them to a fit. If this is not done, the χ^2 of the fit will be underestimated, and as a result the uncertainties of the fit parameters will also be underestimated.

The GPR prediction points are subtracted from the data spectrum, yielding a spectrum that, ideally, corresponds purely to J/ψ and ψ' counts. This spectrum is fitted with the Double Gaussian (J/ψ) plus gaussian (ψ') form previously discussed. To account for the correlated errors from the GPR method the fit is done by minimizing with respect to a modified χ^2 function that is a generalization of the ideal χ^2 formula to the case of a non-diagonal covariance matrix as defined in Equation 6.8

$$\chi^2 = \sum_{k=0}^{N} \sum_{k'=0}^{N} (F_k - D_k)[C^{-1}]_{kk'}(F_{k'} - D_{k'}) \tag{6.8}$$

where F_k is the value of the fit function at point k, D_k is the value of the data point at point k, and $[C^{-1}]_{kk'}$ is the corresponding matrix element of the inverted covariance matrix for points k and k'. As a note on practicality, this modified least squared algorithm is $\mathcal{O}(N^2)$ where N is the number of data points whereas without correlated errors it is $\mathcal{O}(N)$. Accordingly, the convergence for the modified fitting is very slow. To overcome this, the spectrum is first fit with the normal χ^2 minimization routine. The resulting parameters are used as initial conditions for the modified least squared fitting routine, thereby greatly speeding up the convergence by starting close to the

actual minimum. The resulting fits are shown in Figure 6.23 through Figure B.6.
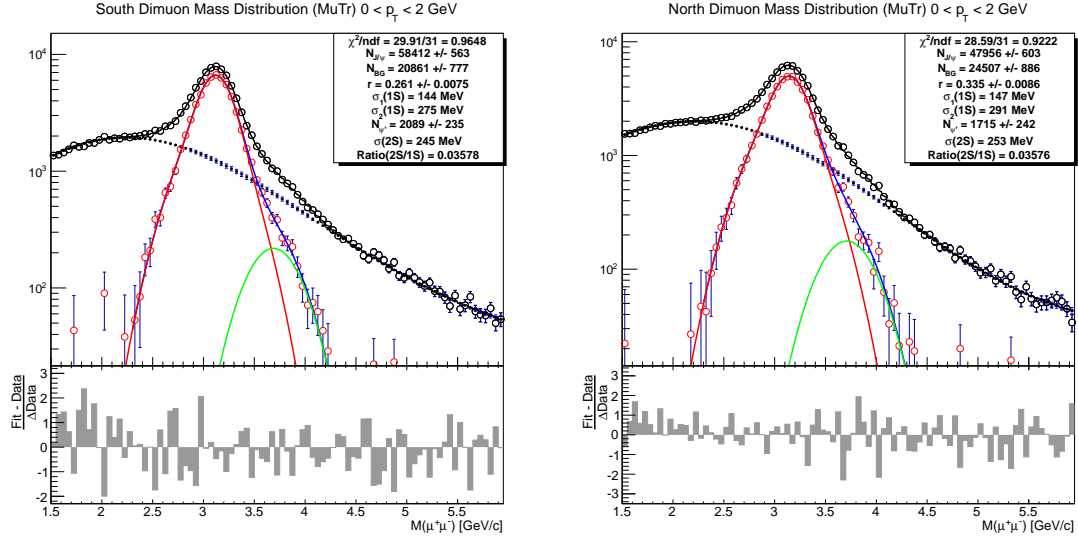
Figure 6.23: MuTr mass spectrum fits with GPR background estimation for the 0-2 GeV bin for the north and south arms and the 2σ mass window.
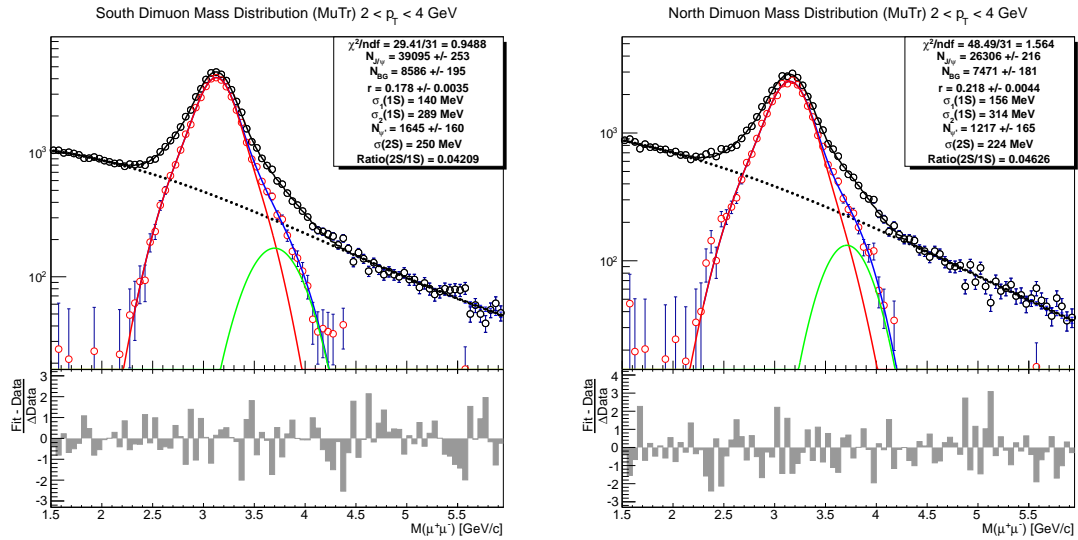
Figure 6.24: MuTr mass spectrum fits with GPR background estimation for the 2-4 GeV bin for the north and south arms and the 2σ mass window.
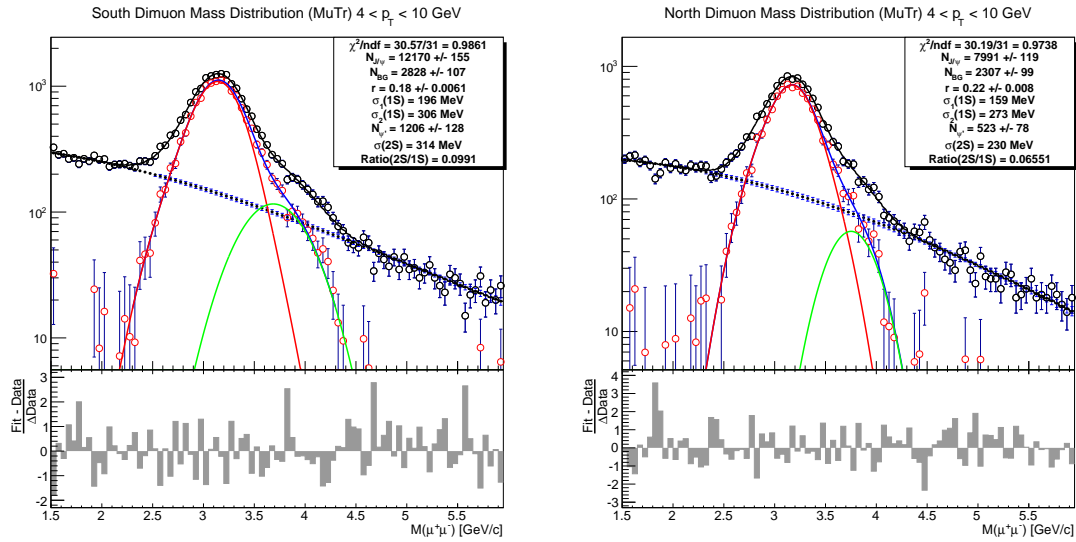
Figure 6.25: MuTr mass spectrum fits with GPR background estimation for the 4-10 GeV bin for the north and south arms and the 2σ mass window.
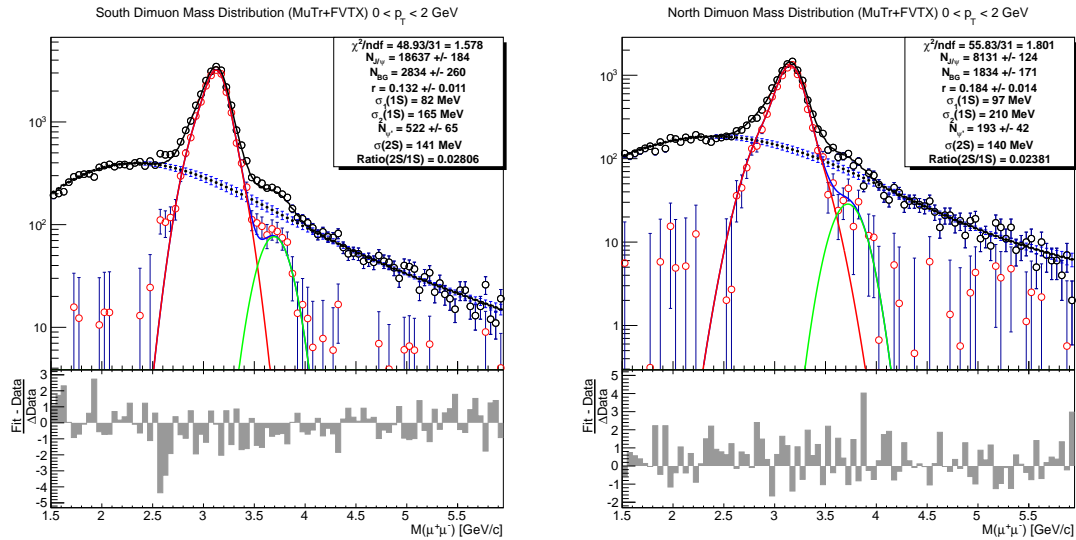
Figure 6.26: MuTr+FVTX mass spectrum fits with GPR background estimation for the 0-2 GeV bin for the north and south arms and the 2σ mass window.
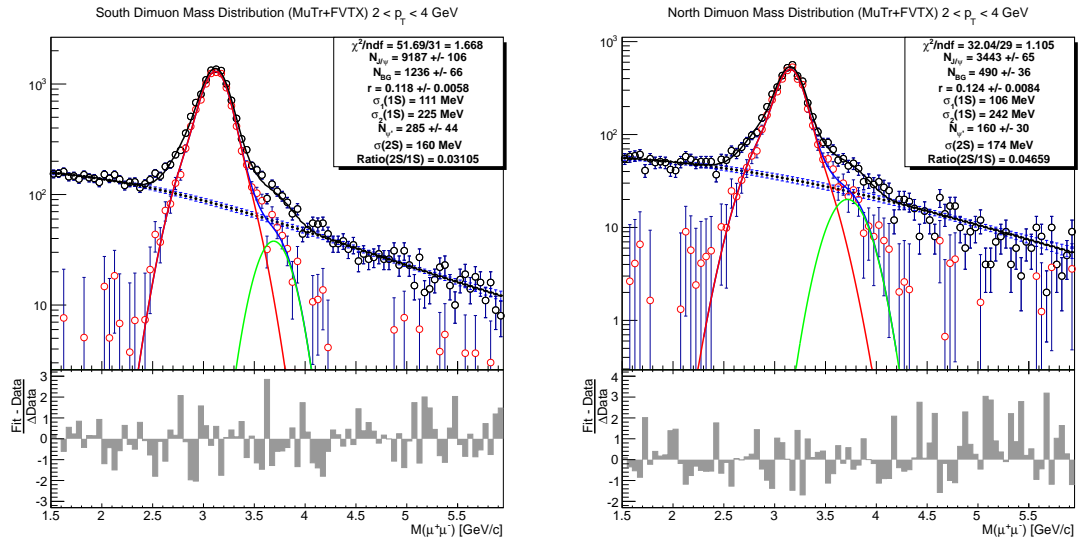
Figure 6.27: MuTr+FVTX mass spectrum fits with GPR background estimation for the 2-4 GeV bin for the north and south arms and the 2σ mass window.
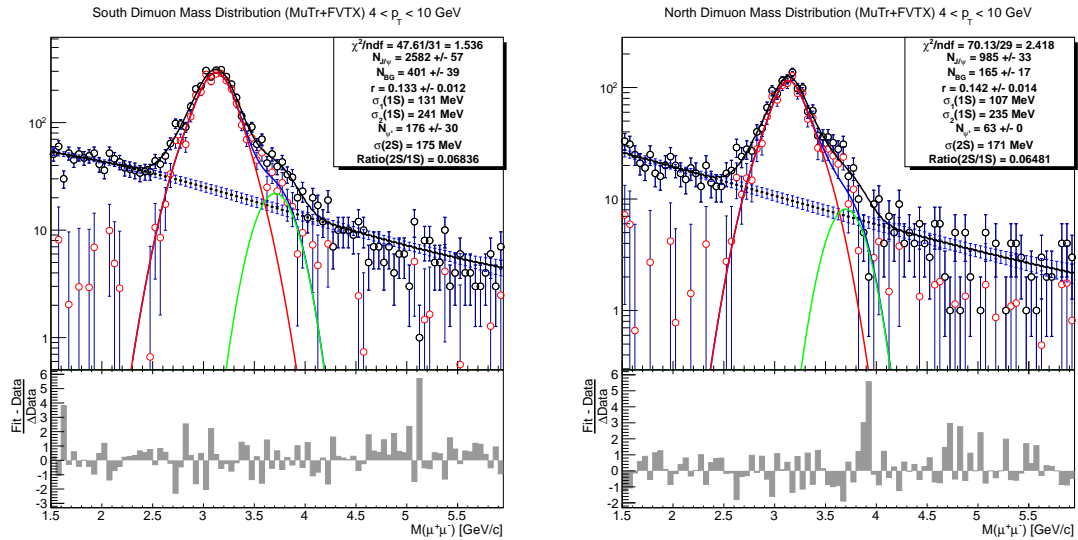
Figure 6.28: MuTr+FVTX mass spectrum fits with GPR background estimation for the 4-10 GeV bin for the north and south arms and the 2σ mass window.

For clarity, the remaining background fits for the case of a 3σ mass window for both the MuTr and MuTr+FVTX cases can be found in Appendix B.

6.4.2.2 Simulated Backgrounds

For the simulated background fits the correlated dimuon background from $b\bar{b}$, $c\bar{c}$, and Drell-Yan processes were simulated and reconstructed through the same reconstruction software as used for the Run13 production. The like sign dimuon mass spectrum shape was used for the uncorrelated background shape. Two different methods were explored with simulated data: with and without the use of a functional form for the signal extraction. The simulated spectrum shapes were fit to the data spectrum with scale factors for each of the components. The uncorrelated shape is extracted from the like sign spectrum and normalized by the geometric mean of the $++$ and $--$ (charge combinations) counts to account for the residual correlation.

The full simulation method, where the simulated shape of the J/ψ peak was fitted with an additional parameter that controlled the smearing of the mass distribution, is unable to properly describe the spectrum in the J/ψ mass range and is rejected. The fits and corresponding pull distributions for the south muon arm are shown in Figure 6.29. From the results it is not clear that there is anything to gain by pursuing fits with simulated mass peaks due to systematic effects introduced by using naïve smearing to match the mass resolution of real data.

Therefore, for this analysis the simulated spectra are used for only the correlated backgrounds and the same functional form as used for the GPR fits is used again for the simulated fits. The results are shown in Figure 6.30 through Figure C.6. The fits are reasonable, and have an acceptable reduced χ^2, however the χ^2 values are systematically higher than with the GPR fits. As the simulation has been found to be clearly deficient for the J/ψ itself, the simulated background shapes may also be
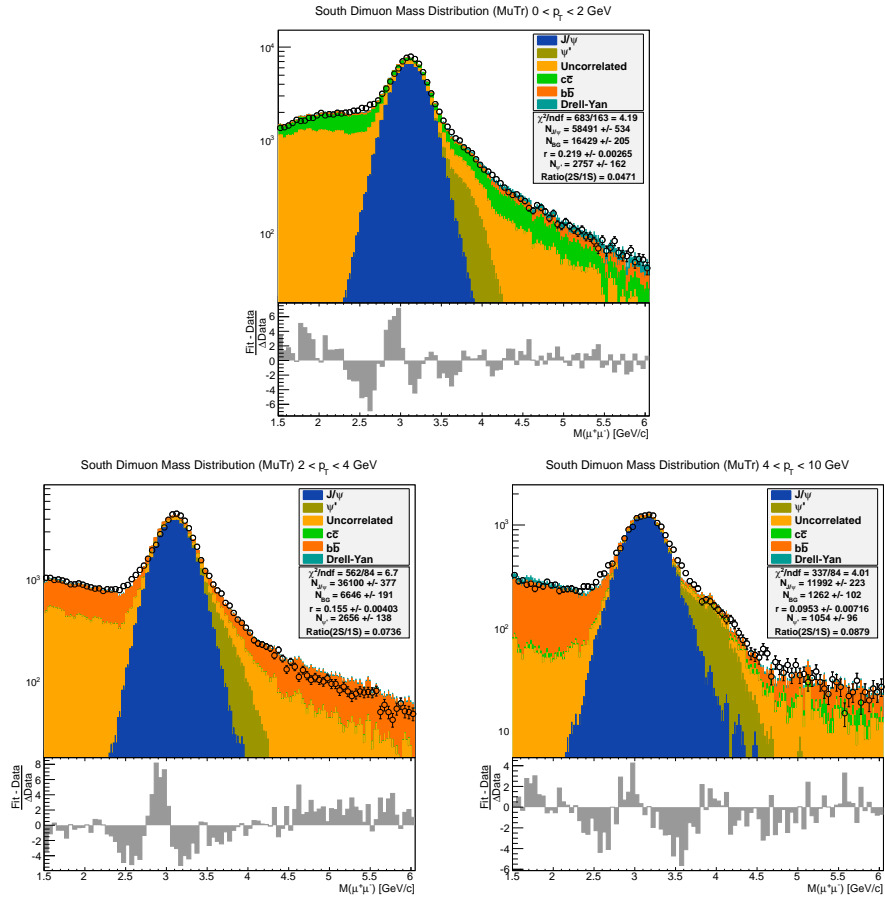
Figure 6.29: Full simulation fits for the south MuTr arm. All components shapes in the fits, including signal, are extracted from simulated data. The fit is unacceptable and has large discrepancies in the *J/ψ* mass range.

affected by the same effects, albeit less noticeably due to the broad shapes of the backgrounds.

Again, for clarity the simulated remaining background fits for the case of a 3σ mass window for both the MuTr and MuTr+FVTX cases can be found in Appendix C.
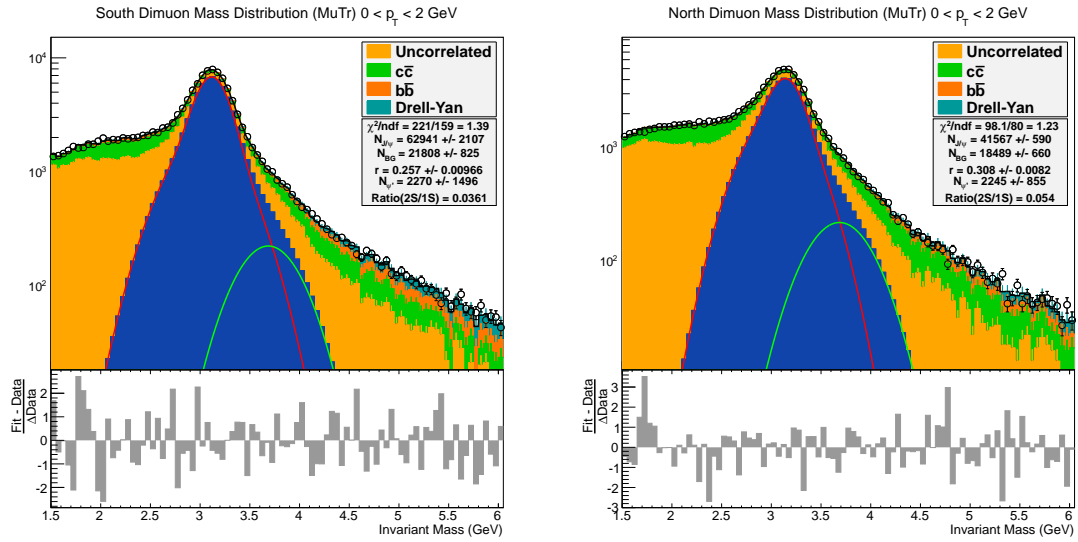
Figure 6.30: MuTr mass spectrum fits with simulated background estimation for the 0-2 GeV bin for the north and south arms and the 2σ mass window.
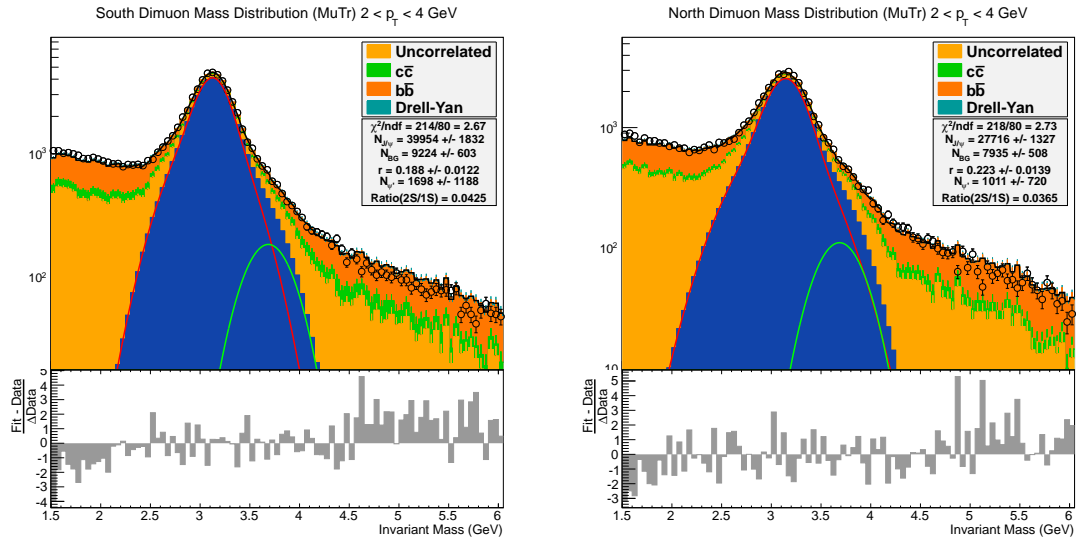
Figure 6.31: MuTr mass spectrum fits with simulated background estimation for the 2-4 GeV bin for the north and south arms and the 2σ mass window.
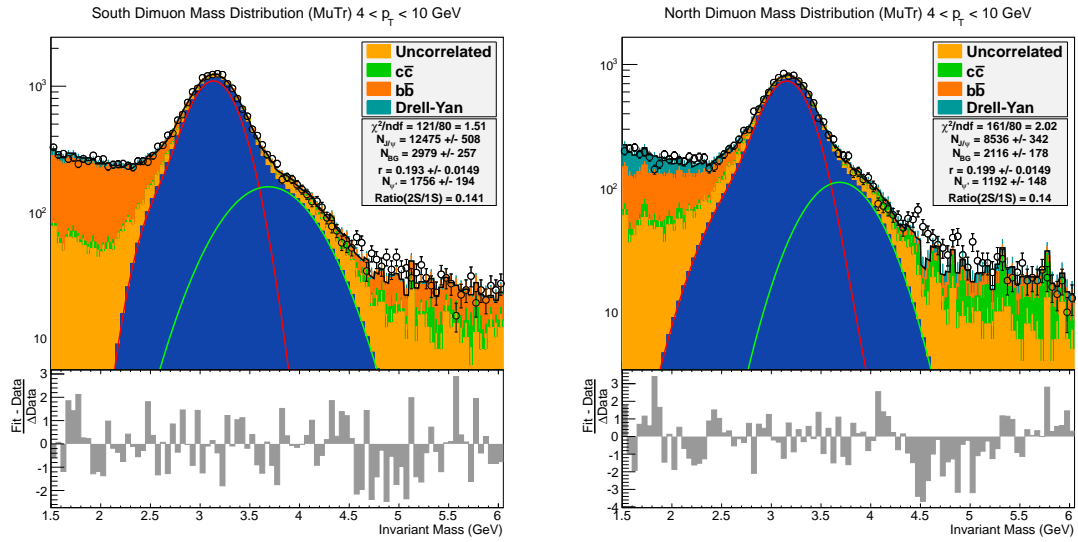
Figure 6.32: MuTr mass spectrum fits with simulated background estimation for the 4-10 GeV bin for the north and south arms and the 2σ mass window.
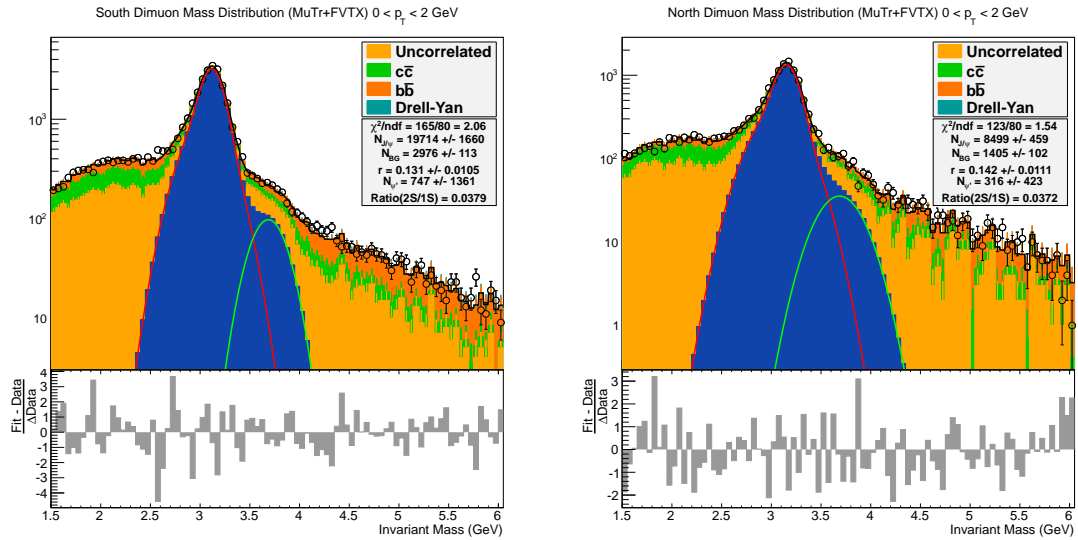
Figure 6.33: MuTr+FVTX mass spectrum fits with simulated background estimation for the 0-2 GeV bin for the north and south arms and the 2σ mass window.
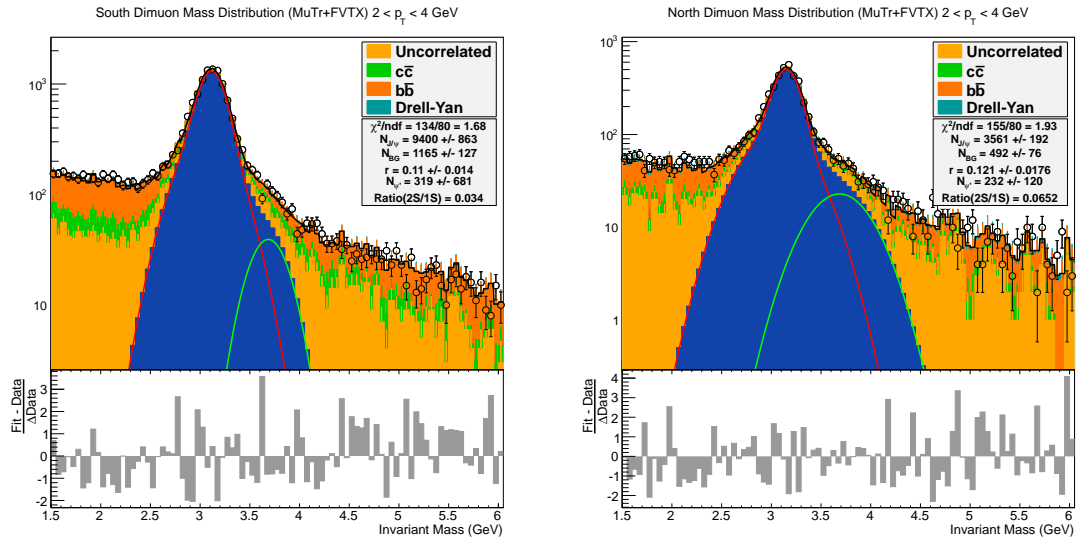
Figure 6.34: MuTr+FVTX mass spectrum fits with simulated background estimation for the 2-4 GeV bin for the north and south arms and the 2σ mass window.
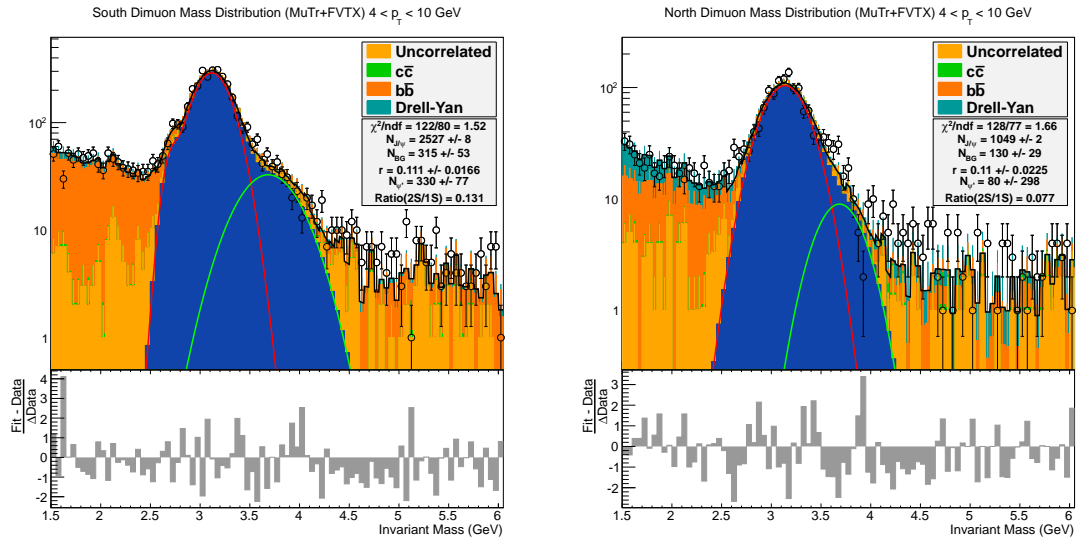
Figure 6.35: MuTr mass spectrum fits with simulated background estimation for the 4-10 GeV bin for the north and south arms and the 2σ mass window.

6.4.3 Method Bias and Systematic Error

The GPR method is now established as providing the best fits of the methods evaluated. Nonetheless, the method may still contain systematic biases that are particular to the method itself. More specifically, we try to quantify how well the GPR method, and as a cross check a third order polynomial (pol3), background fit can extract the spectrum shapes that are found in this analysis. To do so, the simulated spectrum shapes that were used in the simulated fits are used along with the uncorrelated shape from the like sign real data spectrum in a Monte Carlo study of generated background shapes.

An iteration of the Monte Carlo is outlined as follows:

- Sample crystal ball functions for J/ψ and ψ'

- Generate background fraction and signal counts to reflect real data yields

- Randomly sample and scale background spectra to form generated background fraction

- Only accept generated spectrum if $\chi^2(\text{Gen}, \text{Data}) < 5$ in BG region

- Fit output spectra with GPR/pol3 method and crystal ball functions

- Extract background fraction and compare with input

Through this procedure we generate spectrum shapes that are similar in both shape and statistics of the real data spectrum that we are attempting to study. The rejection of dissimilar shapes guarantees that the spectra sampled are reasonable and the conclusions arrived at through the study will be applicable to the real data sample as well. Examples of the generated spectra are shown in Figure 6.36.
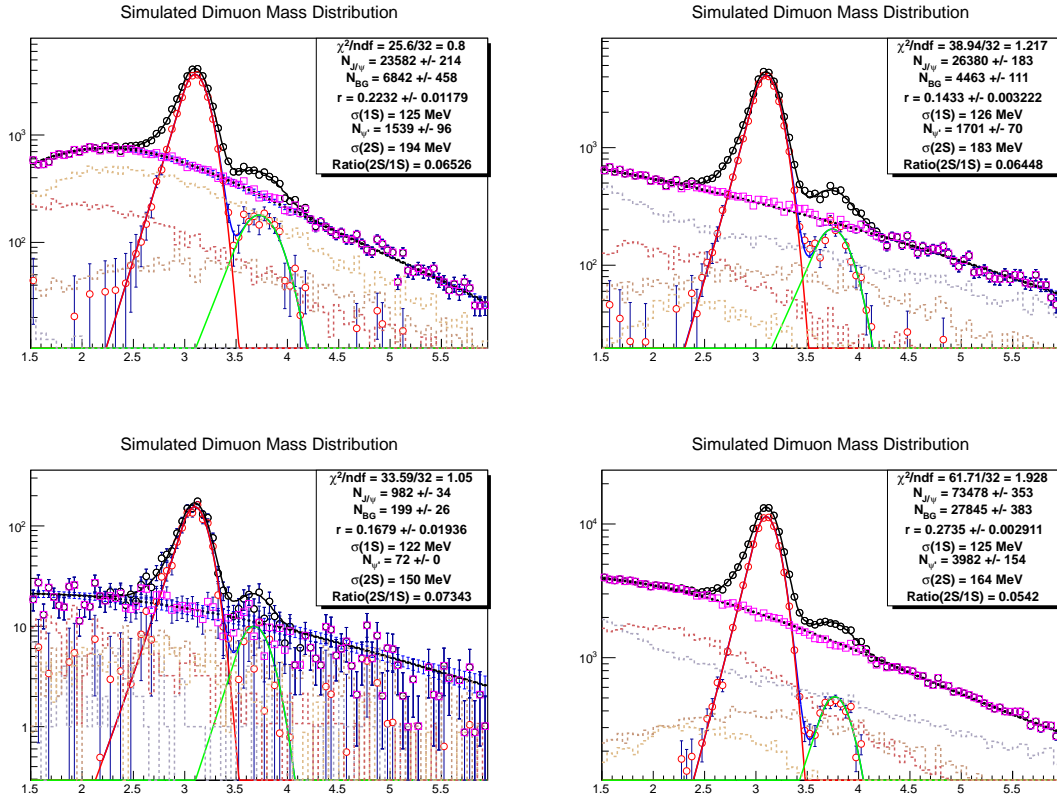
Figure 6.36: Randomly generated mass spectra from the simulated background and randomly sampled crystal ball functions

In each iteration the pull distribution and relative error in the extracted background fraction is extracted and the distributions after many iterations are shown in Figure 6.37 and Figure 6.38 respectively. If the methods have no bias and properly estimate the statistical uncertainties then the distributions should all be $\mathcal{N}(0,1)$.

In the pull distribution it can be observed that both the GPR and pol3 methods have biases that are a function of p_T (i.e., shape). However, the biases for the pol3 method are (much) larger and/or have larger fluctuations (as one would hope). Therefore, the pull distributions are in favor of the GPR method, but that could just indicate that pol3 method underestimates statistical errors as the pulls are normalized by the statistical error.
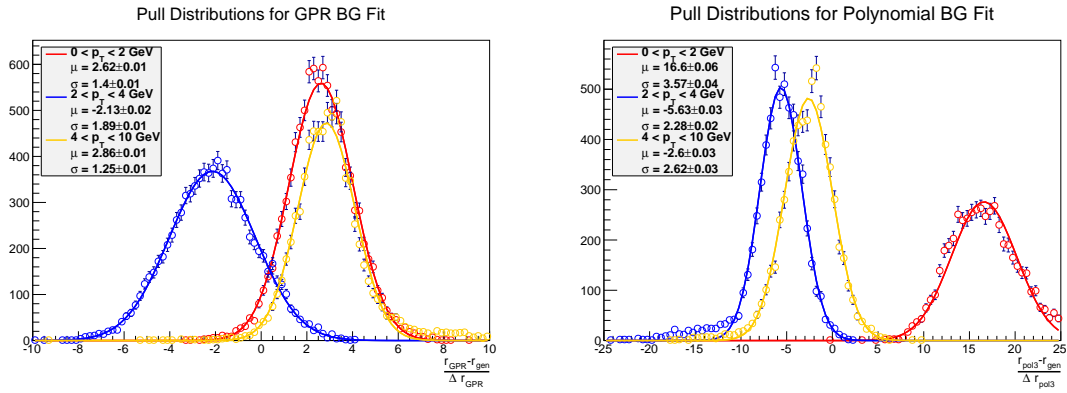
Figure 6.37: Pull distributions of the extracted background fraction for the GPR and pol3 methods
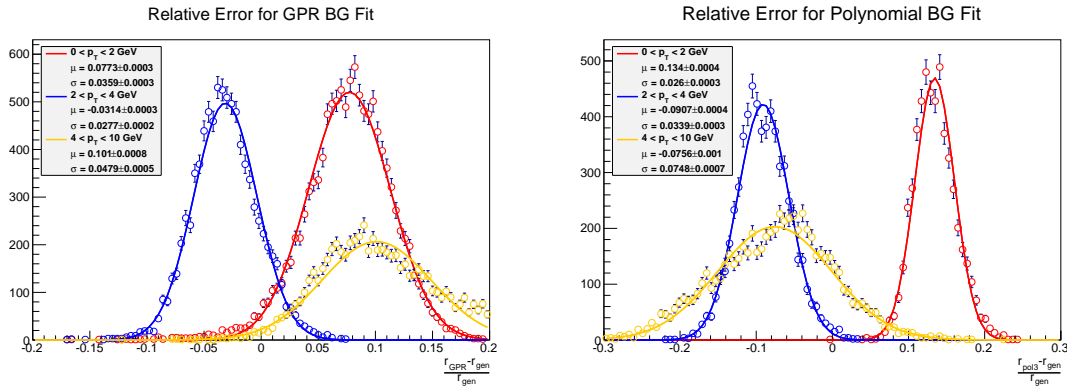
Figure 6.38: Relative error distributions of the extracted background fraction for the GPR and pol3 methods

The relative error is also comparable or smaller with the GPR method. The fluctuations (widths) are roughly equivalent from the two methods, and there are possible issues with both methods at low statistics (yellow) where the distributions begin to take a non-gaussian form. The relative error, again, is in favor of the GPR method where it outperforms the pol3 method by up to a factor of two. Also, with a high confidence in the simulations, this Monte Carlo study coulde used to correct the background fractions from the GPR method. Unfortunately, this is not the case and as such we assign a systematic error equal to the mean offset to account for the

potential bias.

6.4.4 Final Background Fractions

The extracted background fractions for all of the previously introduced methods can be found in Appendix D and the results are summarized in Figure 6.39 for both mass windows.
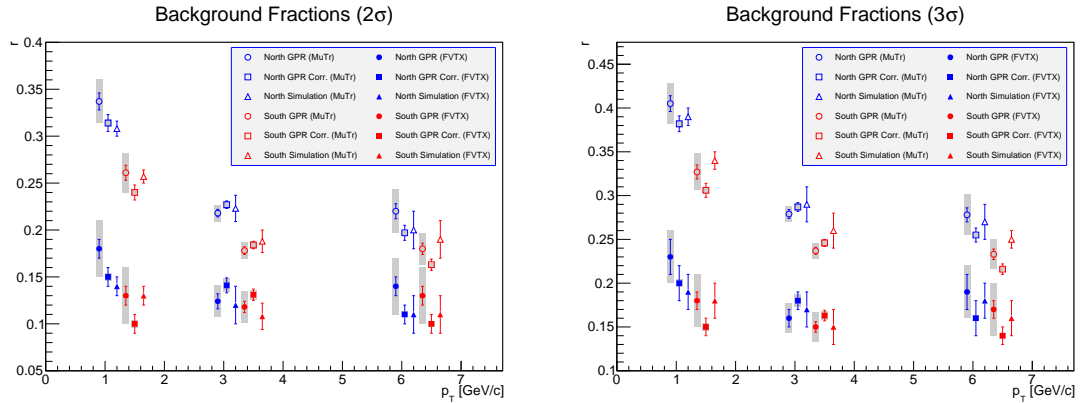
Figure 6.39: Background fraction comparison for all methods and all detector and p_T combinations

Finally, the background fractions used for the remainder of the analysis are the mean values of the GPR method with a systematic taken as the difference between the GPR and simulated background fractions and are shown in Table 6.2, Table 6.3, and summarized in Figure 6.40
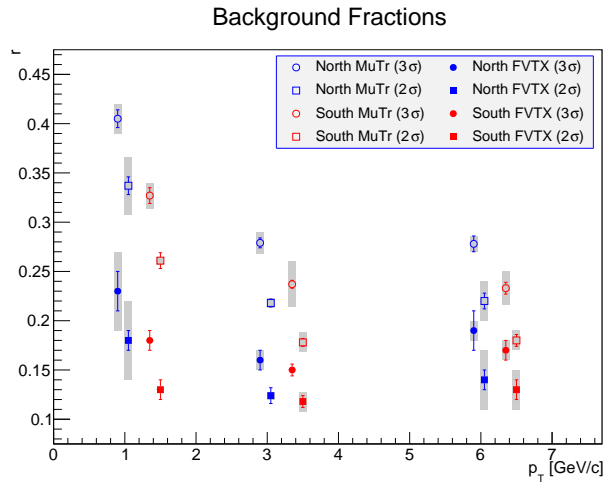
Figure 6.40: Final background fractions with mean value and statistical errors from GPR method, systematic from simulation for both mass windows.

Detector	$p_T \in [0,2]$ GeV	$p_T \in]2,4]$ GeV	$p_T \in]4,10]$ GeV
MuTr N	$0.337 \pm 0.009 \pm 0.029$	$0.218 \pm 0.004 \pm 0.005$	$0.22 \pm 0.008 \pm 0.02$
MuTr S	$0.261 \pm 0.008 \pm 0.004$	$0.178 \pm 0.004 \pm 0.01$	$0.18 \pm 0.006 \pm 0.01$
FVTX N	$0.18 \pm 0.01 \pm 0.04$	$0.124 \pm 0.008 \pm 0.004$	$0.14 \pm 0.01 \pm 0.03$
FVTX S	$0.13 \pm 0.01 \pm 0$	$0.118 \pm 0.006 \pm 0.01$	$0.13 \pm 0.01 \pm 0.02$

Table 6.2: Final background fractions with mean value and statistical errors from GPR method, systematic from simulation (2σ)

Detector	$p_T \in [0,2]$ GeV	$p_T \in]2,4]$ GeV	$p_T \in]4,10]$ GeV
MuTr N	$0.405 \pm 0.009 \pm 0.015$	$0.279 \pm 0.005 \pm 0.011$	$0.278 \pm 0.008 \pm 0.008$
MuTr S	$0.327 \pm 0.008 \pm 0.013$	$0.237 \pm 0.004 \pm 0.023$	$0.233 \pm 0.006 \pm 0.017$
FVTX N	$0.23 \pm 0.02 \pm 0.04$	$0.16 \pm 0.01 \pm 0.01$	$0.19 \pm 0.02 \pm 0.01$
FVTX S	$0.18 \pm 0.01 \pm 0$	$0.15 \pm 0.006 \pm 0$	$0.17 \pm 0.01 \pm 0.01$

Table 6.3: Final background fractions with mean value and statistical errors from GPR method, systematic from simulation (3σ)

6.5   Relative Luminosity

The use of detector measured luminosities only works under the assumption that the detector cross section is spin independent. To this effect we will explore the possible relative asymmetries that may exist between the various luminosity monitoring detectors to quantify the overall systematic uncertainty in our determination of the relative luminosity.

6.5.1   Procedure

As is now established procedure, we study the ratio of counts provided by two different detectors that "see" different physics. This assumption is based off the detectors sitting at different rapidity ranges and triggering on different particles. If there is no asymmetry in the ratio then it is assumed that there is no *relative* asymmetry between the two detectors. There is still no guarantee that each detector cross section does not have an asymmetry as they could conspire to cancel when taking the ratio. This ratio, $r_i = N_{\mathrm{ZDC}}/N_{\mathrm{BBC}}$, is studied as a function of crossing as bunch to bunch variations may exist. Within a fill, the raw relative asymmetry, ε_{LL} is extracted by a fit of the crossing by crossing ratio to the function

$$r = C\left(1 + \varepsilon_{LL}S_B S_Y\right) \tag{6.9}$$

where $S_{B(Y)}$ is the sign of the blue (yellow) beam helicity and C is a constant. The relative physical asymmetry between two detectors D_1 and D_2 is then

$$A_{LL}^{D_1/D_2} = \frac{\varepsilon_{LL}}{P_B P_Y} \tag{6.10}$$

6.5.2   Corrections

The raw counts as provided by the BBC and ZDC must be corrected for the presence of multiple collisions given the binary nature of the BBC/ZDC triggers. In a crossing with more than one interaction the two detectors can still only count at most one collision. The FVTX does not suffer from this limitation as it counts all hits produced in the detector above a minimum threshold and does not depend on coincidence between arms at the cost of increased backgrounds. Multiple collision rates in Run 13 are the highest that RHIC has ever seen and the corrections will play a large role in the final uncertainty on the relative luminosity. While benefit may eventually be extracted from the FVTX data, as of now the BBC and ZDC are used alone for determination of the relative luminosity systematic. Without applying a rate
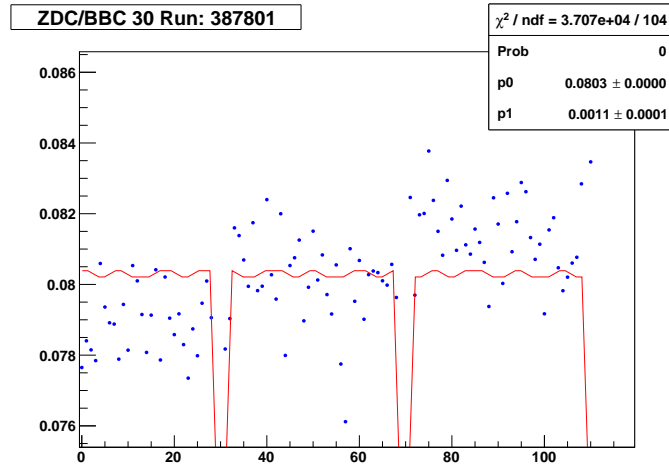
Figure 6.41: Ratio of ZDC and BBC counts with a 30 cm vertex cut vs. crossing number for run 387801

correction (e.g., Figure 6.41) the fluctuations in the ZDC to BBC ratio from crossing to crossing are many times larger than the statistical error. The reduced χ^2 of a constant fit is, understandably, quite poor at ~ 350.

After applying the rate correction, as derived in Appendix A, the fluctuations
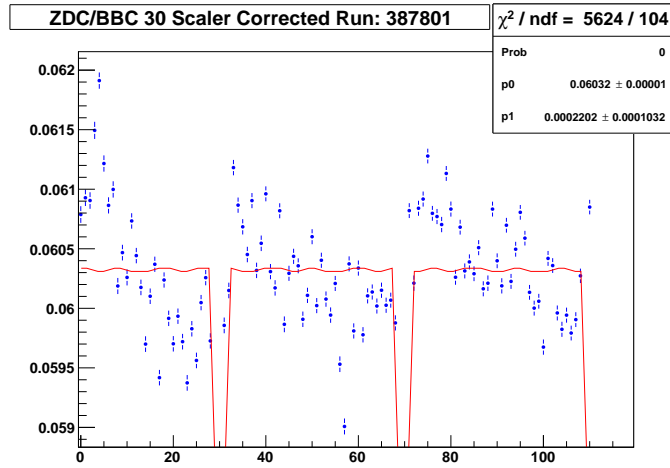
Figure 6.42: Ratio of rate corrected ZDC and BBC counts with a 30 cm vertex cut vs. crossing number for run 387801

from crossing to crossing are reduced with respect to the statistical errors as is reflected in the improved χ^2 of ~ 56. However, this fit value is far from ideal and further work will be needed to understand relative luminosity sufficiently well for higher statistics asymmetries. The effect of the rate correction is readily observed in Figure 6.43 as the run to run asymmetry distribution width is dramatically improved.

Figure 6.44 shows the run dependence of the ZDC to BBC asymmetry for the entire set of runs from Run13. The systematic effects due to rate are clearly absent as there is no large variation from run to run within adjacent runs belonging to the same fill. However, there still exist large jumps from fill to fill that are not statistically distributed. Ideally, one would take the fit value to be the unresolved asymmetry. However, given the clear problems (reflected in the large χ^2) we will conservatively take the full unresolved spread as a systematic for the J/ψ A_{LL}: $\epsilon_{LL} = 0.0005$.
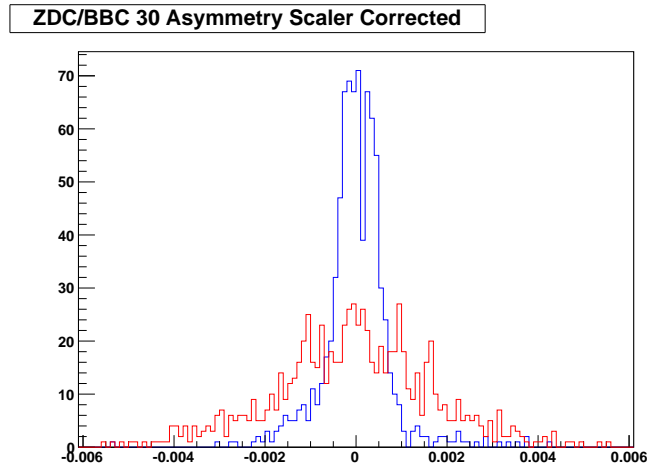
Figure 6.43: Distribution of the relative asymmetry between the ZDC and BBC with a 30 cm vertex cut with (blue) and without (red) the rate correction
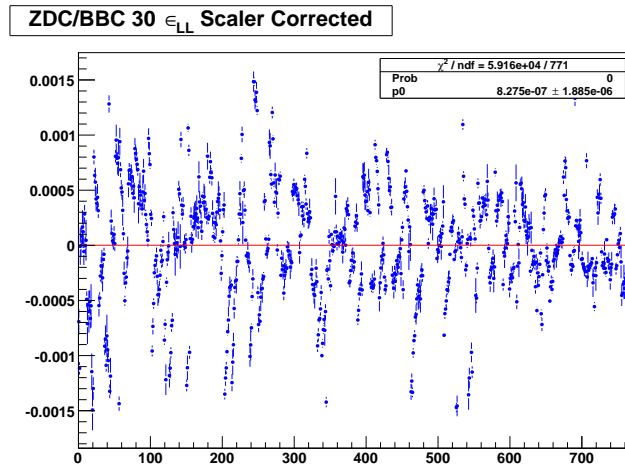
Figure 6.44: Asymmetry between the ZDC and BBC vs. run for the Run13 period. Systematic jumps are seen from fill to fill.

6.5.3   FVTX

As introduced in detail in section 5.3 the FVTX was augmented to function as a luminosity monitor in order to provide a third detector capable of producing a relative luminosity measurement. This section presents an overview of the data acquired during the Run13 period and comparisons with the relative luminosity as determined by the ZDC and BBC. As the implementation of luminosity monitoring, or scaling, in the FVTX does not have a method of requiring that the event vertex be within a certain range the FVTX data will only be compared to the BBC and ZDC data without a vertex cut applied. This restricts the use of the FVTX relative luminosity to analyses where no vertex cut is applied. Nevertheless, the FVTX can provide necessary insight as to the underlying source of the systematic discrepancy in the relative luminosity as seen by the BBC and ZDC.
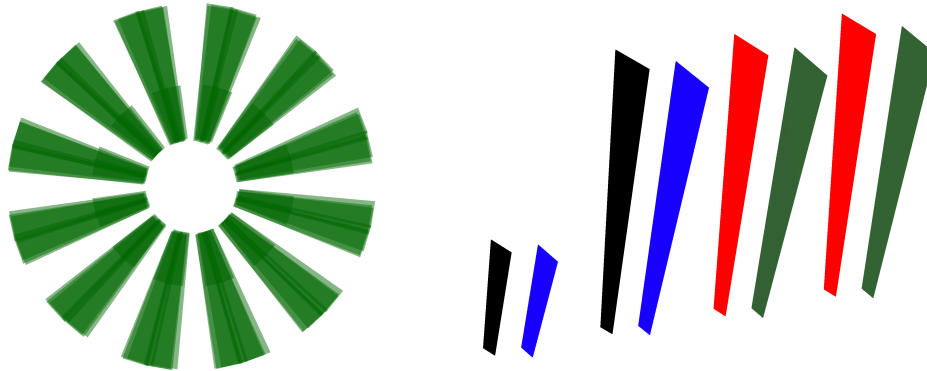
Figure 6.45: Left: Sensor area covered by "single" flavor in a single arm from the head-on perspective (xy projection). The "station-coincidence" flavor forms the complementary set of sectors. Right: Separation of wedges in a single sector into channels (colors). The PHENIX z axis goes from left to right and the smaller sensor area of the first station is visible.

The distribution of the wedges over which the counts are summed are visualized in Figure 6.45 where the azimuthal distribution of the scaler flavors is shown as well

as the physical distribution of the wedges in two neighboring sectors (those serviced by a single FEM) are separated into FEM channels. That is, they are located in the same ϕ sector and adjacent in z. Due to the geometry of the FVTX detector the acceptance is only roughly constant within a ± 10 cm window. Logically, this acceptance falls when the collision vertex is underneath one of the detector cages. This can been seen in Figure 6.46 and Figure 6.47 as the dips in the number of hits per channel per collision around ± 30 cm. The four colors corresponding to the FEM channels for the first two stations and the last two stations on the north and south arm have visibly different acceptances due to the difference in z positions.
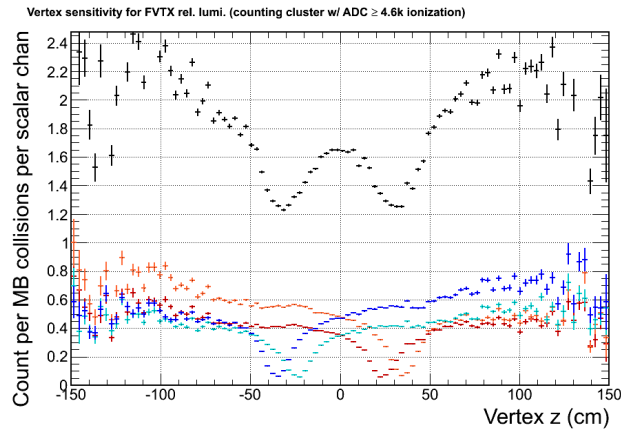
Figure 6.46: "Single" vertex sensitivity as given by the number of counts per FEM/scaler channel per minimum bias collision as extracted from simulated data. The black curve is for the entire detector and the colored lines are for each of the four geometrically distinct channels.

While the variation in acceptance for a single scaler channel can vary drastically, the sum over all scaler channels only varies by approximately 15% for the "single" flavor and 20% for the "station-coincidence" flavor. It can also be observed that as the vertex z distance becomes very large the number of counts per collision rises as it becomes possible for a single particle to deposit hits in both arms of the detector. If
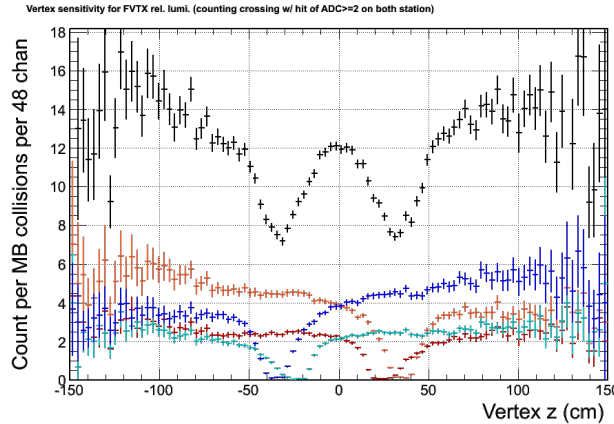
Figure 6.47: "Station-coincidence" vertex sensitivity as given by the number of counts per FEM/scaler channel per minimum bias collision as extracted from simulated data. The black curve is for the entire detector and the colored lines are for each of the four geometrically distinct channels.

the real data vertex distribution is stable from crossing to crossing in both width and mean then the correction is simply a constant factor that will cancel when taking the ratio to arrive at the relative luminosity.

Another way to quantify the extent of the vertex sensitivity of the FVTX luminosity monitor is to calculate, through simulation, the probability for an event to be counted, weighted by the number of counts that are contributed by that event. The results of this study are shown in Figure 6.48. The filled gray histogram is the simulated vertex distribution input and, as before, the FVTX response is show summed over the entire detector (black) and by channel type (colors). The sampled vertex distribution is shown to have variations from the input distribution of approximately 10%. Again, the concern is that vertex distribution variations from bunch to bunch could ruin the sensitivity to the underlying luminosity structure due to the z dependence of the FVTX vertex sampling over the full vertex range.

In Figure 6.49 a comparison of the BBC and ZDC counts without a vertex cut
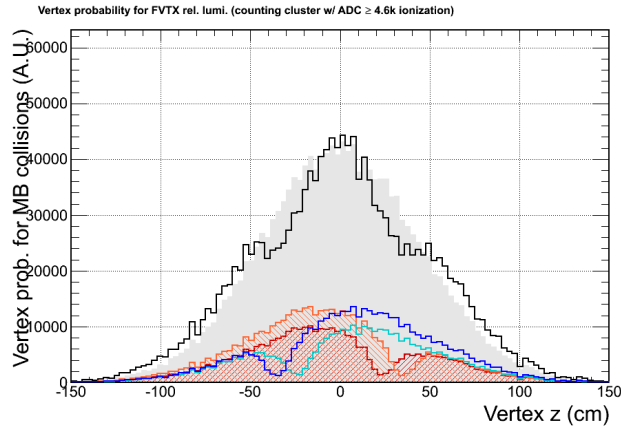
Figure 6.48: Weighted vertex distribution as sampled by the FVTX "singles". The black curve is for the entire detector and the colored lines are for each of the four geometrically distinct channels.

are shown for a single run at the beginning of Run13. The abort gap is clearly visible as a group of nine crossings between 111 and 119 where there is a large deficit of counts that reflects the unfilled bunches that pass through the PHENIX IR. Also visible are two sets of two bunches that were filled in one beam, but empty in the other beam. Using the abort gap as a reference the ZDC has backgrounds that are at a level of $\mathcal{O}(10^{-6})$ or less. The BBC has slightly more background contamination at the $\mathcal{O}(10^{-5})$ level. As is expected, the FVTX based luminosity monitor has a much higher background level which is $\mathcal{O}(10^{-2})$ for the "singles" and $\mathcal{O}(10^{-3})$ for the "station-coincidence".

The impetus of the creation of the FVTX luminosity monitor was to provide a high precision relative luminosity measurement to improve on the existing measurements. Therefore, it must be proven that the significantly higher background levels do not prevent the FVTX from providing an accurate measurement. The relative luminosity values obtained for the runs in a single fill in Run13 are shown in Figure 6.50. From this typical fill the values obtained by the FVTX typically agree with
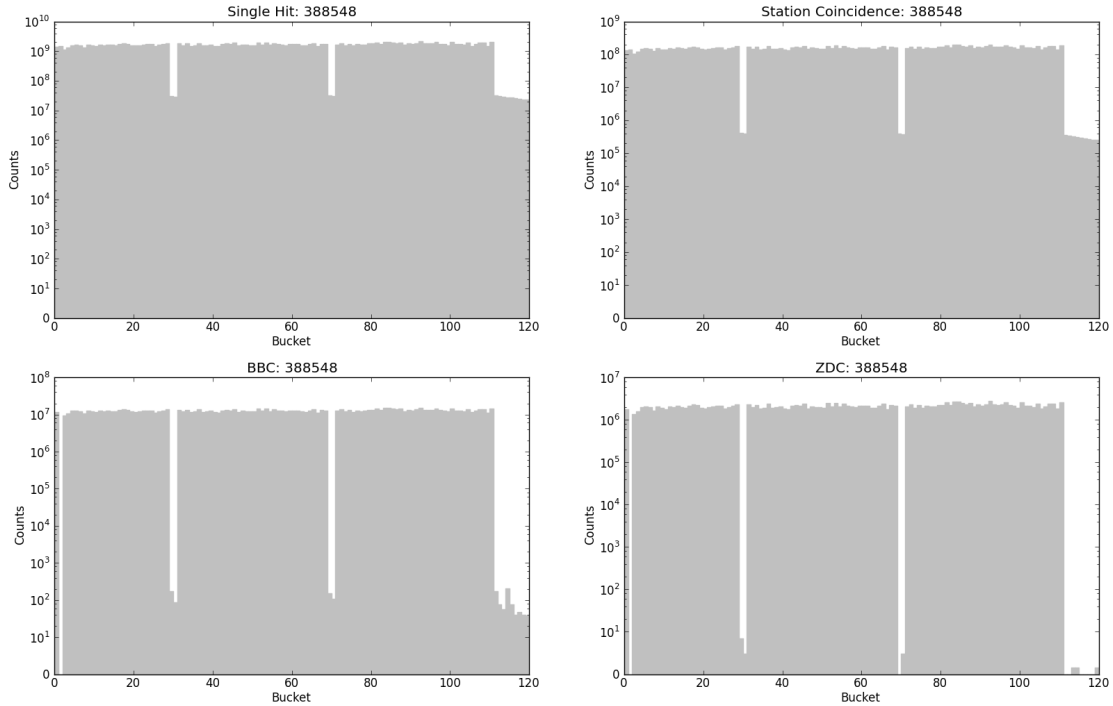
Figure 6.49: Counts vs. crossing for the four detector subsystems capable of providing an online luminosity measurement. The overall crossing dependence is consistent between the different detectors.

the rate corrected BBC and ZDC to within 5×10^{-4}. It can also be observed that the overall trend followed by the BBC and ZDC from run to run is followed by the FVTX as well. However, it can also be observed that the discrepancy between the FVTX and BBC is largely due to a systematic offset that is many times larger than the statistical uncertainties involved. Even within the two types of FVTX scalers there is a consistent offset, albeit much smaller, of approximately 1×10^{-4} or less. Figure 6.51 separates the relative luminosity values given by the FVTX "single" scaler by quadrant (i.e., NE, NW, SE, SE). Agreement is shown to within 5×10^{-5} or less.

The two types of FVTX scalers differ in three ways: the sensitivity to multiple
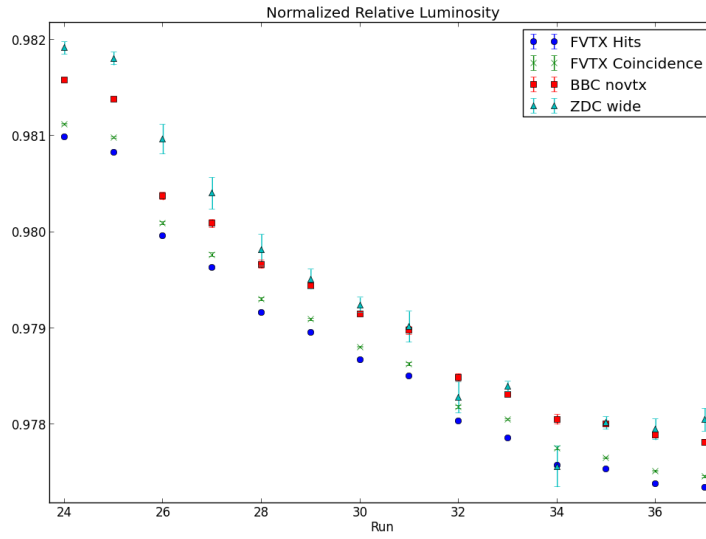
Figure 6.50: Relative luminosity values from all subsystems for one fill in Run13
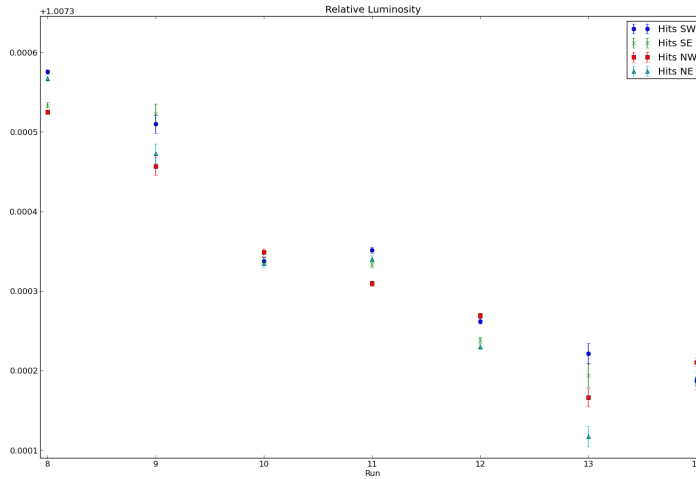
Figure 6.51: Relative luminosity values obtained by the singles scalers for a single fill separated by FVTX cage

Interactions	$\%_{cross}$
1	28.4%
2	27.0%
3	17.1%
4	8.16%
5	3.11%
6	0.99%

Table 6.4: Percentage of crossings with a given number of distinct collisions for a BBC rate of 4 MHz

collisions, the vertex sensitivity, and the sensitivity to non-collision related backgrounds. The percentage of crossings having a given number of interactions is shown in Table 6.4 which is calculated by estimating that the distribution of interactions follows a Poisson distribution in the collision rate. Clearly, multiple collisions are an extremely important effect in Run13 where BBC rates approach 5 MHz and the RHIC crossing rate is 9.4 MHz. The multiple collision sensitivity differs due to the fact that each "station-coincidence" scaler channel, similar to the BBC and ZDC, cannot fire more than once per crossing. However, in contrast to the BBC and ZDC there are 96 independent channels that are also spatially separated. Therefore, the "station-coincidence" scaler will count each collision with a number equal to the number of channels fired that will be a number between 0 and 96. If within a single crossing we have more than one collision such that a particle from each collision passes through the same channel, then only a single particle will be counted, leading to errors due to under-counting. The "singles" scaler also suffers from this problem, but only at the level of a single FPHX channel of which there are over 5×10^5. The change in the distribution of hits per event when going from a single collision per crossing to an extreme case of ten collisions in a single crossing can be seen in Figure 6.52.

As the FVTX counts the number of fired scaler channels per crossing, the ex-
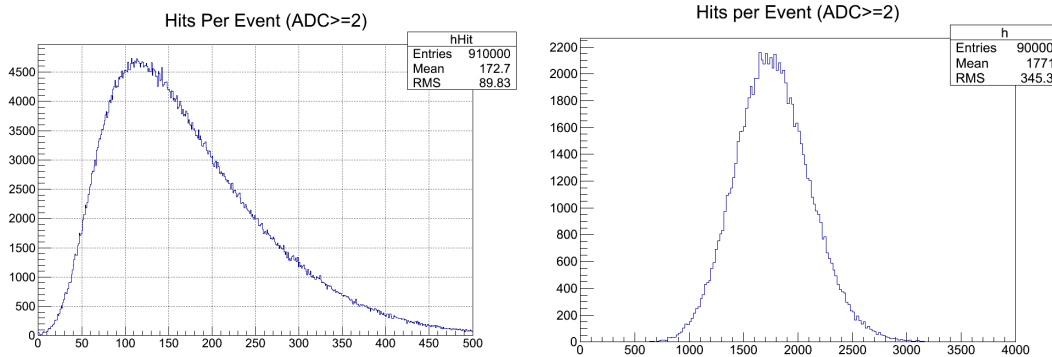
Figure 6.52: Distribution of hits produced in the singles scalers in a single collision (left) and a 10 collision (right) minimum bias pp event at $\sqrt{s} = 510$ GeV with an ADC value greater than one as is required in the scalers.

tracted counts are not numbers of collisions, but rather a number that is proportional to the number of collisions where the proportionality constant is the mean number of channels that are fired in a single collision. The evolution of the mean number of fired channels is studied for the statistically probable multiplicity values seen in Table 6.4 for both the "singles" and "station-coincidence" scalers in Figure 6.53. It is readily observed that the "singles" scaler has a dependence in the mean number of channels fired per crossing that is very nearly linear. In contrast, the "station-coincidence" scaler deviates from linear scaling by greater than 10% in the case of two collisions per crossing and nearly 20% in the case of four collisions per crossing. This is still many times better than the multiple collision scaling of the BBC and ZDC detectors, which is non-existent, and requires a rate correction. Nevertheless, it is shown that the "station-coincidence" scaler will have a stronger rate dependence than the "singles" scaler. This, therefore, cannot be the source of the systematic offset seen between the two scaler flavors as the offset remains constant over a wide range of rates from the beginning of a fill to the end where the multiple collision rate also varies accordingly.
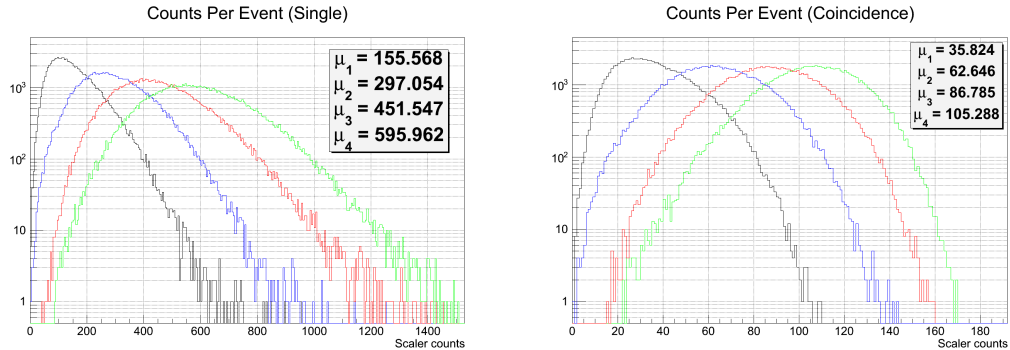
Figure 6.53: Distribution and mean value of hits produced in the "singles" scalers (left) and "station-coincidence" (right) for event multiplicity from one to four at $\sqrt{s} = 510$ GeV with an ADC value greater than one as is required in the scalers.

The vertex sensitivity between the two flavors is also different as has been seen in Figure 6.46 and Figure 6.47. To simulate the variation of the mean number of fired channels the vertex distributions are studied for the Run13 period on a crossing by crossing basis and fit with a gaussian functional form from which the mean and width are extracted.

Figure 6.54 displays the crossing dependence of the extracted fit parameters accumulated per run. There is a crossing shift present in these figures that has not been corrected, and therefore the abort gap is not in the usual crossings of 111-119. The crossing shift, however, is inconsequential to the analysis at hand. Both the distribution mean and the width are seen to be very stable from crossing to crossing over the entire run period with no systematic shifts observed. Nonetheless, the distribution for each crossing could allow for bunch to bunch fluctuations of a few centimeters in both mean and width. To show more clearly the bunch to bunch differences, the mean and width parameters crossing dependence are shown for a single run in Figure 6.55. The distribution of these parameters for a single bunch over the entire run period is shown in Figure 6.56, where the shapes do not deviate significantly from a statistical distribution.
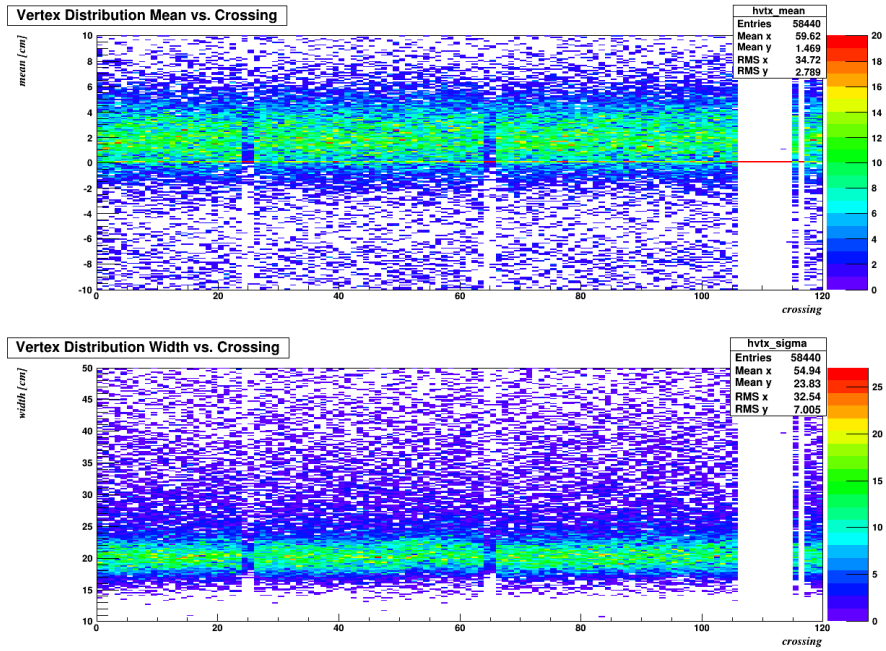
Figure 6.54: Mean and with values of a gaussian fit to the vertex distribution vs. crossing number accumulated over the Run13 period
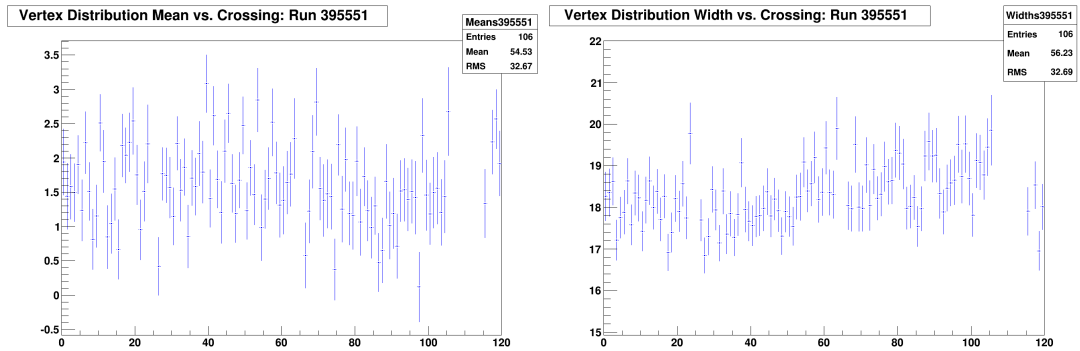
Figure 6.55: Mean and width of the vertex distribution vs. crossing for a single run: 395551

Simulated pp collisions produced in PYTHIA6 and fully propagated through GEANT 3 are produced with gaussian vertex distributions which are shifted by multiples of 5 cm. The effect on the distribution of the number of channels fired
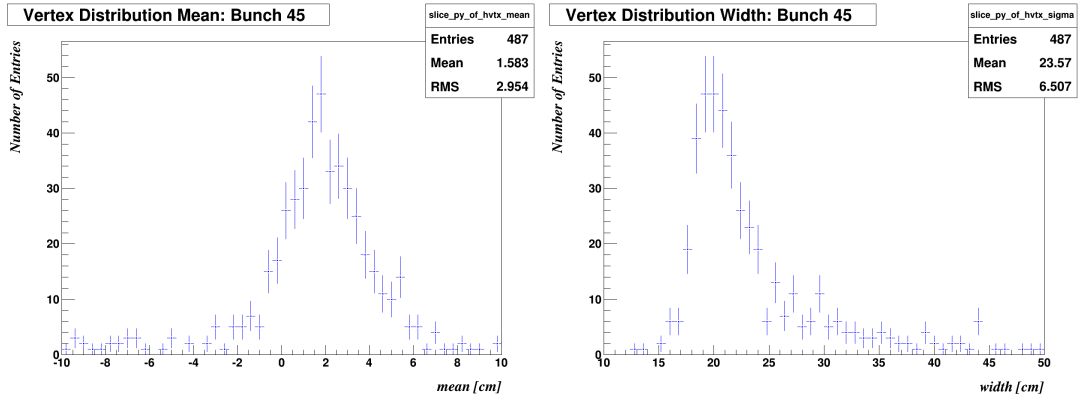
Figure 6.56: Histogram of the mean and width of the vertex distribution of a single crossing (45) over the entire Run13 period

is found to be minimal, which is perhaps naïvely surprising given the strong vertex dependence of the detector acceptance. The dependence for the "singles" is seen in Figure 6.59 and the "station-coincidence" is seen in Figure 6.58. The variation in the mean channels fired as a percentage of the mean number fired for no vertex shift is shown for the different vertex shifts is shown in Table 6.5, all of which are shown to be less than 1%.
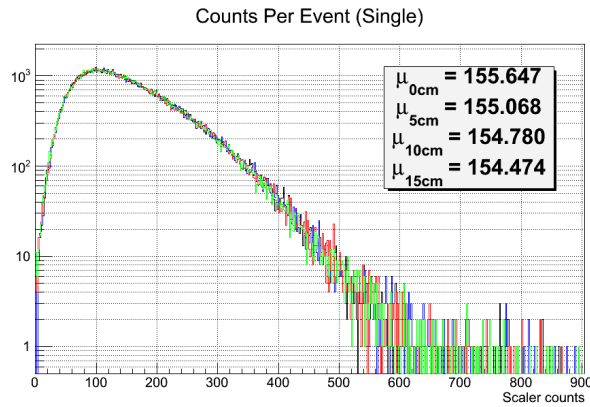
Figure 6.57: Singles hits per event distribution passing an ADC cut for various vertex distribution shifts
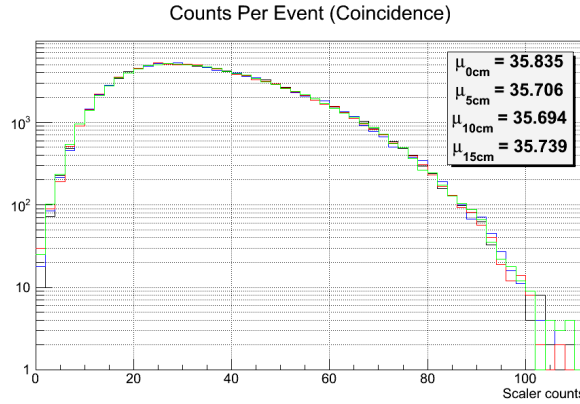
Figure 6.58: Coincidence hits per event distribution passing an ADC cut for various vertex distribution shifts

Shift (cm)	$\Delta\mu(\%)$ Single	$\Delta\mu(\%)$ Coincidence
5	0.37	0.36
10	0.56	0.39
15	0.75	0.27

Table 6.5: Variation in the average hits per event in the singles and coincidence scalers passing the ADC cut when the vertex distribution is shifted by 5, 10, 15 cm

However, the final effect on the relative luminosity of the vertex shifts and width variations cannot be seen directly in the mean channels fired per event. Therefore, a simple Monte Carlo calculation is performed with a given input relative luminosity value of 1 and normally distributed shifts from bunch to bunch. The process is repeated over 10000 trials and the relative luminosity extracted. The distribution of the extracted values is seen in Figure 6.59 and fit with a normal distribution. The gaussian, unsurprisingly, has a mean value of 1 which indicates that no bias is induced in the relative luminosity due to normally distributed bunch to bunch shifts. A bias could only be induced by a systematic shifting of the like helicity crossings with respect to the un-like helicity crossings, something for which no evidence is found.

The width of the gaussian gives us the smearing of the true relative luminosity value due to the vertex distribution shifts. The peculiar vertex sensitivity of the FVTX is therefore found to cause no bias and a loss in precision of approximately 10^{-4}.
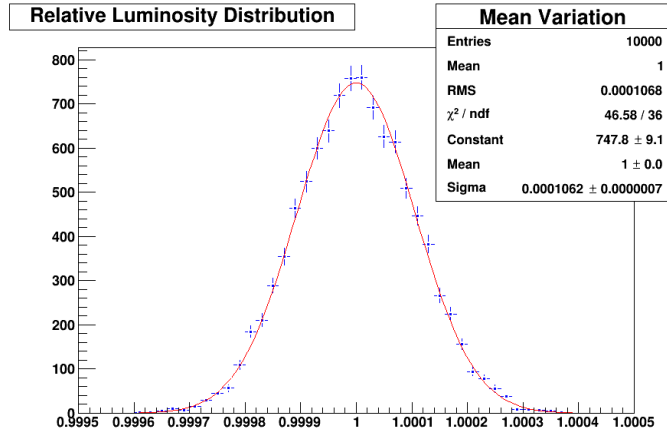
Figure 6.59: Singles distribution of relative luminosity values with an input value of 1 and bunch to bunch shift variations of 5 cm

A similar study is completed on the effect of the variation in vertex widths from crossing to crossing. The study is done for width variations of 5 cm and 10 cm. The Run13 data supports that 5 cm variations are a conservative upper limit to be representative of real data conditions. The resulting fired channels distributions are shown in Figure 6.60 and Figure 6.61 with the variations in the mean number of fired channels summarized in Table 6.6. The vertex width is found to cause less than 1% variations in the mean value, similar in size to the variations due to vertex shifts.

Once again, the variations in mean value are propagated to a Monte Carlo simulation of the relative luminosity extraction for the case of 5 cm crossing to crossing vertex width variations that are normally distributed. The procedure is repeated for 10000 iterations and the extracted relative luminosity distribution is fit with a normal distribution. For vertex width variations there is no induced bias for either scaler flavor. The smearing due to the width variations is smaller than 2×10^{-5} in

Shift (cm)	$\Delta\mu(\%)$ Single	$\Delta\mu(\%)$ Coincidence
5	0.064	0.88
10	0.47	0.65

Table 6.6: Variation in the average hits per event in the singles and coincidence scalers passing the ADC cut when the vertex distribution width is varied by 5, 10 cm
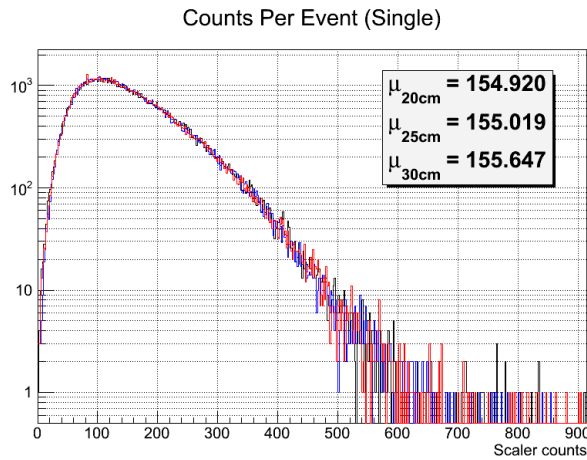
Figure 6.60: Singles hits per event distribution passing an ADC cut for various vertex distribution widths

the "singles" and smaller than 3×10^{-4} for the "station-coincidence".

Therefore, it has been determined from simulation that the systematic differences seen between the two FVTX scaler flavors are not due to vertex width or mean fluctuations, nor is it due to a rate dependent effect such as multiple collision sensitivity. The remaining factor, therefore, is the different non-collision background levels between the two types. As has been shown before, the background levels also differ greatly from those seen in the ZDC and BBC. Though it is not conclusive, it is also the most probable cause for the larger systematic differences seen with respect to those detectors.
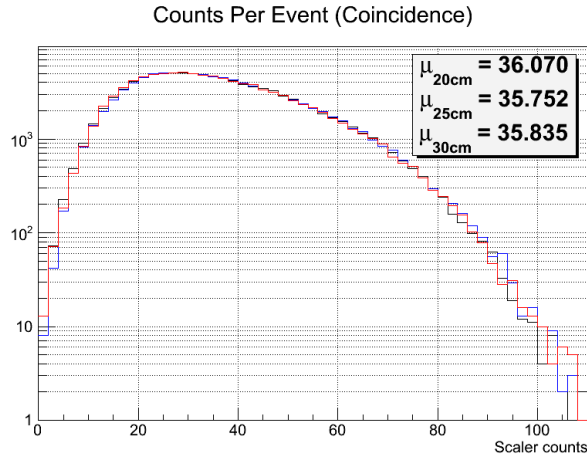
Figure 6.61: Coincidence hits per event distribution passing an ADC cut for various vertex distribution widths
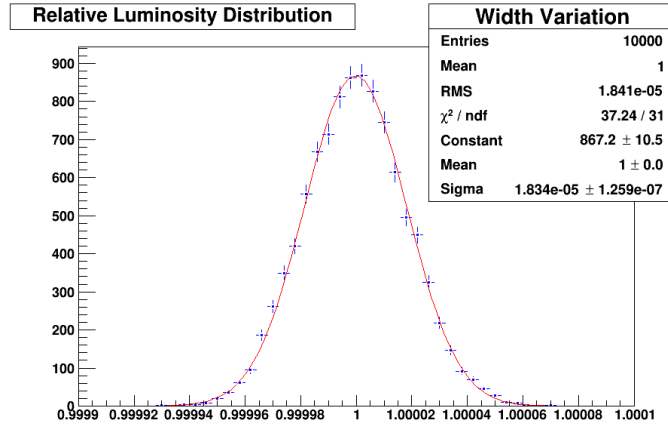
Figure 6.62: Singles distribution of relative luminosity values with an input value of 1 and bunch to bunch width variations of 5 cm

While the agreement with the BBC is shown to be better than 5×10^{-4} it is unlikely that the FVTX data, in the current form, will be able to improve the systematic uncertainty in the relative luminosity further than has already been done with the BBC and ZDC alone. The ideal implementation of the FVTX scaler would use the "hits" strategy with the addition of a coincidence requirement. This coinci-
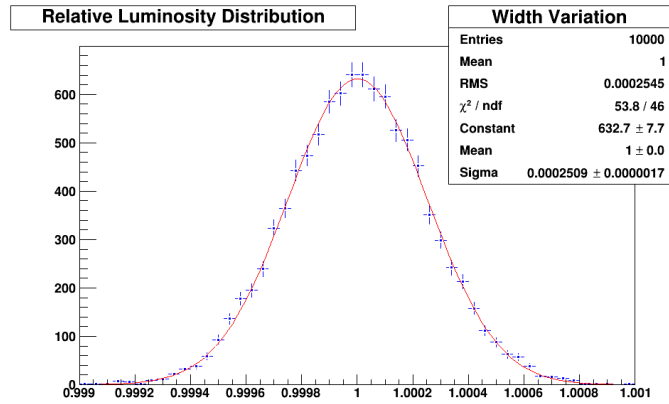
Figure 6.63: Coincidence distribution of relative luminosity values with an input value of 1 and bunch to bunch width variations of 5 cm

dence requirement could be as simple as using the BBC trigger itself as an enable signal for counting the hits within the event, which would be possible with the current hardware. This would reduce backgrounds that occur during crossings where there are no collisions, yet hits are produced in the FVTX due to particles that are co-moving with the beam. If, however, the backgrounds are hits produced at the same time as a real collision, yet are not related to the primary interaction then this simple strategy will do nothing to improve the background rejection. A more complex, but complete strategy would be to count tracks that are reconstructed online in hardware. This strategy would perform online vertex finding and require that the vertex be within a given range. With the combination of these two techniques one would preserve the linear scaling with multiple collisions as well as reduce the background levels to the same level as those seen in the BBC and ZDC.

6.6 Run Clustering

Historically, asymmetries are calculated fill-by-fill or run-by-run and averaged with the justification being that the acceptance-efficiency does not vary over the short time scales of fills or runs. Under these conditions the cancellation of acceptance-efficiency is justified given that when we experimentally extract the J/ψ counts we are integrating the J/ψ cross section, the time dependent acceptance-efficiency, and the instantaneous luminosity over the fill or run as shown in Equation 6.11

$$N_{J/\psi}^{++} = \int dt \varepsilon(t) \sigma_{J/\psi}^{++} \mathcal{L}^{++}(t) \tag{6.11}$$

Immediately, we can rule out run-by-run asymmetries for the J/ψ due to having insufficient statistics in a single run. In Run13 it has been shown that the trigger efficiency is highly rate dependent at the collision rates that were seen in Run13. This has been determined to be due to the MuID tube efficiency decreasing with the increased backgrounds. Accordingly, the dimuon efficiency can vary strongly from the beginning to the end of a fill as the BBC rates go from $\sim 5\,\mathrm{MHz}$ to $\sim 2\,\mathrm{MHz}$. Therefore, fill-by-fill asymmetries are also poorly motivated and an attempt is made to more appropriately group runs together based on having similar acceptance-efficiencies.

First, we choose two quantities that are directly related to the muon reconstruction efficiency. The muon efficiency is only nominally flat inside of a 30 cm vertex range and as such the efficiency for a given run will be a function of the vertex distribution width. A readily available proxy for that width is the ratio of BBC triggers within a 15 cm vertex and those within a 30 cm vertex. Additionally, the number of J/ψ candidates normalized by the number of minimum bias triggers in a 30 cm vertex is a direct measure of the trigger efficiency. Given these two quantities for each run we can apply a 2D clustering algorithm used in machine learning for feature extraction when the number of features is not known. The particular algo-

rithm chosen is known as the Mean Shift algorithm [52] that, in a short summary, calculates the mean distance of a cluster center to the neighboring points and in each iteration shifts the center of the cluster to the position that minimizes that mean. When applied to this dataset the algorithm detects 34 distinct clusters for Run13 that have similar acceptance-efficiencies. One complication of using this method is that now the polarization used to calculate the asymmetry of a given subset of runs is the luminosity weighted average polarization of each individual fill from which the runs were extracted.
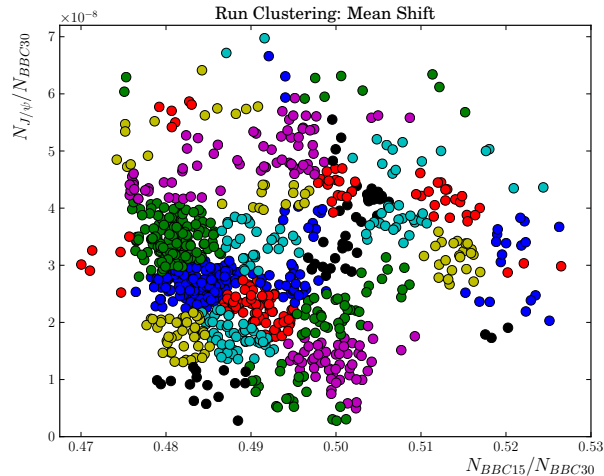
Figure 6.64: Clustering of runs in Run13 as determined by the Mean Shift algorithm applied to proxies for the J/ψ rate and the vertex width. Note: colors are re-used and points of the same color that are not spatially connected do not belong to the same cluster.

6.7   Inclusive and Background Asymmetries

The inclusive and background asymmetries as extracted for the above defined run groupings are shown in Figure 6.65 through Figure 6.68. The remaining asymmetry

cases are covered in Appendix E. The background asymmetry is calculated from the like sign and sideband asymmetries as given by Equation 6.4 and the extracted background fractions as given by Table 6.2 and Table 6.3.
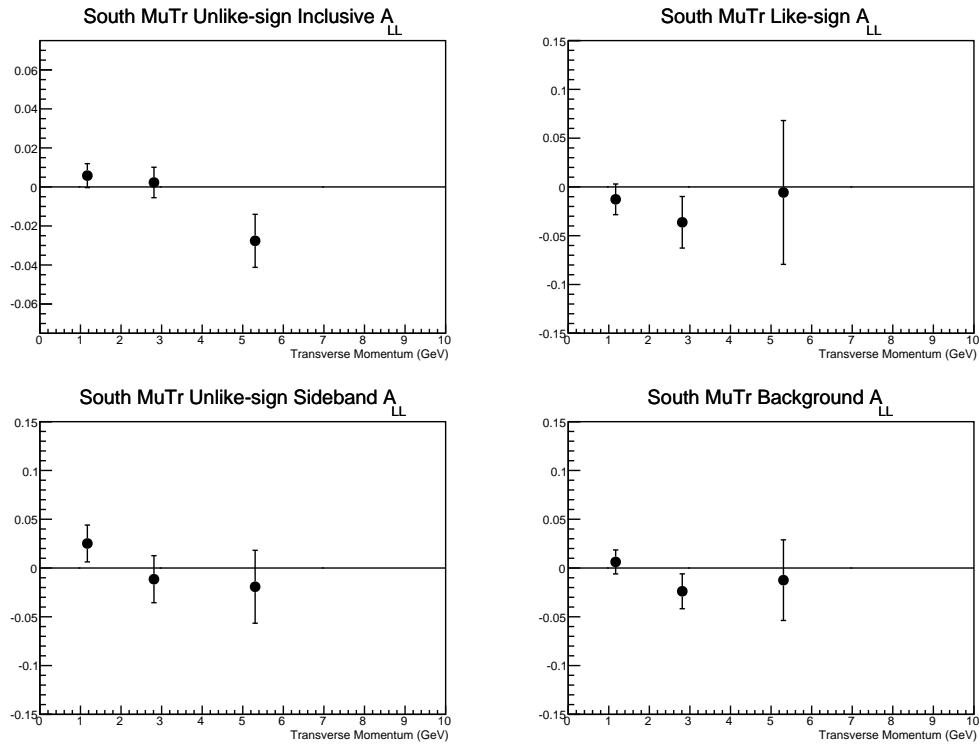
Figure 6.65: Inclusive and background asymmetries for the south MuTr 2σ dataset
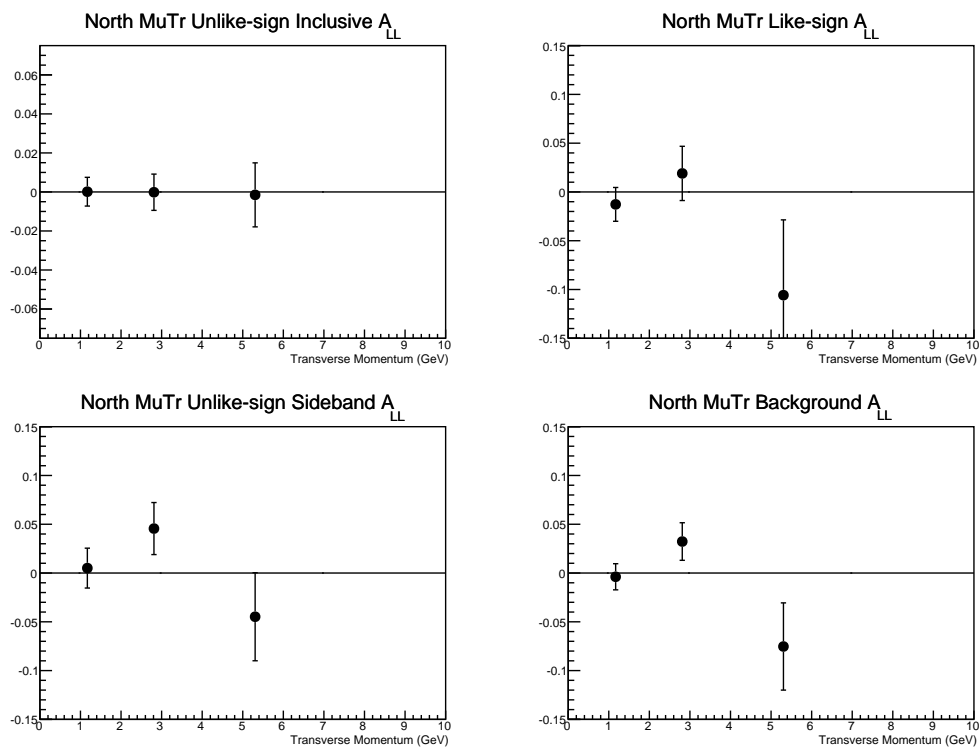
Figure 6.66: Inclusive and background asymmetries for the north MuTr 2σ dataset
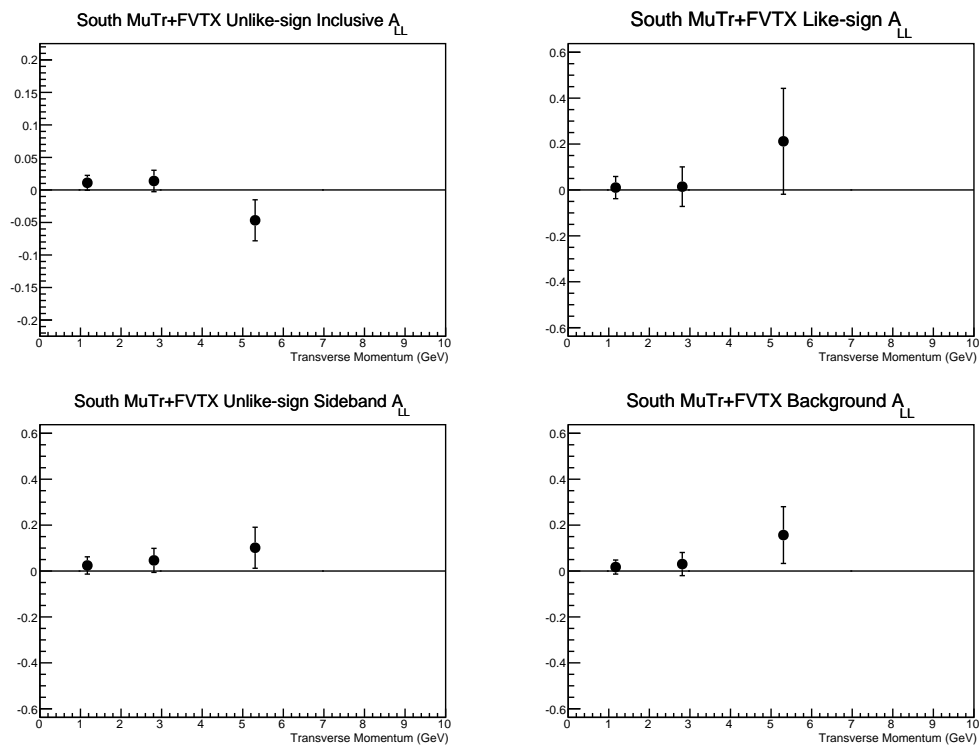
Figure 6.67: Inclusive and background asymmetries for the south MuTr+FVTX 2σ dataset
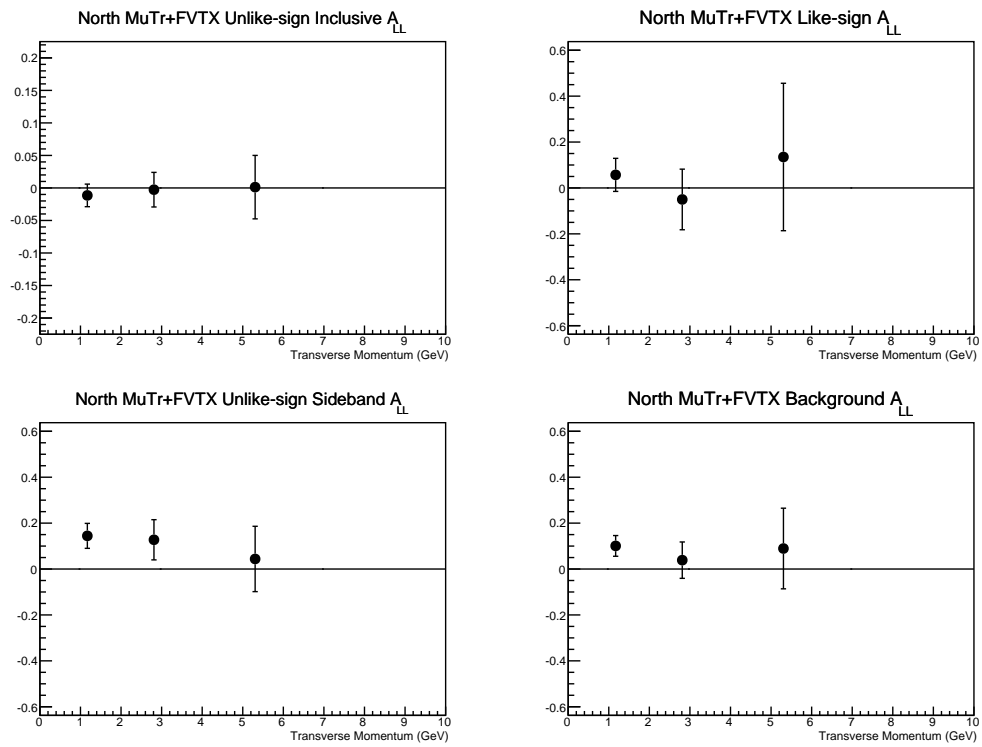
Figure 6.68: Inclusive and background asymmetries for the north MuTr+FVTX 2σ dataset

6.8 J/ψ A_{LL}

Having obtained the inclusive and background asymmetries, the signal asymmetry can be calculated from Equation 6.4 and Equation 6.5. The results are show for each arm in Figure 6.69 through Figure E.6. The arm separated results are then combined and the arm combined results are then combined between the MuTr and MuTr+FVTX datasets as shown in Figure 6.71 through Figure 6.72.

6.8.1   Arm Separated Signal Asymmetries
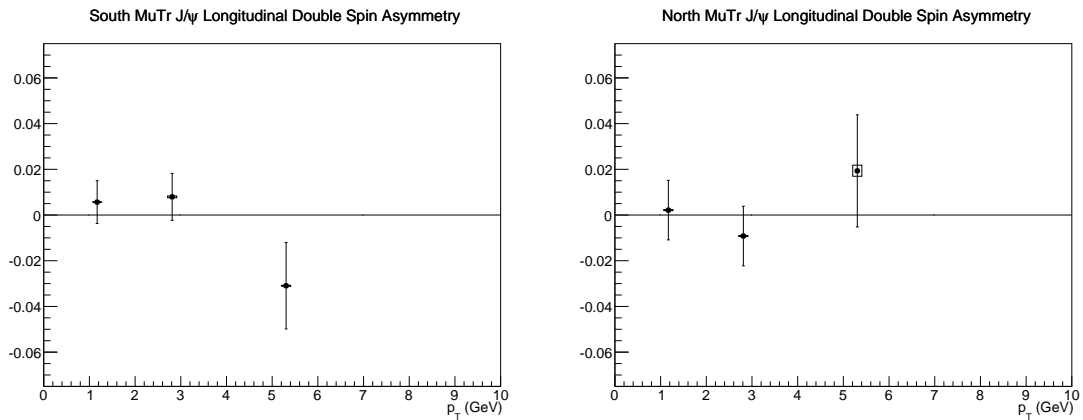
Figure 6.69: 2σ signal asymmetries for the south (left) and north (right) MuTr.
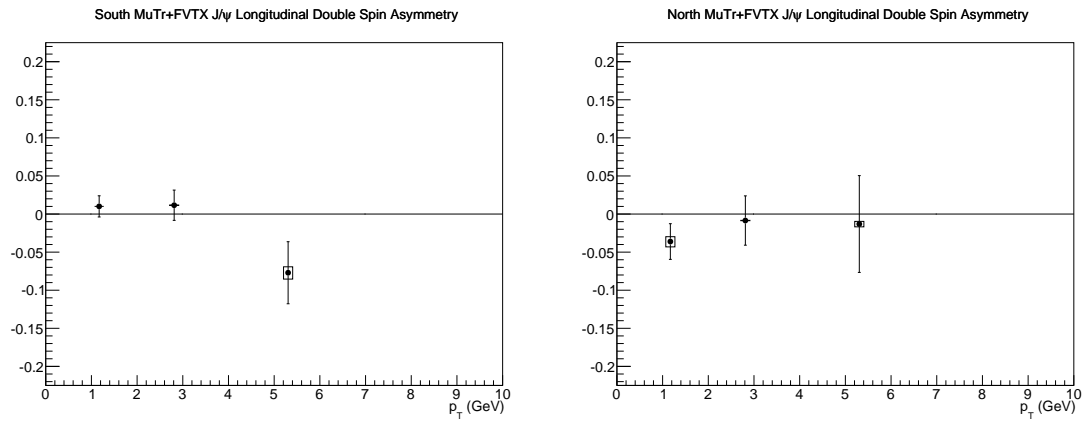
Figure 6.70: 2σ signal asymmetries for the south (left) and north (right) MuTr+FVTX.

6.8.2   Combined Signal Asymmetries
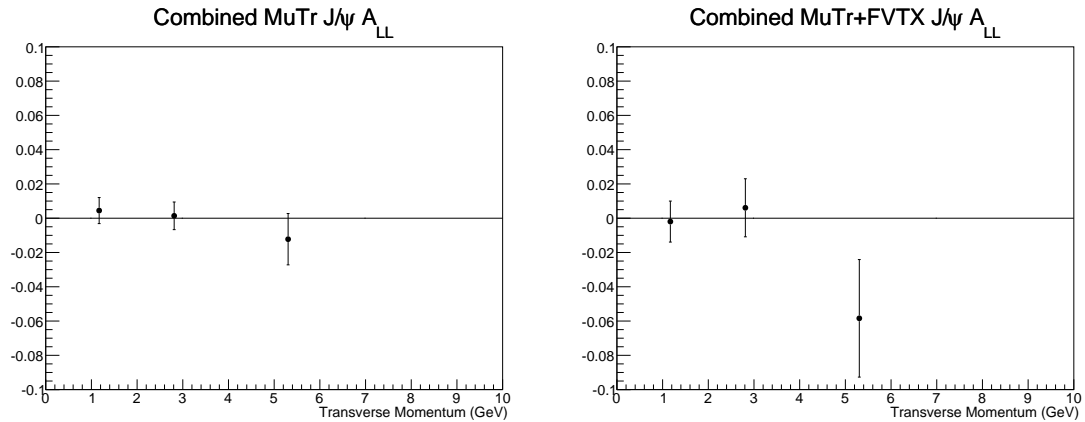
Figure 6.71: 2σ signal asymmetries for the MuTr (left) and MuTr+FVTX (right) subsets after combining the asymmetries for the north and south arms.
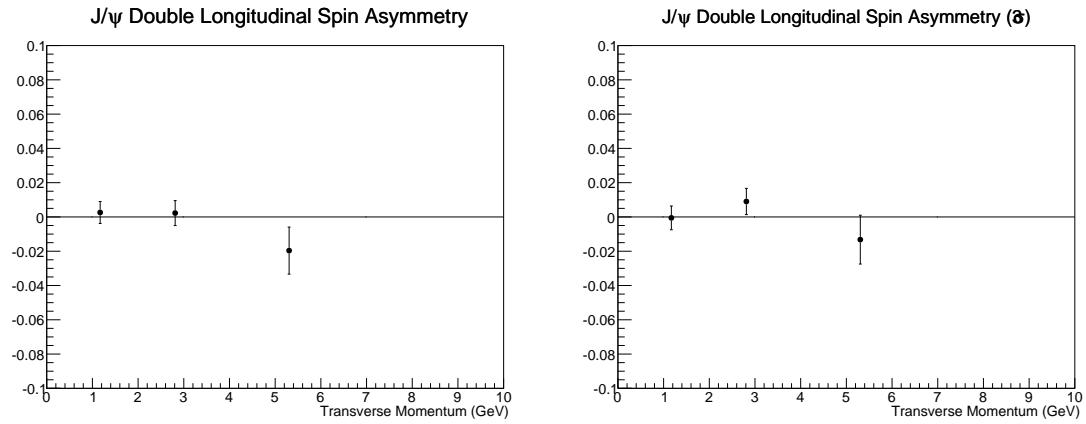
Figure 6.72: Signal asymmetries for the 2σ (left) and 3σ (right) subsets after combining the asymmetries for the MuTr and MuTr+FVTX datasets.

6.9   Summary and Final Results

The final J/ψ A_{LL} with full propagation of systematic errors with the additional systematic from the variation of the asymmetry with the variation of the mass window is shown in Figure 6.73 and summarized in Table 6.7.
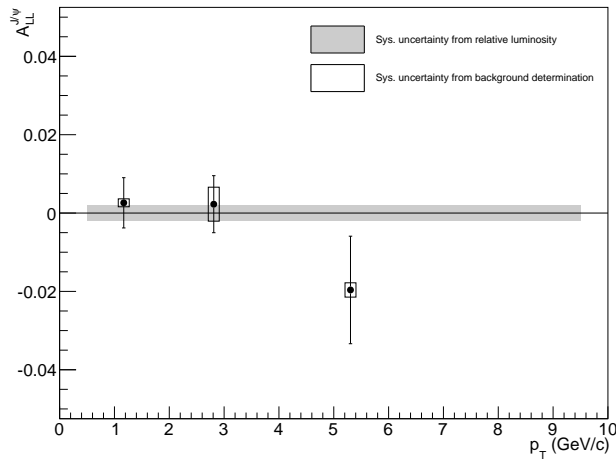
Figure 6.73: Final Run13 J/ψ A_{LL} result with systematic errors from relative luminosity, background fraction, and asymmetry variation when changing the mass window.

p_T GeV/c	$\langle p_T \rangle$ GeV/c	$A_{LL} \pm \delta A_{LL}^{stat} \pm \delta A_{LL}^{sys}$
$0-2$	1.17	$0.0026 \pm 0.0064 \pm 0.0010$
$2-4$	2.81	$0.0022 \pm 0.0073 \pm 0.0043$
$4-10$	5.30	$-0.020 \pm 0.014 \pm 0.002$

Table 6.7: Final J/ψ longitudinal double spin asymmetry results.

Chapter 7

Conclusions and Future Work

A measurement of the helicity dependence of the production of the charmonium ground state, the J/ψ, has been presented in this document in the form of the double longitudinal spin asymmetry. This result is a novel addition to the ever increasing wealth of experimental data collected to constrain the decomposition of the nucleon spin in terms of the polarization of its constituents within the theoretical framework of quantum chromodynamics. Many recent advances in the determination of the polarized parton distribution functions have been pioneered by the experiments at RHIC. The J/ψ spin asymmetry measurement extends the current knowledge of the gluon polarization in the proton into an x range that has never been explored.

The large statistics, high energy polarized pp run in 2013 has enabled a reduction of nearly an order of magnitude in the statistical precision of the studied asymmetry. The asymmetry has been found to be consistent with zero across the studied range of transverse momentum. The measured asymmetry will be included with the existing experimental data in the DSSV++ polarized PDFs to constrain the uncertainty on the gluon polarization at low x. In order to do so, a measurement of the J/ψ cross section at $\sqrt{s} = 510$ GeV is needed, and forthcoming, at RHIC in order to validate

the NNLO pQCD calculations involved in the global fit. The A_{LL} result also serves to validate the existing gluon polarization data at RHIC from π^0 and jet asymmetries by accessing the effects of gg fusion versus gq scattering.

The major FVTX detector upgrade was installed and commissioned during the 2012 RHIC running period in preparation for the 2013 running period and beyond. The detector has been shown to meet or exceed the performance specification set out during its inception. Numerous improvements have been made to the software and firmware that have guaranteed the observed high levels of performance. In addition, the capabilities of the FVTX detector have been expanded beyond those conceived during the planning and construction stages to include capabilities for real time luminosity monitoring. With further study and improvement, the additional information will aid in the effort to reduce the systematic uncertainty in the relative luminosity. This reduction is not necessary for the J/ψ A_{LL} as the result is statistically limited by a large margin, but will become important for future measurements of probes with sufficient statistics to measure asymmetries that are $\mathcal{O}(10^{-4})$. Additionally, novel trigger capabilities have been developed and made available for inclusion in future configurations allowing for refinement of existing muon triggers and efficient studies of high multiplicity phenomena.

Looking to the future, this result alone will not be sufficient to conclusively determine the total contribution of the gluon polarization to the spin polarization of the proton. From the current era of RHIC and PHENIX there remains only a single additional measurement to be made that is capable of further constraining the gluon polarization: the π^0 A_{LL} in the very forward Muon Piston Calorimeter. That measurement will benefit from the large production cross section of the π^0 and have statistical uncertainties on the order of 10^{-4} while accessing a similar x range as the J/ψ A_{LL}. Even this measurement, while being capable of providing a meaningful reduction in the uncertainties in $\Delta g(x)$ at small values of x, will still not likely be

able to provide a truly decisive quantification of the total gluon polarization in the proton.
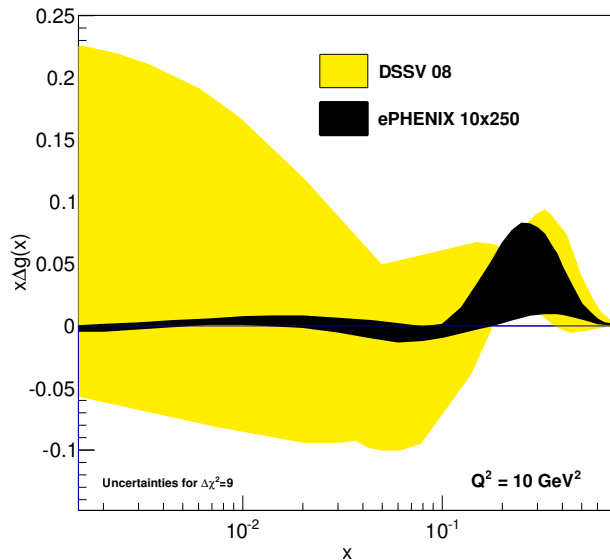
Figure 7.1: Projected uncertainties on the polarized gluon PDF from asymmetry measurements in a proposed polarized electron ion collider (EIC) at RHIC.

To do so will require the construction of a spin polarized electron ion collider (EIC) and a move back to SIDIS measurements versus polarized hadron-hadron collisions. However, the EIC will provide the necessary kinematics and luminosity to once and for all determine the gluon polarization over a wide x range. Currently in early research and development are accompanying detector upgrades at PHENIX in the form of the ePHENIX detector [53]. If funded, the new experimental apparatus will open a new chapter in spin physics, as can be seen in the statistical projections of the impact ePHENIX can have on $\Delta g(x)$ in Figure 7.1.

Appendices

Appendix A

Rate Correction

The rate correction is derived from a statistical argument that reasons that in a coincidence detector, the relationship between the number of events that trigger a single arm of the detector and the number of events that trigger both arms is a function of the true rate that includes multiple collisions per crossing. The argument follows from supposing that the true number of collisions follows a Poisson distribution

$$P_{DS}(i) = \frac{\lambda_i e^{-\lambda}}{i!}, \tag{A.1}$$

where DS signifies that we are considering events that are double-sided in that they trigger can trigger the coincidence detector. Therefore, for the south arm one has that the probability for the detector to be hit k_S times is

$$P_{DS}(k_S) = \sum_{i=k_S}^{\infty} \binom{i}{k_S} \epsilon_S^{k_S} (1 - \epsilon_S)^{i-k_S} P_{DS}(i) \tag{A.2}$$

where ϵ_S is the efficiency, or probability for a hit to be detected, of the south detector.

It can be shown that the probability distribution for k_S is also a Poisson distribution and follows

$$P_{DS}(k_S) = \frac{(\epsilon_s \lambda)_S^k e^{-\epsilon_S \lambda}}{k_S!} \tag{A.3}$$

Appendix A. Rate Correction

. Extending this result to the case of a double sided detector, as is the case of the BBC and ZDC we have that

$$P_{DS}(k_S, k_N) = P_{DS}(k_N|k_S)P_{DS}(k_S) \tag{A.4}$$

$$= \left(\sum_{i=k_N}^{\infty} \binom{i}{k_N} \epsilon_N^{k_N} (1 - \epsilon_N)^{i-k_N} P_{DS}(i|k_S) \right) P_{DS}(k_S)$$

where applying Bayes' theorem

$$P_{DS}(i|k_S) = \frac{P_{DS}(k_S|i)P_{DS}(i)}{P_{DS}(k_S)} \tag{A.5}$$

and taking the special case of $k_S = 0$, $k_N = 0$ the expression reduces to

$$P_{DS}(k_S = 0, k_N = 0) = e^{\epsilon_S \epsilon_N \lambda - \epsilon_S \lambda - \epsilon_N \lambda} = e^{-\epsilon_N(1-\epsilon_S)\lambda} e^{-\epsilon_S \lambda} \tag{A.6}$$

Following the same derivation, but considering events that can only trigger a single side (SS) of the detector with averages of $\lambda_{S(N)}$ that also follow a Poisson distribution we have

$$P(k_S = 0) = P_{DS}(k_S = 0)P_{SS}(k_S = 0) = e^{-\epsilon_S(\lambda + \lambda_S)} \tag{A.7}$$

and

$$P(k_S = 0, k_N = 0) = P_{DS}(k_S = 0, k_N = 0)P_{SS}(k_S = 0)P_{SS}(k_N = 0)$$
$$= e^{\epsilon_S \epsilon_N \lambda - \epsilon_S(\lambda + \lambda_S) - \epsilon_N(\lambda + \lambda_N)} \tag{A.8}$$

Finally, with the derivation complete we can use Equation A.6, Equation A.7, and Equation A.8 to calculate the following

$$\ln(P(k_S = 0, k_N = 0)) - \ln(P(k_S = 0)) - ln(P(k_N = 0)) = \epsilon_N \epsilon_S \lambda \tag{A.9}$$

or, given that $P(k_S = 0) = 1 - P_S$, $P(k_N = 0) = 1 - P_N$, and $P(k_S = 0, k_N = 0) = 1 - P_{OR}$ where P_S, P_N, and P_{OR} are the probabilities of firing the south, north, and logical OR of the south and north triggers. Therefore, we can arrive at the true rate, inclusive of multiple collisions if we can measure the rate at which the above triggers fire.

Appendix B

GPR Background Fits
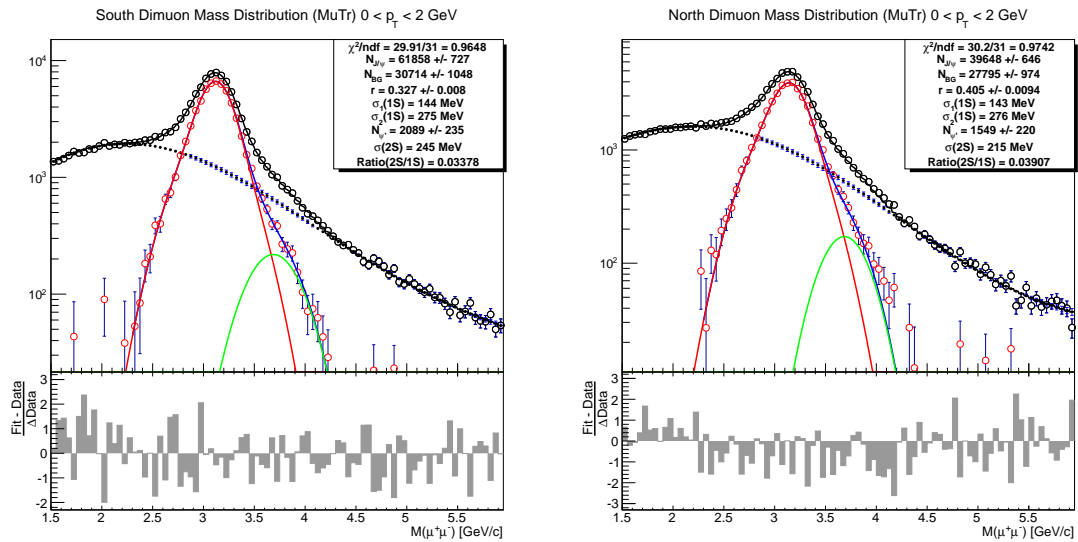
Figure B.1: MuTr mass spectrum fits with GPR background estimation for the 0-2 GeV bin for the north and south arms and the 3σ mass window.
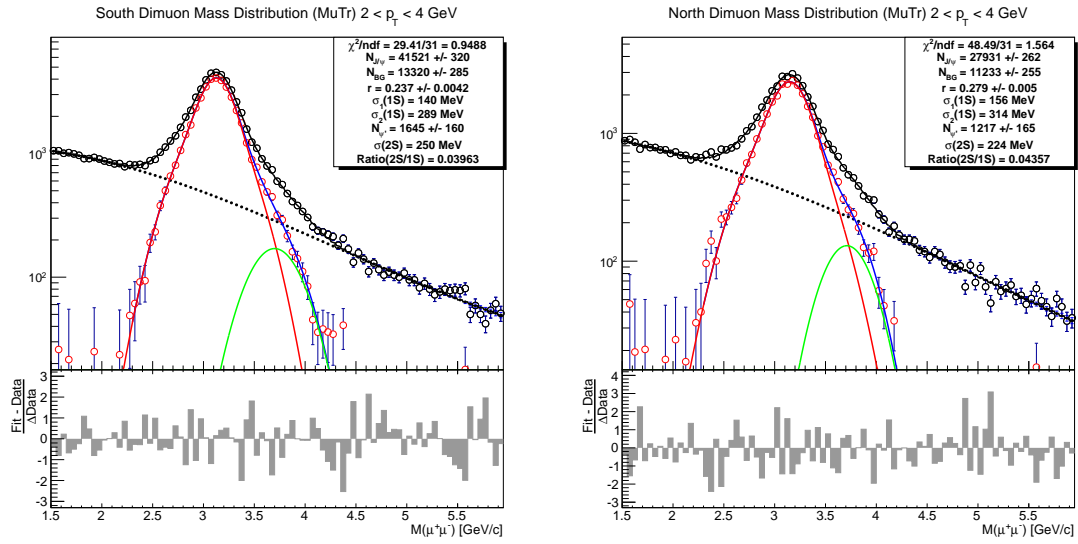
Figure B.2: MuTr mass spectrum fits with GPR background estimation for the 2-4 GeV bin for the north and south arms and the 3σ mass window.
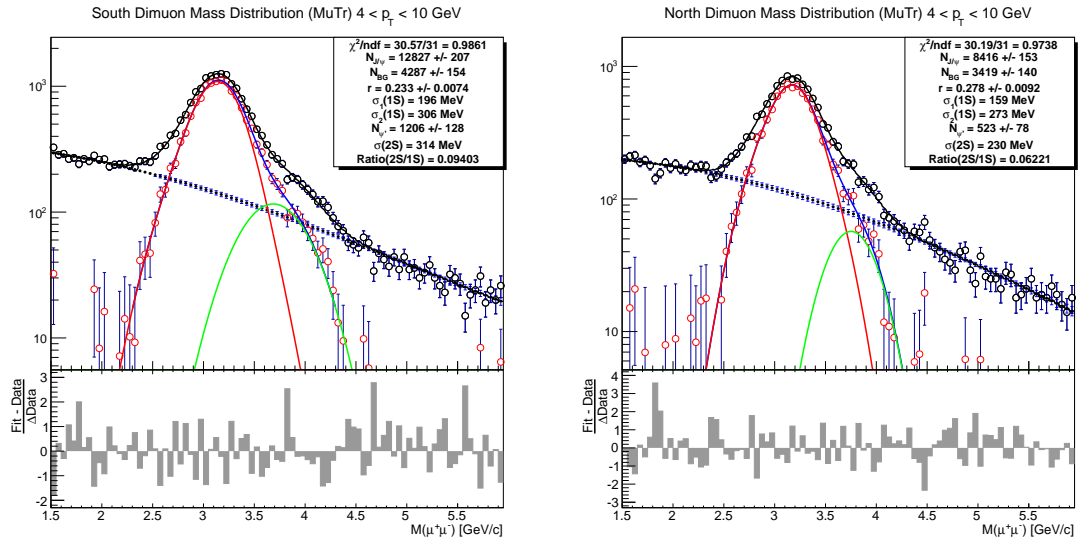
Figure B.3: MuTr mass spectrum fits with GPR background estimation for the 4-10 GeV bin for the north and south arms and the 3σ mass window.

Figure B.4: MuTr+FVTX mass spectrum fits with GPR background estimation for the 0-2 GeV bin for the north and south arms and the 3σ mass window.
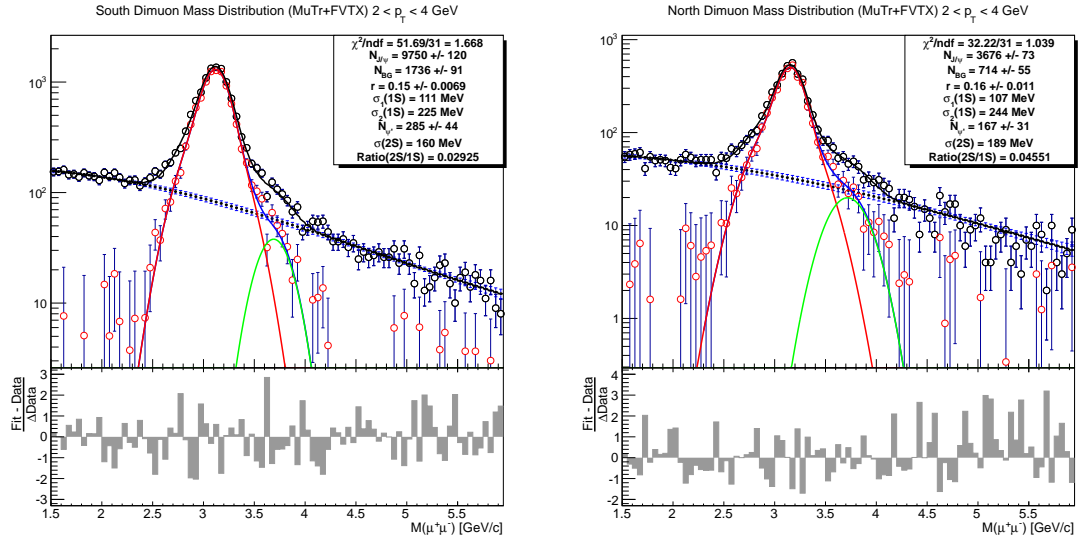
Figure B.5: MuTr+FVTX mass spectrum fits with GPR background estimation for the 2-4 GeV bin for the north and south arms and the 3σ mass window.

Figure B.6: MuTr+FVTX mass spectrum fits with GPR background estimation for the 4-10 GeV bin for the north and south arms and the 3σ mass window.

Appendix C

Simulated Background Fits
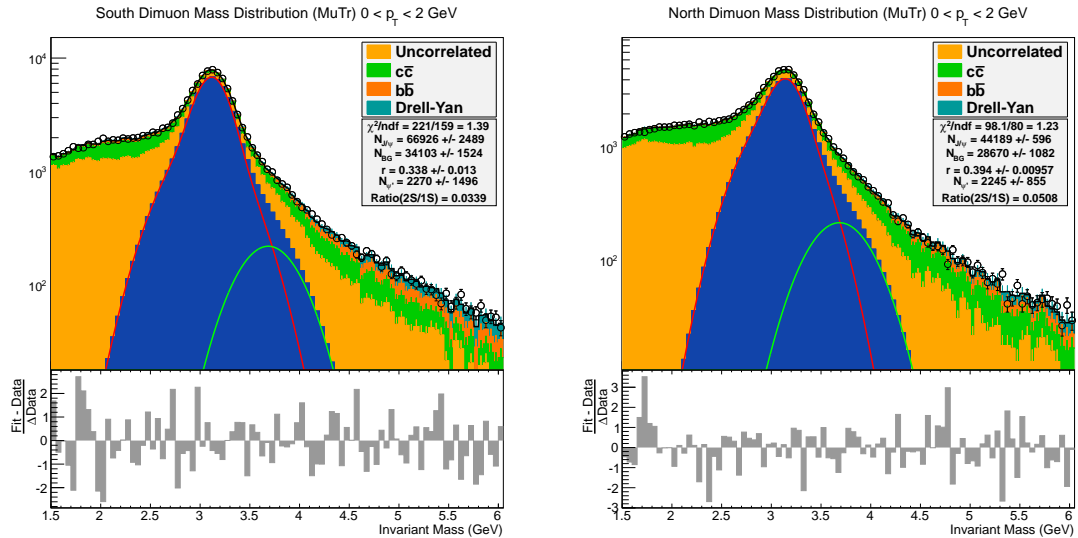
Figure C.1: MuTr mass spectrum fits with simulated background estimation for the 0-2 GeV bin for the north and south arms and the 3σ mass window.
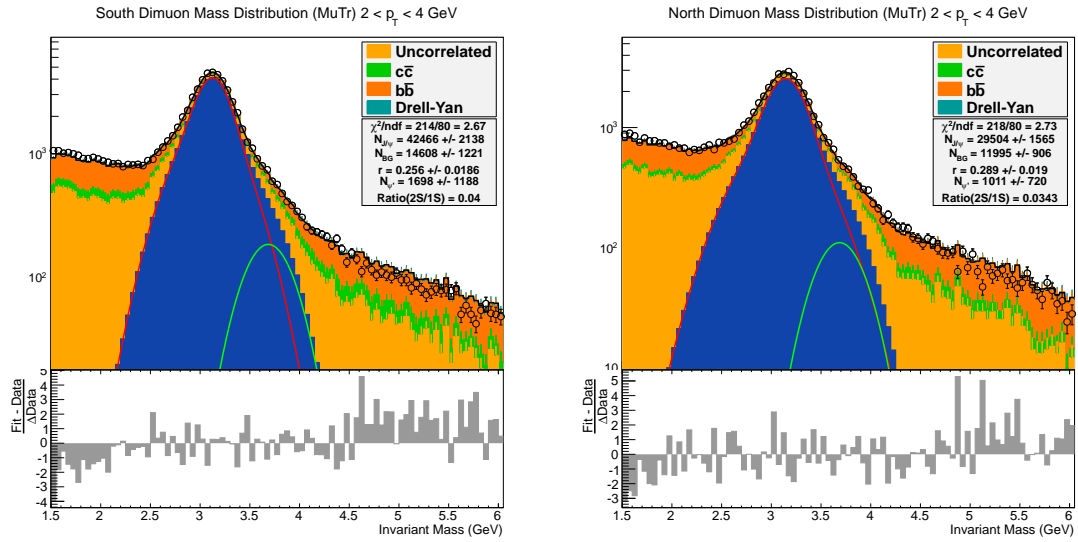
Figure C.2: MuTr mass spectrum fits with simulated background estimation for the 2-4 GeV bin for the north and south arms and the 3σ mass window.
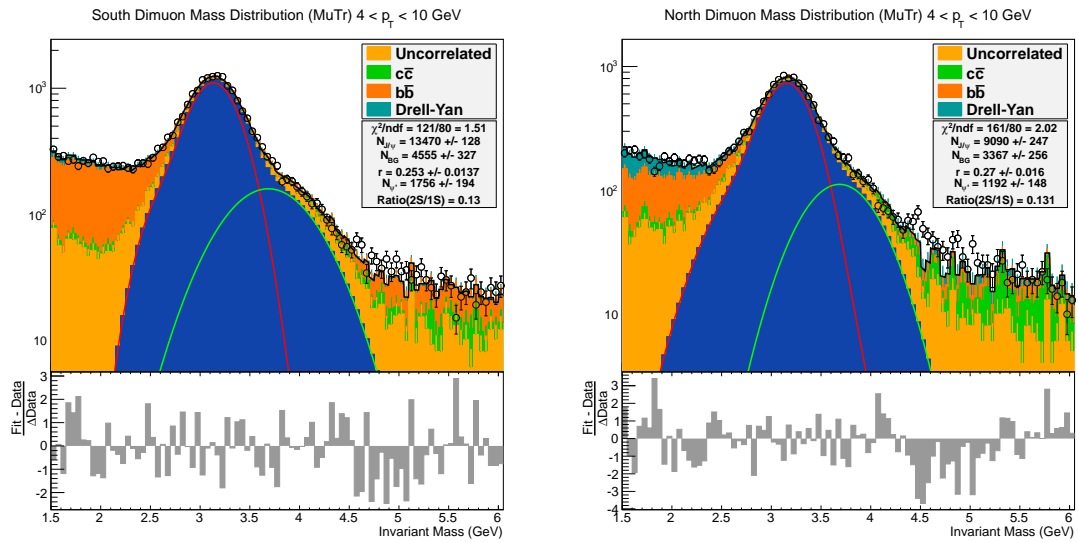
Figure C.3: MuTr mass spectrum fits with simulated background estimation for the 4-10 GeV bin for the north and south arms and the 3σ mass window.

Figure C.4: MuTr+FVTX mass spectrum fits with simulated background estimation for the 0-2 GeV bin for the north and south arms and the 3σ mass window.
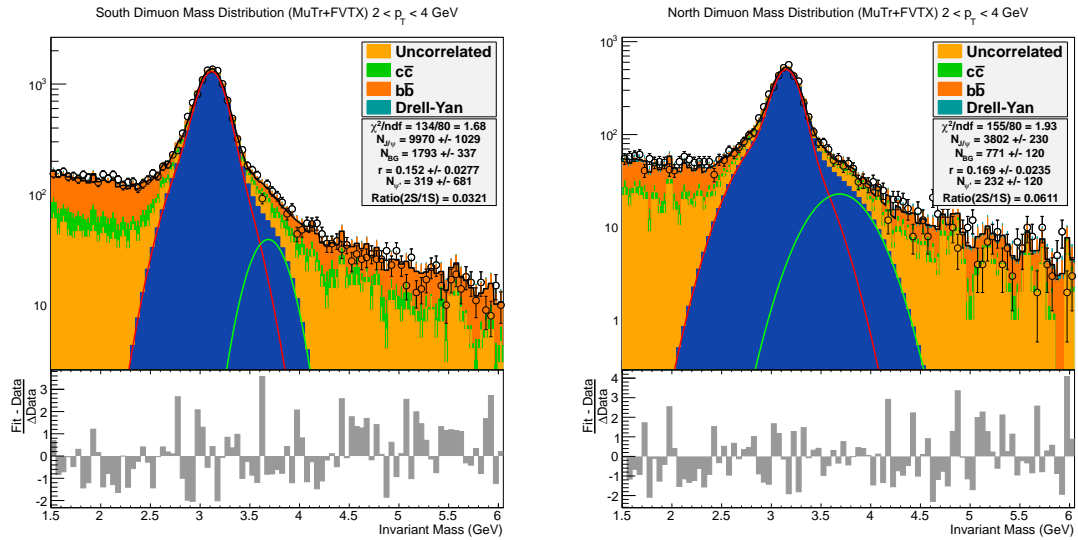
Figure C.5: MuTr+FVTX mass spectrum fits with simulated background estimation for the 2-4 GeV bin for the north and south arms and the 3σ mass window.

Figure C.6: MuTr+FVTX mass spectrum fits with simulated background estimation for the 4-10 GeV bin for the north and south arms and the 3σ mass window.

Appendix D

Background Fractions

Appendix D. Background Fractions

Detector	$p_T \in [0,2]$ GeV	$p_T \in \,]2,4]$ GeV	$p_T \in \,]4,10]$ GeV
MuTr N	$0.337 \pm 0.009 \pm 0.023$	$0.218 \pm 0.004 \pm 0.009$	$0.220 \pm 0.008 \pm 0.023$
MuTr S	$0.261 \pm 0.008 \pm 0.021$	$0.178 \pm 0.004 \pm 0.009$	$0.180 \pm 0.006 \pm 0.017$
FVTX N	$0.18 \pm 0.01 \pm 0.03$	$0.124 \pm 0.008 \pm 0.017$	$0.14 \pm 0.01 \pm 0.03$
FVTX S	$0.13 \pm 0.01 \pm 0.03$	$0.118 \pm 0.006 \pm 0.017$	$0.13 \pm 0.01 \pm 0.03$

Table D.1: GPR background fractions for the 2σ window. Statistical errors and correlated errors from GPR method with systematic added are shown

Detector	$p_T \in [0,2]$ GeV	$p_T \in \,]2,4]$ GeV	$p_T \in \,]4,10]$ GeV
MuTr N	$0.405 \pm 0.009 \pm 0.023$	$0.279 \pm 0.005 \pm 0.009$	$0.278 \pm 0.008 \pm 0.023$
MuTr S	$0.327 \pm 0.008 \pm 0.021$	$0.237 \pm 0.004 \pm 0.009$	$0.233 \pm 0.006 \pm 0.017$
FVTX N	$0.23 \pm 0.02 \pm 0.03$	$0.16 \pm 0.01 \pm 0.017$	$0.19 \pm 0.02 \pm 0.03$
FVTX S	$0.18 \pm 0.01 \pm 0.03$	$0.150 \pm 0.006 \pm 0.017$	$0.17 \pm 0.01 \pm 0.03$

Table D.2: GPR background fractions for the 3σ window. Statistical errors and correlated errors from GPR method with systematic added are shown

Detector	$p_T \in [0,2]$ GeV	$p_T \in \,]2,4]$ GeV	$p_T \in \,]4,10]$ GeV
MuTr N	0.308 ± 0.008	0.223 ± 0.014	0.20 ± 0.02
MuTr S	0.257 ± 0.007	0.188 ± 0.012	0.19 ± 0.02
FVTX N	0.14 ± 0.01	0.12 ± 0.02	0.11 ± 0.02
FVTX S	0.131 ± 0.008	0.108 ± 0.014	0.10 ± 0.02

Table D.3: Simulated background fractions and statistical errors for the 2σ window.

Detector	$p_T \in [0,2]$ GeV	$p_T \in \,]2,4]$ GeV	$p_T \in \,]4,10]$ GeV
MuTr N	0.40 ± 0.01	0.29 ± 0.02	0.27 ± 0.02
MuTr S	0.34 ± 0.01	0.26 ± 0.02	0.25 ± 0.01
FVTX N	0.19 ± 0.02	0.17 ± 0.02	0.18 ± 0.02
FVTX S	0.178 ± 0.014	0.15 ± 0.03	0.15 ± 0.02

Table D.4: Simulated background fractions and statistical errors for the 3σ window.

Appendix E

Component Asymmetries
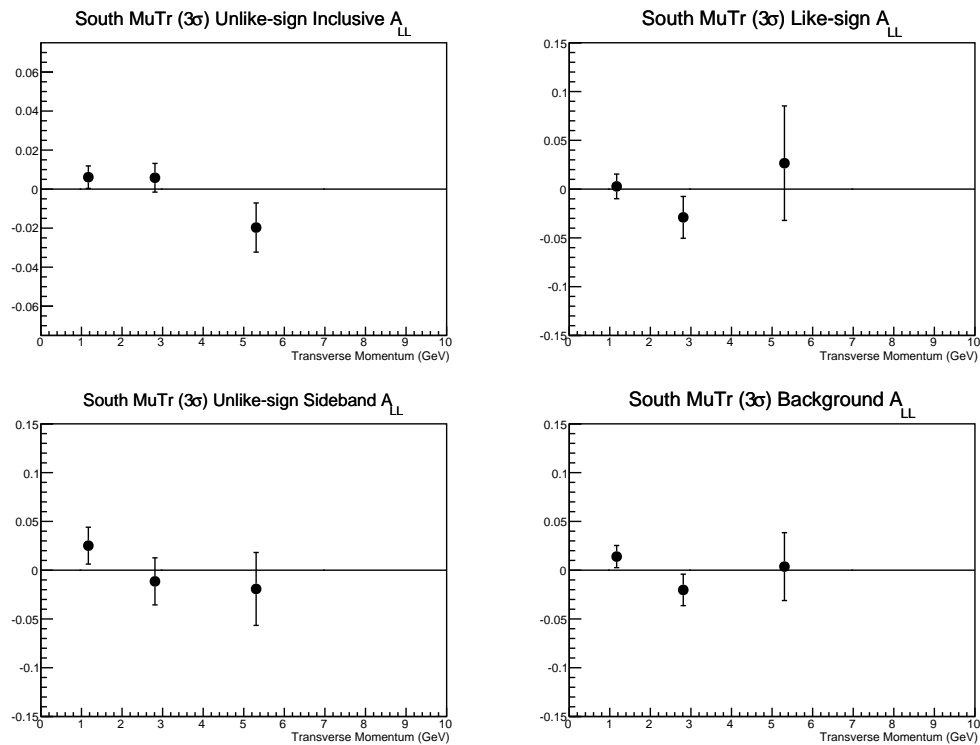
Figure E.1: Inclusive and background asymmetries for the south MuTr 3σ dataset
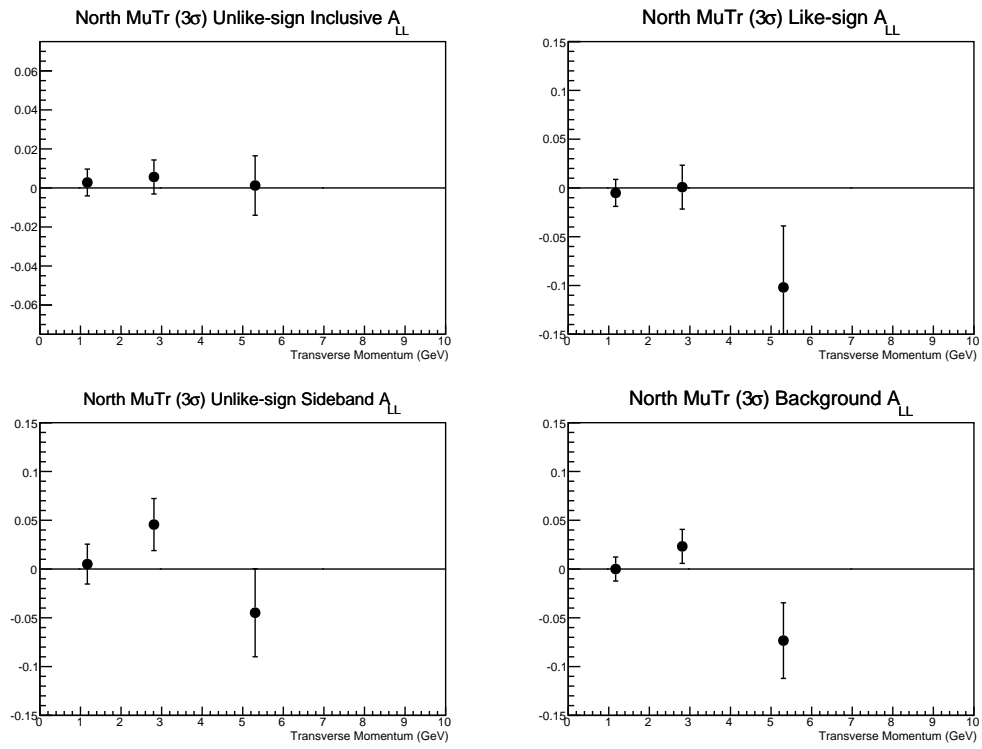
Figure E.2: Inclusive and background asymmetries for the north MuTr 3σ dataset
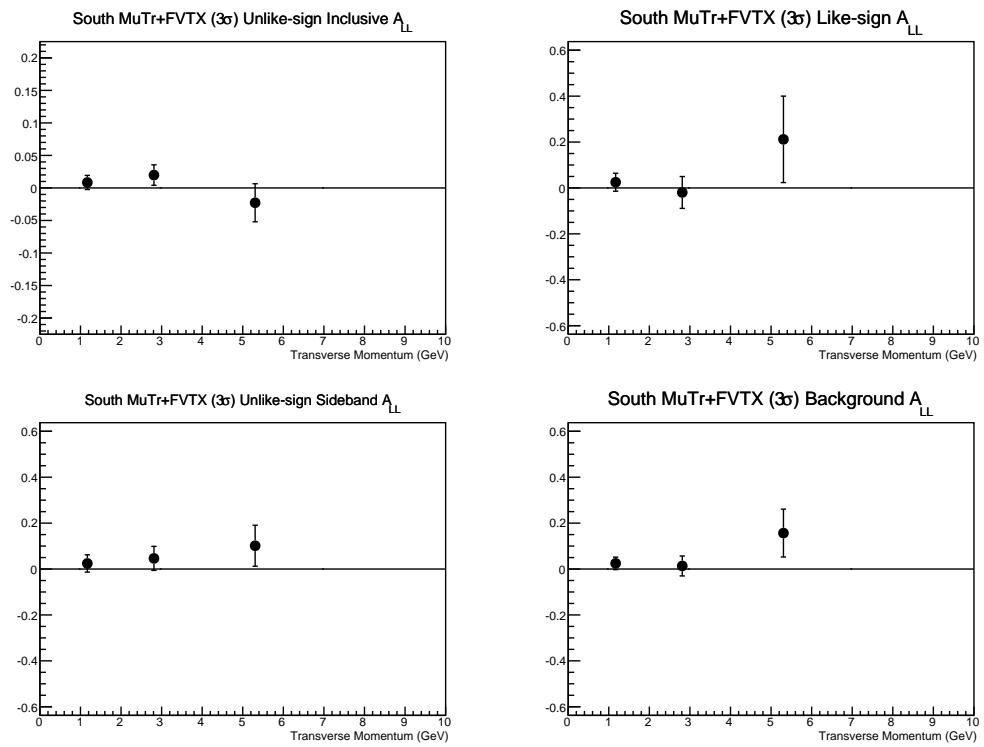
Figure E.3: Inclusive and background asymmetries for the south MuTr+FVTX 3σ dataset
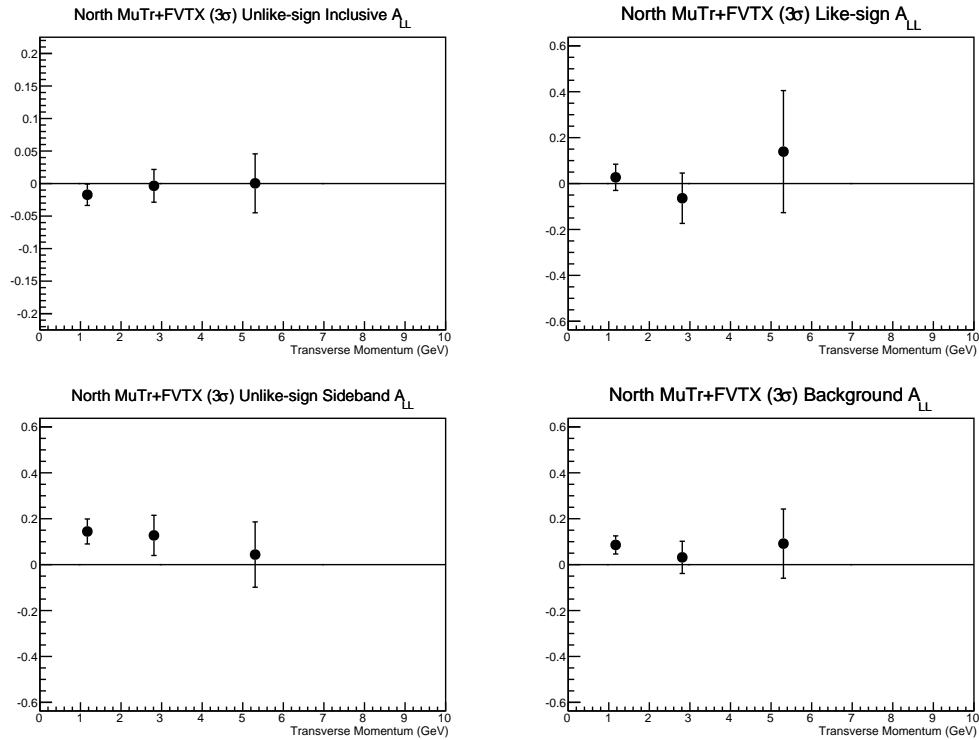
Figure E.4: Inclusive and background asymmetries for the north MuTr+FVTX 3σ dataset

Figure E.5: 3σ signal asymmetries for the south (left) and north (right) MuTr.
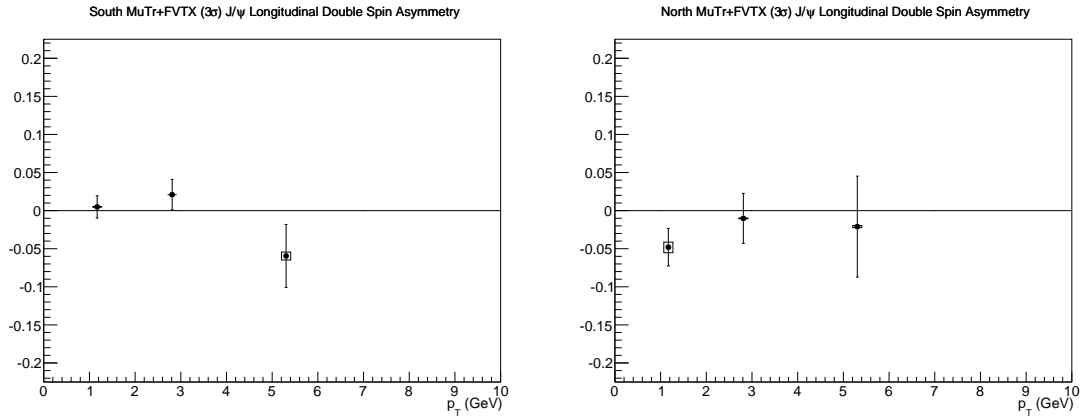
Figure E.6: 3σ signal asymmetries for the south (left) and north (right) MuTr+FVTX.

Figure E.7: 3σ signal asymmetries for the MuTr (left) and MuTr+FVTX (right) subsets after combining the asymmetries for the north and south arms.

Bibliography

1. S. L. Glashow, *Nuclear Physics* **22**, 579–588 (Feb. 1961).

2. M. E. Peskin, D. V. Schroeder, *An introduction to quantum field theory* (Westview, 1995).

3. V. S. Varadarajan, *Lie groups, Lie algebras, and their representations* (Prentice-Hall Englewood Cliffs, NJ, 1974), vol. 102.

4. M Gell-Mann, Y Neeman, *The eightfold way: a review, with a collection of reprints* (W.A. Benjamin, 1964).

5. R. Feynman, *Physical Review Letters* **23**, 1415–1417 (Dec. 1969).

6. W. Greiner, D. A. Bromley, S. Schramm, E. Stein, *Quantum chromodynamics* (Springer, 2007).

7. H. Fritzsch, M. Gell-Mann, H. Leutwyler, *Physics Letters B* **47**, 365–368 (Nov. 1973).

8. K. Wilson, *Physical Review D* **10**, 2445–2459 (Oct. 1974).

9. G. Altarelli, G. Parisi, *Nuclear Physics B* **126**, 298–318 (Aug. 1977).

10. H David Politzer, *Physics Reports* **14**, 129–180 (Nov. 1974).

11. M. Gell-Mann, *Physics Letters* **8**, 214–215 (Feb. 1964).

12. H. Politzer, *Physical Review Letters* **30**, 1346–1349 (June 1973).

13. S. Bethke, *Progress in Particle and Nuclear Physics* **58**, 351–386 (Apr. 2007).

14. V. Balagura, *Nuclear Instruments and Methods in Physics Research Section A: Accelerators, Spectrometers, Detectors and Associated Equipment* **654**, 634–638 (Oct. 2011).

15. R. Hofstadter, R. McAllister, *Physical Review* **98**, 217–218 (Apr. 1955).

16. Y. Dokshitzer, *Zh. Eksp. Teor. Fiz* **46** (1977).

17. J. Bjorken, *Physical Review* **179**, 1547–1553 (Mar. 1969).

18. J. Gao *et al.*, *Physical Review D* **89**, 033009 (Feb. 2014).

19. a.V. Belitsky, a.V. Radyushkin, *Physics Reports* **418**, 1–387 (Oct. 2005).

20. M. Diehl, *Physics Reports* **388**, 41–277 (Dec. 2003).

21. X. Ji, *Annual Review of Nuclear and Particle Science* **54**, 413–450 (Dec. 2004).

22. J Ashman *et al.*, *Physics Letters B* **206**, 364–370 (May 1988).

23. J. Aubert *et al.*, *Physical Review Letters* **33**, 1404–1406 (Dec. 1974).

24. M Anerella *et al.*, *Nuclear Instruments and Methods in Physics Research Section A: Accelerators, Spectrometers, Detectors and Associated Equipment* **499**, 280–315 (Mar. 2003).

25. V. Bargmann, V. L. Telegdi, *Physical Review Letters* **2**, 435–436 (May 1959).

26. I Alekseev *et al.*, *Nuclear Instruments and Methods in Physics Research Section A: Accelerators, Spectrometers, Detectors and Associated Equipment* **499**, 392–414 (Mar. 2003).

27. A. Krisch *et al.*, *Physical Review Letters* **63**, 1137–1140 (Sept. 1989).

28. M. Okamura *et al.*, *Nuclear Instruments and Methods in Physics Research Section A: Accelerators, Spectrometers, Detectors and Associated Equipment* **452**, 53–60 (Sept. 2000).

29. K. O. Eyser *et al.*, presented at the AIP Conference Proceedings, vol. 915, pp. 916–919, arXiv:`0612020v1` [`arXiv:nucl-ex`].

30. K. Adcox *et al.*, *Nuclear Instruments and Methods in Physics Research Section A: Accelerators, Spectrometers, Detectors and Associated Equipment* **499**, 469–479 (Mar. 2003).

31. K. Adcox *et al.*, *Nuclear Instruments and Methods in Physics Research Section A: Accelerators, Spectrometers, Detectors and Associated Equipment* **499**, 489–507 (Mar. 2003).

32. H. Ohnishi, *Nuclear Instruments and Methods in Physics Research Section A: Accelerators, Spectrometers, Detectors and Associated Equipment* **569**, 33–36 (Dec. 2006).

33. T. Ypsilantis, J Seguinot, *Nuclear Instruments and Methods in Physics Research Section A: Accelerators, Spectrometers, Detectors and Associated Equipment* **343**, 30–51 (Apr. 1994).

34. M. Aizawa *et al.*, *Nuclear Instruments and Methods in Physics Research Section A: Accelerators, Spectrometers, Detectors and Associated Equipment* **499**, 508–520 (Mar. 2003).

35. H. Akikawa *et al.*, *Nuclear Instruments and Methods in Physics Research Section A: Accelerators, Spectrometers, Detectors and Associated Equipment* **499**, 537–548 (Mar. 2003).

36. M. Allen *et al.*, *Nuclear Instruments and Methods in Physics Research Section A: Accelerators, Spectrometers, Detectors and Associated Equipment* **499**, 549–559 (Mar. 2003).

37. C Adler *et al.*, *Nuclear Instruments and Methods in Physics Research Section A: Accelerators, Spectrometers, Detectors and Associated Equipment* **470**, 488–499 (Sept. 2001).

38. B. Meredith, *Nuclear Instruments and Methods in Physics Research Section A: Accelerators, Spectrometers, Detectors and Associated Equipment* **602**, 766–770 (May 2009).

39. R. Towell, *Nuclear Instruments and Methods in Physics Research Section A: Accelerators, Spectrometers, Detectors and Associated Equipment* **602**, 705–708 (May 2009).

40. A. Taketani *et al.*, *Nucl. Instrum. Meth. A* **623**, 374–376 (2010).

41. J. Hoff, T. Zimmerman, R. Yarema, J. Kapustinsky, M. Brooks, *2009 IEEE Nuclear Science Symposium Conference Record (NSS/MIC)*, 75–79.

42. J. S. Kapustinsky, *Nucl. Instrum. Meth. A* **617**, 546 –548 (2010).

43. V. Blobel, *Nucl. Instrum. Meth. A* **566**, 5 –13 (2006).

44. R. O. Duda, P. E. Hart, *Communications of the ACM* **15**, 11–15 (Jan. 1972).

45. D. Ben-Tzvi, M. Sandler, *Pattern Recognition Letters* **11**, 167–174 (Mar. 1990).

46. S. Gupta, P. Mathews, *Physical Review D* **55**, 7144–7151 (June 1997).

47. a Adare *et al.*, *Physical Review Letters* **103**, 012003 (July 2009).

48. L Adamczyk *et al.*, *Physical Review D* **86**, 032006 (Aug. 2012).

49. D. de Florian, R. Sassot, M. Stratmann, W. Vogelsang, *Physical Review D* **80**, 034030 (Aug. 2009).

50. P Cho, A. Leibovich, *Physical review D: Particles and fields* **53**, 6203–6217 (June 1996).

51. C. E. Rasmussen, C. K. I. Williams, *Gaussian Processes for Machine Learning (Adaptive Computation and Machine Learning)* (The MIT Press, 2005).

52. D. Comaniciu, P. Meer, S. Member, *IEEE Transactions on Pattern Analysis and Machine Intelligence* **24**, 603–619 (May 2002).

53. A Adare, Others, arXiv:1402.1209 `[nucl-ex]` (2014).